TECHNISCHE UNIVERSITÄT MÜNCHEN

WALTHER-MEISSNER-INSTITUT FÜR TIEF-TEMPERATURFORSCHUNG

BAYERISCHE AKADEMIE DER WISSENSCHAFTEN

Experimental Study of Spin Currents in Compensated Rare Earth Garnets

Master's Thesis

Kathrin Ganzhorn

Supervisor: PD Dr. Sebastian T. B. Gönnenwein

Munich, 21 October 2014

To my grandfather

Contents

List of Figures

List of Tables

Introduction

In times, in which our everyday life seems impossible without internet, computers, smart phones etc., large amounts of money are put into the development and improvement of such technologies. In the last decades, the need for more efficient computing devices, i.e. faster data processing and transfer, smaller devices with more storage and low thermal design power, increased drastically. There are however lower boundaries to the size of devices based on electron charge transfer, due to the Joule heating of charge currents. Since the electron does not only transport charge, but also a spin, the idea of transporting information via the spin degree of freedom, instead of using the electron charge, gave rise to a new research field called spintronics, in analogy to the conventional electronics. Pure spin currents, i.e. currents of angular momentum, which do not transport any charge, can flow in electric insulators and could therefore help to overcome the limits of conventional electronic devices. Therefore, one goal in the field of spintronics is the developement of circuitry based on spin currents. To this end, first the generation and detection of spin currents needs to be investigated. A promising candidate for the electrical detection of spin currents is the Inverse Spin Hall Effect (ISHE) in normal metals, which is now well established for nearly a decade [1]. The investigation of spin current sources is still one of the hot topics in the field of spintronics. One concept for the generation of spin currents is to induce magnetization dynamics in a ferromagnetic insulator, giving rise to a spin current which can flow into an adjacent normal metal, so that it can be electrically detected via the ISHE. The spin Seebeck effect, observed for the first time in 2008 in ferromagnetic metals [2] and 2 years later also in ferromagnetic insulators [3], generates a spin current through thermal excitation, i.e. when a temperature gradient is applied across the bilayer interface. For the spin pumping effect, reported in 2002 [4, 5], the magnetization of the ferromagnetic material is resonantly excited by a microwave magnetic field (ferromagnetic resonance) and relaxes by pumping a spin current across the interface, into the normal metal layer.

In addition to the spin current generation and detection, it was recently discovered that ferromagnetic insulator/normal metal bilayers also exhibit a magnetoresistive effect, i.e. the spin Hall magnetoresistance (SMR) effect [6–8]. The SMR is based on the fact, that the magnetization orientation in the insulating ferromagnet changes the resistance of the non magnetic metal through the absorption of spin currents. This effect might be a candidate for a new kind of magnetic field sensor.

While the SSE [2, 3, 9–13], spin pumping [14–17] and SMR [6–8] effects have been thoroughly investigated in ferrimagnetic insulator/normal metal heterostructures, and microscopic models of the processes involved in the generation of spin currents have been proposed [4, 18–20], there are still open questions. Although a spin current is defined as a flow of angular momentum, spin pumping, spin Seebeck effect and SMR are today described in terms of magnetization dynamics via the Landau-Lifschitz-Gilbert equation [21, 22]. Therefore, the question arises whether the spin current originates in the dynamics of the angular momentum $\mathbf{L}$ or the magnetization $\mathbf{M}$ in the ferromagnet. In most materials, this distinction is not necessary since $\mathbf{M}$ and $\mathbf{L}$ are simply related by a proportionality factor γ, the gyromagnetic ratio. However, in compensated ferrimagnets multiple sublattices contribute to the total magnetization and total angular momentum of the spin system [23, 24]. Since the gyromagnetic ratios of the sublattices are not equal in general [25], the proportionality factor γ_{eff} between the total angular momentum and total magnetization is not a constant in these materials [24, 26]. In particular, around a temperature called the magnetization compensation temperature $T_{\text{comp, M}}$, where all sublattice magnetizations cancel each other out, γ_{eff} goes to zero, and diverges at the angular momentum compensation temperature $T_{\text{comp, L}}$. These magnetically compensated materials should therefore allow for the experimental distinction of angular momentum and magnetic moment, since they both have different temperature dependencies. In this thesis, we thus conduct spin current experiments as a function of temperature, in order to determine whether a spin current is indeed related to magnetization dynamics, as the theoretical description suggests, or rather originates in the angular momentum dynamics. Such a method for the distinction between angular momentum and magnetization dynamics using spin current experiments has not been put forward to date, and would enhance our understanding of the microscopic effects related to spin currents.

This thesis is structured as follows: Chapter 1 gives an overview of the theoretical concepts behind ferromagnetic resonance, spin current detection via the ISHE, spin current generation via the SSE and spin pumping, as well as the SMR effect. We will also discuss the main properties of magnetically compensated materials.

In Chapter 2, we describe the process of fabrication and optimization for the samples used in this thesis, i.e. Yttrium Iron Garnet/Pt (YIG/Pt), which does not exhibit compensation, and two magnetically compensated materials: Gadolinium Iron Garnet/Pt (GdIG/Pt) and In, Y doped Gadolinium Iron Garnet (InYGdIG/Pt).

A model, which allows for the calculation of the sublattice magnetizations in our samples as a function of temperature, is presented in Chapter 3. Using this model, we can simulate the effective gyromagnetic ratio and ferromagnetic resonance field in all three samples, which we then compare to the experimental data.

In Chapter 4, we start with a description of the experimental setup used for ferromagnetic resonance, spin pumping and microwave heating induced spin Seebeck effect. We then

proceed to the discussion of these measurements in YIG/Pt. These reference measurements will enable us to distinguish effects and temperature dependencies inherent only to magnetically compensated materials from those which can also be observed in ordinary ferrimagnetic materials. We then turn to the analysis of the temperature dependent spin current generation experiments in the compensated materials InYGdIG/Pt and GdIG/Pt and propose a phenomenological model based on the simulation in Chapter 3, which qualitatively reproduces the experimental results.

The results of magneto-transport measurements in InYGdIG/Pt are presented in Chapter 5. First, the experimental setup is described, followed by the analysis of current heating induced SSE measurements as a function of temperature. These results are compared to the microwave heating induced SSE measurements presented in Chap. 4. Finally, we discuss spin Hall magnetoresistance measurements as a function of temperature and propose a model which explains the behaviour of the sample resistance near the compensation temperature.

The thesis concludes with a summary of the results in Chapter 6, as well as an outlook on future experiments for further investigations in magnetically compensated materials.

Chapter 1

Theory

In this Chapter we give a compact overview of the theoretical principles relevant in this thesis. First an introduction to ferromagnetic resonance and magnetic anisotropies is given. We then proceed to the detection and generation of spin currents in a ferromagnet/normal metal bilayer and discuss microwave rectification due to magnetoresistive effects. Finally, temperature and magnetic field dependent properties of the magnetically compensated material Gadolinium Iron Garnet are discussed.

1.1 Ferromagnetic Resonance

1.1.1 Ferromagnetic resonance condition

In a ferromagnet, the magnetic moments are coupled by an exchange interaction, so that the whole spin system with magnetization $\mathbf{M}$ can be described by a macrospin. This macrospin precesses around an effective magnetic field $\mu_0\mathbf{H}_{\text{eff}}$ with the Larmor frequency

$$\omega_0 = \gamma\mu_0 H_{\text{eff}} \tag{1.1}$$

where $\gamma = eg/2m < 0$ is the gyromagnetic ratio with e and m the electron charge and mass [27]. A microwave magnetic field with the same frequency is resonantly absorbed and leads to a deflection of the macrospin, this is called ferromagnetic resonance (FMR). The time dependent evolution of the magnetization is described by the Landau-Lifschitz-Gilbert equation (LLG) [21, 22, 27]

$$\frac{\partial\mathbf{M}}{\partial t} = \gamma\left[\mathbf{M}\times(\mu_0\mathbf{H}_{\text{eff}})\right] + \frac{\alpha_0\gamma}{M_s}\left[\mathbf{M}\times(\mathbf{M}\times\mu_0\mathbf{H}_{\text{eff}})\right] \tag{1.2}$$

with the saturation magnetization M_s and the dimensionless damping parameter α_0. The first term on the right hand side in Eq. (1.2) describes the torque acting on $\mathbf{M}$ due to $\mathbf{H}_{\text{eff}}$. The second term is the damping term: relaxation processes cause the magnetization to spiral back to a position aligned with $\mathbf{H}_{\text{eff}}$.

The effective field $\mu_0\mathbf{H}_{\text{eff}}$ consists of the static external magnetic field $\mu_0\mathbf{H}_0$ and an internal magnetic field $\mu_0\mathbf{H}_{\text{int}}$ due to exchange interaction with other magnetic moments,

crystalline anisotropy, shape anisotropy etc., which will be discussed in more detail in Sect. 1.1.2:

$$\mathbf{H}_{\text{eff}} = \mathbf{H}_0 + \mathbf{H}_{\text{int}} \tag{1.3}$$

The damped precession of the magnetization in FMR is similar to a damped harmonic oscillator of the form $e^{-\Delta\omega t}\cos(\omega_0 t)$ [27], which in the frequency domain corresponds to a Lorentzian absorption line at the resonance frequency ω_0 with a half width at half maximum $\Delta\omega$. For the FMR experiments conducted in this thesis, the microwave frequency is kept constant, while the magnetic field is swept. Since ω is essentially proportional to the magnetic field (see Eq. (1.1)) [27], we also expect a Lorentzian lineshape as a function of the external magnetic field $\mu_0 H_0$

$$S \cdot \frac{\Delta H^2}{(H_0 - H_{\text{res}})^2 + \Delta H^2} \tag{1.4}$$

where H_{res} is the center of the peak, i.e. the magnetic field resonance position, ΔH is the half width at half maximum and S the peak amplitude, so that $S \cdot \Delta H \cdot \pi$ is the peak area.

1.1.2 Influence of anisotropy on the resonance condition

We have seen in Sect. 1.1 that the magnetization dynamics in a ferromagnet depend on an effective magnetic field $\mu_0\mathbf{H}_{\text{eff}}$. A free energy ansatz allows us to take into account the internal fields in the sample and determine the resonance condition. The total free energy of the sample can be decomposed into [27, 28]:

$$F_{\text{tot}} = F_{\text{stat}} + F_{\text{demag}} + F_{\text{c}} + F_{\text{u,oop}} \tag{1.5}$$

The Zeeman energy F_{stat} is the magnetostatic energy of a sample with magnetization $\mathbf{M}$ in an external magnetic field $\mu_0\mathbf{H}_0$:

$$F_{\text{stat}} = -\mu_0\, \mathbf{M} \cdot \mathbf{H}_0 \tag{1.6}$$

The demagnetization term, also called shape anisotropy, depends on the demagnetization tensor $\mathbf{N}$, which is determined by the sample shape, and the sample magnetization $\mathbf{M}$:

$$F_{\text{demag}} = \frac{\mu_0}{2}\mathbf{M} \cdot \mathbf{N} \cdot \mathbf{M} \tag{1.7}$$

In addition to the shape anisotropy there are also contributions from crystalline anisotropies: $F_{\text{u,oop}}$, the free energy of the crystalline uniaxial anisotropy, which can be due to strain in the material (e.g. lattice mismatch with the substrate), giving rise to easy and hard magnetic axes. $F_{\text{u,oop}}$ is proportional to the uniaxial crystalline anisotropy constant $K_{\text{u,oop}}$ [28]. We will also consider a crystalline anisotropy reflecting the symmetry

of the local environment of the magnetic moments in the thin film: in all our samples we will assume an additional cubic anisotropy contribution F_c to the free energy, proportional to the cubic crystalline anisotropy constant K_c [28].

The derivation of the resonance condition from the total free energy is described in detail in Sect. 3.3.

1.2 Spin current generation

In this Section we will describe different effects related to the topic of spinelectronics in ferromagnetic insulator/normal metal bilayers. Starting with spin currents and their detection, we will discuss different ways of generating a spin current, i.e. the spin Seebeck effect (SSE) and spin pumping. We will also present the recently discovered spin Hall magnetoresistance (SMR).

1.2.1 Spin currents and their detection

In addition to their charge, electrons also carry spin angular momentum, i.e. an up or down spin. The total charge current can be written as

$$\mathbf{I}_q = \mathbf{I}_\uparrow + \mathbf{I}_\downarrow \tag{1.8}$$

with $\mathbf{I}_\uparrow$ the current of spin up electrons and $\mathbf{I}_\downarrow$ the current of spin down electrons. We can in a similar way define the spin current in units of angular momentum

$$\mathbf{I}_s = -\frac{\hbar}{2e}(\mathbf{I}_\uparrow - \mathbf{I}_\downarrow) \tag{1.9}$$

A simple way to generate such a spin current is via the spin Hall effect (SHE) [29–31], which transforms a charge current into a transverse spin current. For this effect, a paramagnetic material with a strong spin-orbit coupling, e.g. Pt, is necessary: different microscopic mechanisms, viz. skew scattering [32], side-jump scattering [33] and intrinsic effects [34] cause spin up and down electrons to flow into opposite directions perpendicular to $\mathbf{I}_c$ leading to a pure spin current given by [35]

$$\mathbf{I}_s^{\mathrm{SH}} = \alpha_{\mathrm{SH}} \left(-\frac{\hbar}{2e}\right) [\mathbf{I}_q \times \boldsymbol{\sigma}] \tag{1.10}$$

with α_{SH} the spin Hall angle and $\boldsymbol{\sigma}$ the spin polarization.

The inverse spin Hall (ISHE) effect in a paramagnet transforms a pure spin current into a transverse pure charge current allowing for an electrical detection of spin currents [1, 35]

$$\mathbf{I}_q^{\mathrm{ISH}} = \alpha_{\mathrm{SH}} \left(-\frac{2e}{\hbar}\right) [\mathbf{I}_s \times \boldsymbol{\sigma}] \tag{1.11}$$

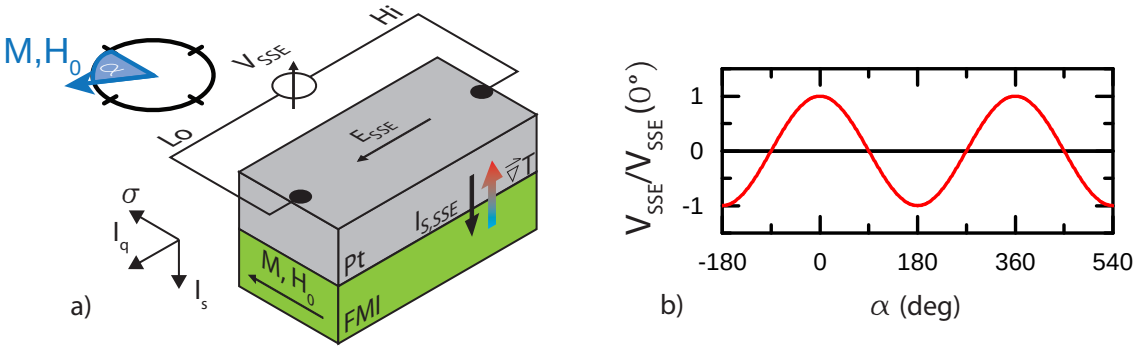

Figure 1.1: a) If a temperature gradient ∇T is applied to an FMI/Pt bilayer, a spin current $\mathbf{I}_{\mathrm{s,SSE}}$ is emitted along ∇T, this is called spin Seebeck effect. $\mathbf{I}_{\mathrm{s,SSE}}$ is transformed into a transverse charge current via the ISHE according to Eq. (1.11). b) The SSE voltage amplitude depends on the spin polarization $\boldsymbol{\sigma} \parallel \mathbf{M}$, so that we expect a $\cos(\alpha)$ dependence on the magnetization orientation.

In this thesis we will focus on bilayers consisting of a magnetic insulator and a normal metal Pt. In the magnetic insulator no charge can flow, but angular momentum can be transferred via magnons, leading to pure a spin current, which flows into the Pt layer and can then be detected via the ISHE.

1.2.2 Spin Seebeck Effect (SSE)

In addition to the SHE, there are other effects which can generate a spin current, for example the spin Seebeck effect (SSE). If a temperature gradient ∇T is applied to a FMI/Pt bilayer, the system relaxes by emitting a spin current along ∇T, as depicted in Fig.1.1 a). If we apply an external magnetic field $\mu_0 H_0$ large enough to overcome the magnetic anisotropies, the magnetization $\mathbf{M}$ is aligned with $\mu_0 H_0$. The generated spin current then has a spin polarization $\boldsymbol{\sigma}$ which is aligned with the magnetic field. According to Eq. (1.11), the spin current induces a transverse charge current in the Pt layer, and the SSE voltage V_{SSE} can be measured.

The SSE voltage therefore depends on the magnetization direction and if we rotate the magnetization direction in Fig. 1.1 a) by 90°, $\mathbf{I}_c$ flows along the short side of the sample, so that no SSE voltage can be detected in this configuration. We therefore expect a $\cos(\alpha)$ dependence on the magnetization orientation, as shown in Fig. 1.1 b). This is consistent with the sign of the SSE voltage determined by Schreier et al. [36] in YIG/Pt bilayers.

The SSE voltage changes sign when the magnetic field is inverted, and in particular, V_{SSE} follows the magnetic hysteresis when the external magnetic field is swept, so that we expect a voltage of the form [37]

$$V_{\mathrm{SSE}}(H_0) = B \cdot \left(\frac{\cosh\left(\frac{H_0 - H_\mathrm{c}}{s}\right)}{\sinh\left(\frac{H_0 - H_\mathrm{c}}{s}\right)} - \frac{s}{H_0 - H_\mathrm{c}} \right) + C \cdot x \tag{1.12}$$

where B is half the amplitude of the SSE hysteresis and $\mu_0 H_\mathrm{c}$ is the coercive field of the ferrimagnetic layer, as shown in Fig. 1.2. There is an additional slope C in case the magnetic film does not saturate, e.g. due to a paramagnetic contribution, as discussed in Sect. 5.2.1. This slope is exaggerated in Fig. 1.2 for better visibility, and in our samples $C \cdot \mu_0 H_0$ is negligible at small magnetic fields.

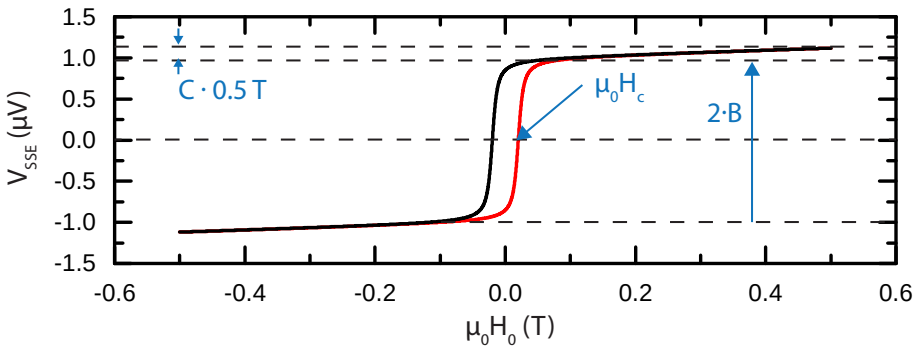

Figure 1.2: Hysteresis of the spin Seebeck voltage as a function of the external magnetic field $\mu_0 H_0$ showing the magnetic field upsweep in red and the magnetic field down sweep in black. The coercive field is marked by a blue arrow, as well as the SSE amplitude $2B$. The slope C of the hysteresis is exaggerated in this graph: $C\ \mu_0 H_0$ is in general negligible at small magnetic fields and becomes important only at high fields.

It was shown that the SSE spin current depends on the temperature difference $\Delta T = T_\mathrm{Pt} - T_\mathrm{FMI}$ between the electrons in the Pt and the magnons in the ferromagnetic insulator [18]

$$I_s^{\mathrm{SSE}} \propto \Delta T = T_\mathrm{Pt} - T_\mathrm{FMI} \tag{1.13}$$

There are different methods to generate such a temperature difference: the first SSE experiments were conducted with two heatbaths of different temperatures on opposite sample sides in order to generate a temperature gradient along the sample [3, 38]. At the Walther-Meissner-Institut, a laser was used to generate a local temperature gradient, allowing for spatially resolved SSE measurements [9, 39, 40].

In this thesis we will make use of the recently discovered current heating induced SSE (iSSE) [41, 42] developed again at WMI, where a dc current I_d is applied to the Pt layer in order to heat it. ΔT is then directly proportional to the temperature increase in the Pt layer [18, 43], which is in turn proportional to the heating power of the dc current, i.e. the Joule heating

$$P_{\text{Joule}} = V_{\text{d}} I_{\text{d}} = I_{\text{d}}^2 R \tag{1.14}$$

where R is the sample resistance. We therefore expect $V_{\text{SSE}} \propto I_{\text{d}}^2$.

The same effect as in the iSSE can be achieved by exposing the sample to microwave radiation: the rf electric field induces an ac current in the Pt layer and the dissipated electrical power induces a temperature gradient which also generates a spin Seebeck voltage.

1.2.3 Spin pumping

Another way to generate a spin current in a ferromagnetic insulator is the so called spin pumping. It was found that in FM/NM bilayer a precessing magnetization can also relax by pumping a spin current with a spin polarization σ along the external magnetic field into the NM [4], as shown in Fig. 1.3 a). This effect leads to an enhanced Gilbert damping [5], since the spin current provides an additional relaxation channel. The damping coefficient α_0 in Eq. (1.2) is then replaced by $\alpha' = \alpha_0 + \alpha_{\text{SP}}$, where α_{SP} is due to spin pumping.

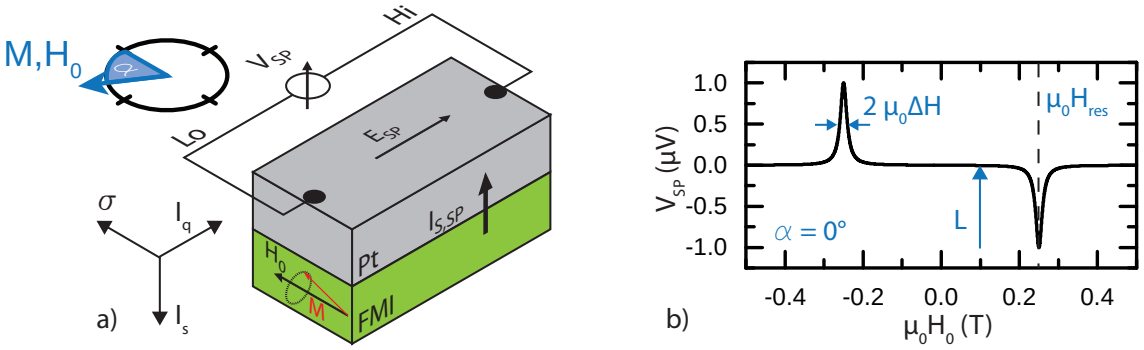

Figure 1.3: a) The precessing magnetization in the FMI layer emits a spin current with spin polarization along the external magnetic field, this is called spin pumping. The spin current flows into the Pt layer and is transformed into a charge current via the ISHE, so that the spin pumping voltage V_{SP} can be measured. b) V_{SP} attains its maximum at the FMR field $\mu_0 H_0$ and has a Lorentzian line shape with the FMR linewidth. Since the spin pumping voltage depends on the spin polarization direction, it changes sign upon field inversion.

The spin current originating from spin pumping is again transformed into a charge current via the ISHE (see Sect. 1.2.1) in the Pt layer, giving rise to a voltage [14, 15, 44]

$$V_{\text{SP}} = \frac{-e\ \alpha_{\text{SH}}\ \lambda_{\text{SD}}\ \tanh(t_{\text{NM}}/(2\lambda_{\text{SD}}))}{\sigma_{\text{NM}} t_{\text{NM}}} g_{\uparrow\downarrow}\ \nu_{\text{MW}}\ l\ P\ \sin^2\Theta \tag{1.15}$$

with e the electron charge, λ_{SD} the spin diffusion length in NM, $g_{\uparrow\downarrow}$ the spin mixing

conductance, l the sample length, ν_{MW} the microwave frequency, Θ the magnetization precession cone angle, P is a correction factor taking into account the ellipticity of the magnetization precession [14, 45] and t_{NM} the normal metal film thickness, σ_{NM} the normal metal conductivity.

According to Eq. (1.15) the spin current amplitude is at its maximum when the precession angle Θ is at its maximum, i.e. when the magnetization is driven by a microwave magnetic field in ferromagnetic resonance. The spin pumping voltage depends on the precession angle and is therefore symmetric with respect to the resonance field $\mu_0 H_{\mathrm{res}}$, so that we expect a Lorentzian lineshape of the form [14, 46]

$$V_{\mathrm{SP}}(H_0) = L \cdot \frac{\Delta H^2}{(H_0 - H_{\mathrm{res}})^2 + \Delta H^2} - L \cdot \frac{\Delta H^2}{(H_0 + H_{\mathrm{res}})^2 + \Delta H^2} \tag{1.16}$$

with L the peak height, i.e. the spin pumping amplitude, H_0 the external magnetic field, H_{res} the FMR resonance field and ΔH the FMR half linewidth at half maximum, as depicted in Fig. 1.3 b). Equation (1.16) gives the spin pumping amplitude for positive and negative fields: when the magnetic field is inverted, the spin current polarization is inverted as well and the voltage changes sign. The spin current from spin pumping and SSE flow into opposite direction, since for spin pumping it is the ferrimagnetic layer that is excited and in the SSE, the Pt layer is heated. The spin pumping amplitude L is therefore negative for positive magnetic field, which is consistent with the absolute sign of the spin pumping voltage determined in Ref. [36].

In an FMR experiment the precession angle Θ from Eq. (1.15) can be calculated as [15]

$$\Theta = h_{\mathrm{MW}}/\Delta H \tag{1.17}$$

with h_{MW} the microwave magnetic field and ΔH the FMR half linewidth at half maximum, as long as the precession cone angle is small. In the small angle approach we obtain

$$\sin^2\Theta \approx \Theta^2 = (h_{\mathrm{MW}}/\Delta H)^2 \tag{1.18}$$

During measurements at a constant microwave power and therefore constant h_{MW}, the spin pumping amplitude L in resonance is proportional to $1/(\Delta H^2)$. Since we will be investigating spin pumping in samples with different FMR linewidths, and also observe a strong temperature dependence of the FMR linewidth in some samples, a useful parameter allowing us to compare all results is $L(\mu_0 \Delta H)^2$, which we call the spin pumping efficiency. We will see in Chapter 4, that this spin pumping efficiency is indeed approximately constant in our different samples.

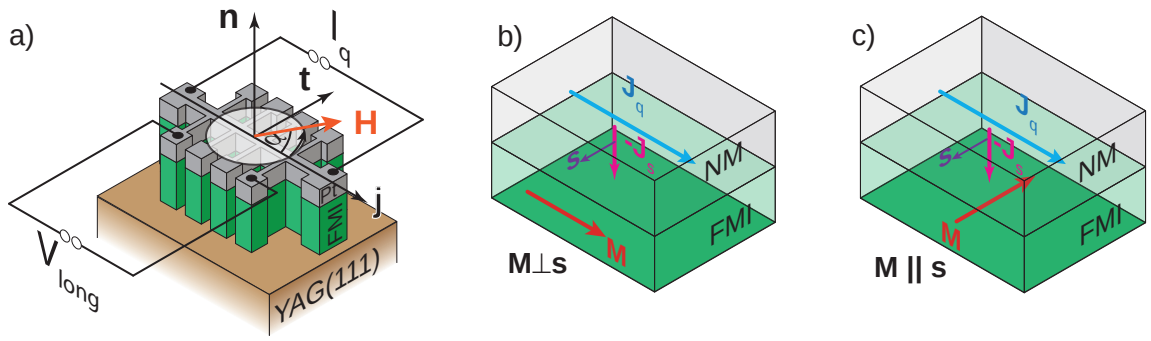

Figure 1.4: a) Measurement scheme used for the SMR effect in a FMI/Pt bilayer: a longitudinal dc current is applied to the Hall bar along **j** and and the longitudinal resistance R_{long} is measured as a function of the in plane magnetic field orientation α. b) The charge current density $\mathbf{J}_c$ induces a spin current via the SHE which can either be absorbed ($\mathbf{M}\perp\mathbf{s}$) or c) reflected ($\mathbf{M} \parallel \mathbf{s}$) at the interface, depending on the relative orientations of $\mathbf{M}$ and $\mathbf{s}$. The reflected spin current is then converted into a charge current via the ISHE and $R_{\mathbf{M}\perp\mathbf{s}} > R_{\mathbf{M}\parallel\mathbf{s}}$ leading to a magnetoresistive effect. Figure taken from Ref. [6]

1.2.4 Spin Hall magnetoresistance (SMR)

The recently discovered spin Hall magnetoresistance [6–8, 20, 47, 48] is a magnetoresistive effect visible in FMI/NM bilayers. A dc charge current I_q is applied along the Hall bar shown in Fig. 1.4 a) and via the SHE (see Sect. 1.2.1) induces a spin current with spin polarization σ which flows into the FMI. If σ is perpendicular to the magnetization $\mathbf{M}$ of the ferromagnet as depicted in Fig. 1.4 b), the spin current can exert torque and transfer angular momentum to $\mathbf{M}$, i.e. the spin current is absorbed. If $\sigma \parallel \mathbf{M}$ as shown in Fig. 1.4 c), no angular momentum can be transferred and the spin current is reflected at the interface and transformed back into a charge current via the ISHE (see Sect. 1.2.1). We then expect a larger longitudinal resistance if the current is absorbed and a lower resistance if not, such that [6]

$$R_{\mathbf{M}\perp\mathbf{s}} > R_{\mathbf{M}\parallel\mathbf{s}} \tag{1.19}$$

The longitudinal resistance can be written as [6, 7]

$$R_{\text{long}} = R_0 + R_1 m_t^2 \tag{1.20}$$

with $R_0 = R_{\mathbf{M}\perp\mathbf{s}}$ the larger resistance, $R_1 = R_{\mathbf{M}\parallel\mathbf{s}} - R_{\mathbf{M}\perp\mathbf{s}}$ and m_t the projection of $\mathbf{M}$ on the $\mathbf{t}$ axis in Fig. 1.4 a), so that R_1 is in general negative [6]. When rotating the external magnetic field and assuming that $\mathbf{M} \parallel \mathbf{H}$, we expect a longitudinal resistance dependence on the magnetic field orientation α of the form

$$R_{\text{long}} = R_0 + R_1 \cos^2\alpha \tag{1.21}$$

The assumption $\mathbf{M} \parallel \mathbf{H}$ is valid as long as crystalline and shape anisotropies can be neglected, i.e. at sufficiently high external magnetic fields.

The positive SMR ratio is then defined as [6, 8]

$$- R_1/R_0 \tag{1.22}$$

1.3 Microwave rectification

We have discussed microwave driven spin pumping in FM/Pt bilayers in Sect. 1.2.3 which gives rise to a symmetric signal with respect to the ferromagnetic resonance field. There are however other effects which can yield a voltage in resonance, e.g. microwave rectification. The origin of the microwave rectification voltage can be explained in a simple picture: when the sample is exposed to microwave radiation with a frequency ω, the rf magnetic field drives the magnetization precession with the same frequency. If the sample yields magnetoresistive effects, the sample resistance is time dependent due to magnetization precession as well, so that $R(t) = R_0 + R_S \cos(\omega t)$. The rf electric field on the other hand induces an ac current in the Pt layer of the form $I(t) = I_0 \cos(\omega t + \varphi)$, with φ the phase difference between ac current and resistance. This leads to a voltage

$$\begin{aligned} V_{\text{rect}} &= I(t) \cdot R(t) = (I_0 \cos(\omega t + \varphi)) \cdot (R_0 + R_S \cos(\omega t)) \\ &= I_0 R_0 \cos(\omega t + \varphi) + I_0 R_S \cos(\omega t + \varphi) \cos(\omega t) \\ &= I_0 R_S/2 \cos(\varphi) + I_0 R_0 \cos(\omega t + \varphi) + I_0 R_S/2 \cos(2\omega t + \varphi) \end{aligned} \tag{1.23}$$

We therefore obtain an additional dc voltage from microwave rectification proportional to $\cos\phi$.

The concept of microwave rectification in conducting ferromagnets with an anisotropic magnetoresistance (AMR) is well established and experimentally confirmed [14, 46, 49, 50]. In this thesis only ferrimagnetic insulators covered by a Pt layer are used, so that we should not observe AMR rectification. However, as discussed in Sect. 1.2.4, a magnetoresistive effect (SMR) can also be observed in FMI/Pt bilayers and according to Iguchi et al. [51] leads to an SMR rectification voltage of the form

$$V_{\text{rect, SMR}} \propto \cos(\varphi_0) \frac{\Delta H^2}{(H - H_{\text{res}})^2 + \Delta H^2} - \sin(\varphi_0) \frac{\Delta H (H - H_{\text{res}})}{(H - H_{\text{res}})^2 + \Delta H^2} \tag{1.24}$$

with $\mu_0 H_{\text{res}}$ the FMR field, $\mu_0 \Delta H$ the FMR half linewidth and φ_0 the phase difference between electric and magnetic microwave field.

The microwave rectification therefore yields a symmetric and an antisymmetric dc voltage contribution with respect to the FMR field, depending on the phase φ_0. In a high Q microwave cavity as used in this thesis $\varphi_0 \approx 90°$ [51, 52], so that we expect to see only antisymmetric rectification of the form [49]

$$V_{\text{rect}}(H_0) = D \cdot \frac{\Delta H (H_0 - H_{\text{res}})}{(H_0 - H_{\text{res}})^2 + \Delta H^2} + D \cdot \frac{\Delta H (H_0 + H_{\text{res}})}{(H_0 + H_{\text{res}})^2 + \Delta H^2} \tag{1.25}$$

with D the amplitude of the microwave rectification voltage, as depicted in Fig. 1.5.

Similar to the spin pumping efficiency $L(\mu_0 \Delta H)^2$, as defined in Sect. 1.2.3, we can also define a rectification efficiency. According to Ref. [51], the SMR rectification amplitude D is proportional to $1/\Delta H$, so that we obtain the microwave rectification efficiency $D(\mu_0 \Delta H)$.

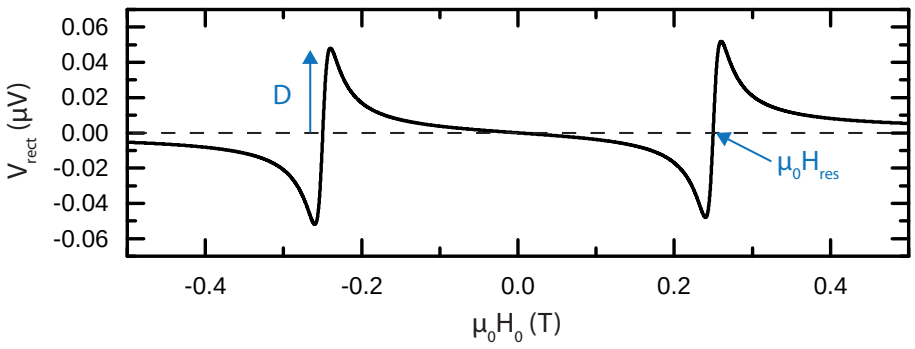

Figure 1.5: SMR Microwave rectification voltage in a cavity with $\phi_0 = 90°$, so that the rectification voltage is purely antisymmetric around the FMR field $\mu_0 H_{\text{res}}$.

1.4 Total DC voltage

In the previous Sections we have discussed different resonant and non resonant contributions to the dc voltage in a FMI/Pt bilayer. V_{DC} shown in Fig. 1.6 is a superposition of the non resonant SSE voltage (see Sect. 1.2.2) and the resonant voltage consisting of symmetric spin pumping (see Sect. 1.2.3) and an antisymmetric rectification voltage (see Sect. 1.3):

$$
\begin{aligned}
V_{\mathrm{DC}}(H_0) &= B \cdot \left(\frac{\cosh\left(\frac{H_0 - H_c}{s}\right)}{\sinh\left(\frac{H_0 - H_c}{s}\right)} - \frac{s}{H_0 - H_c} \right) + C \cdot H_0 \\
&\quad + L \cdot \frac{\Delta H^2}{(H_0 - H_{\mathrm{res}})^2 + \Delta H^2} + D \cdot \frac{\Delta H (H_0 - H_{\mathrm{res}})}{(H_0 - H_{\mathrm{res}})^2 + \Delta H^2} \\
&\quad - L \cdot \frac{\Delta H^2}{(H_0 + H_{\mathrm{res}})^2 + \Delta H^2} + D \cdot \frac{\Delta H (H_0 + H_{\mathrm{res}})}{(H_0 + H_{\mathrm{res}})^2 + \Delta H^2}
\end{aligned} \tag{1.26}
$$

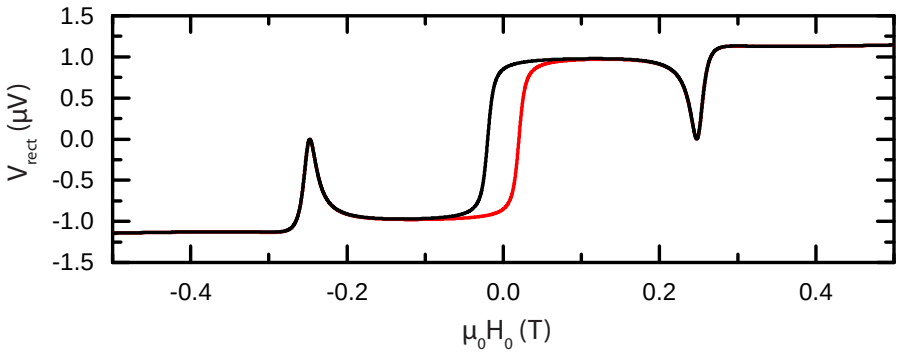

Figure 1.6: Total DC voltage: superposition of the contributions from spin Seebeck effect V_{SSE}, spin pumping V_{SP} and antisymmetric microwave rectification V_{rect}.

Equation (1.26) is used as a fit function for the experimental data in Chap. 4.

1.5 Magnetically compensated materials

We have discussed different spinelectronics effects in ferromagnetic insulator/Pt bilayers, and in this thesis we use, among other materials, the magnetically compensated material Gadolinium Iron Garnet (GdIG) as a ferromagnetic insulator. GdIG is composed of three sublattices: a tetrahedrally coordinated Fe^{3+} sublattice (d), an octahedrally cordinated Fe^{3+} sublattice (a) and a dodecahedrally coordinated Gd^{3+} sublattice (c). Both Fe^{3+} sublattices are antiferromagnetically coupled to each other, the Gd^{3+} sublattice is antiferromagnetically coupled to the octahedral Fe^{3+} sublattice and ferromagnetically coupled to the tetrahedral Fe^{3+} [23]. The corresponding exchange energies are given in Chapter 3. The temperature dependence of the net Fe magnetization given by $M_d - M_a$ is shown in Fig. 1.7 a) taken from Ref. [23][1] and the magnetization of the Gd^{3+} sublattice M_c which is antiparallel to the net Fe sublattice is depicted as well. At high

[1]Note that the magnetizations in this figure are given in cgs units and are all positive, so that the relative direction of the sublattices is added through a minus sign.

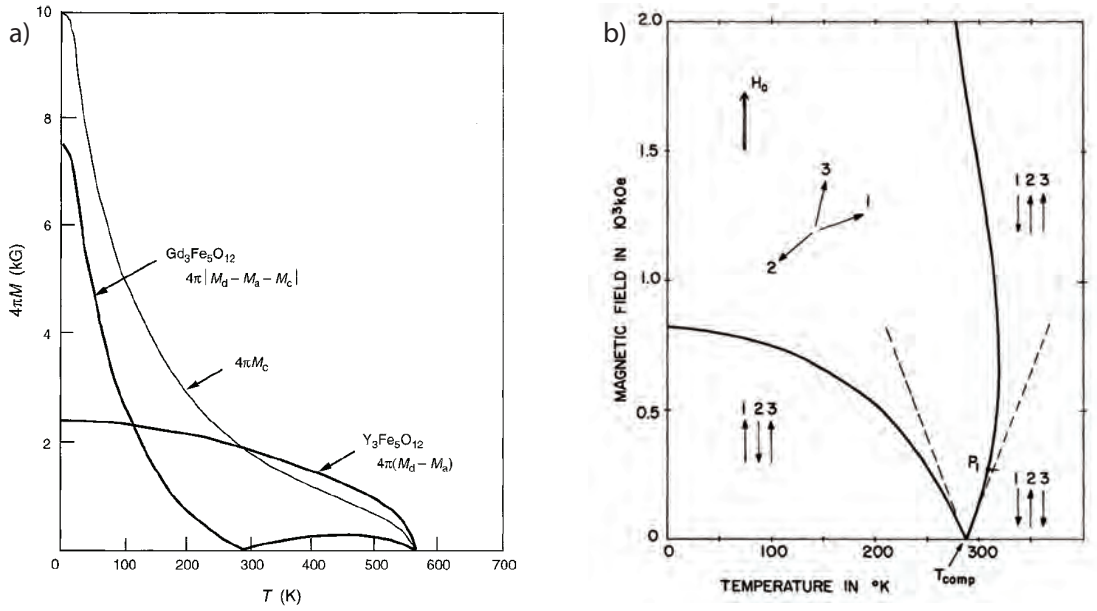

Figure 1.7: a) Magnetization of the net Fe^{3+} sublattice as well as the Gd^{3+} sublattice in GdIG. The $|M_{\text{tot}}|$ yields a magnetization compensation temperature at 280 K [23]. b) Magnetic field vs temperature phase diagram in GdIG: above a critical magnetic field H_{c1} represented by a black line, the sublattice magnetizations enter the spin canting phase. The critical field decreases strongly around $T_{\text{comp, M}}$. [53]

temperatures, the net Fe magnetization dominates, down to the magnetization compensation temperature $T_{\text{comp, M}} = 280\,\text{K}$, where $M_d - M_a = M_c$ and the total magnetization $|M_{\text{tot}}| = |M_d - M_a - M_c|$ goes to zero. Below $T_{\text{comp, M}}$, M_c dominates, so that $|M_{\text{tot}}|$ increases again. If no external magnetic field is applied, the total magnetization M_{tot} changes sign at $T_{\text{comp, M}}$. However, in a finite external magnetic field $\mu_0\mathbf{H}_0$, the total sample magnetization aligns with $\mu_0\mathbf{H}_0$, so that at $T_{\text{comp, M}}$ all sublattice magnetizations are inverted. In a first approximation, the magnetization curve in an external magnetic field therefore behaves like $|M_{\text{tot}}|$.

The temperature dependent GdIG magnetization as given in Fig. 1.7 a) is accurate, as long as we assume that all three sublattices are always either parallel or antiparallel to each other. However, if the external magnetic field exceeds the critical field H_{c1} the magnetizations are not collinear anymore but form an angle and enter the so called spin canting phase [54, 55].

Bernasconi et al. calculated the magnetic field vs temperature phase diagram in GdIG (neglecting magnetic anisotropies), as shown in Fig. 1.7 b) [53]. The critical field H_{c1} is represented by a black line in Fig. 1.7 b): below H_{c1} the sublattice magnetizations represented by arrows 1 to 3 are collinear and above H_{c1}, the magnetizations are canted. This means that the sublattice magnetizations are no longer aligned with external magnetic

field, but are oriented nearly perpendicular, with a slight tilt to $\mu_0\mathbf{H}_0$. H_{c1} was calculated to be of the order of 80 T in GdIG at temperatures far below the magnetization compensation temperature. Near $T_{\text{comp, M}}$ however, the critical field decreases and spin canting can be achieved with more accessible magnetic field strengths. The critical field is in fact zero at $T_{\text{comp, M}}$ if anisotropies are neglected, but is again finite even at $T_{\text{comp, M}}$, if there is a finite magnetic anisotropy.

During temperature dependent measurements, when passing $T_{\text{comp, M}}$ in a very weak magnetic field, the magnetizations of all three sublattices are reversed. However, at magnetic fields larger than $\mu_0 H_{c1}$, spin canting occurs and the sublattice magnetization reorientation around $T_{\text{comp, M}}$ takes place in a finite temperature interval. The width of this interval increases with the applied magnetic field [53, 54].

We will now discuss what happens during an FMR experiment in a magnetically compensated material. In general the antiferromagnetic coupling between sublattices is large, so that in the so called normal mode the sublattice magnetizations are rigidly coupled. The angle between the magnetizations is 180° and they act like a net magnetization precessing about the external magnetic field. In an FMR experiment, the compensated garnet can then be treated just like a ferromagnet with the resonance frequency ω_0 from Eq. (1.1) where γ is replaced by an effective gyromagnetic ratio [24, 56–58]

$$\gamma_{\text{eff}} = \frac{M}{L} = \frac{M_{d,Fe} - M_{a,Fe} - M_{c,Gd}}{L_{d,Fe} - L_{a,Fe} - L_{c,Gd}} \tag{1.27}$$

with the sublattice magnetizations $M_i > 0$, the sublattice angular momenta $L_i = M_i/\gamma_i$ and the sublattice gyromagnetic ratios $\gamma_i < 0$. If all $\gamma_i = \gamma$ are equal, Eq. (1.27) simplifies to γ and is independent of temperature. However, if the γ_i are only slightly different, M and L have different compensation temperatures [24], and γ_{eff} diverges at the angular momentum compensation point. These effects related to γ_{eff} will be discussed in more detail in Sect. 3.2.

There is a second FMR mode which can be excited, where each magnetization does not precess around the external magnetic field, but around the exchange field provided by the other sublattices. This mode is called exchange mode and is similar to the antiferromagnetic resonance mode [59]. In a two sublattice model, the frequency of the exchange mode is $\omega_e \approx \lambda(\gamma_1 M_1 - \gamma_2 M_2)$ with λ the molecular field constant, and therefore ω_e is of the order of a few 100 GHz [60] and much larger than the normal mode frequency ω_0, which is given by the external magnetic field.

At the magnetization compensation temperature, $M_1 \approx M_2$ and the exchange mode moves to a lower frequency of a few GHz, so that it is more accessible with ordinary microwave frequencies [57].

Chapter 2

Sample fabrication and characterization

2.1 Gadolinium Iron Garnet

The compensated magnetic material predominantly used in this thesis is Gadolinium Iron Garnet ($Gd_3Fe_5O_{12}$, GdIG). The sublattice structure and magnetization as a function of temperature for a typical compensated garnet have been described in Sect. 1.5.

Our measurements were conducted in GdIG thin films deposited onto single crystalline [111]-oriented Yttrium Aluminum Garnet substrates via pulsed laser deposition (PLD) [61, 62]. After the PLD process, the ferrimagnetic thin films were covered *in situ* by a few nanometers of Pt, using electron beam evaporation. The sample fabrication and optimization were conducted by Francesco Della Coletta in the course of his Master's thesis [63]. The crystal quality as well as film thicknesses were deduced from X-ray diffractometry (XRD). The magnetization and compensation temperature were determined via SQUID magnetometry. Growth parameters were optimized in order to achieve good crystalline quality and a compensation temperature close to the value for bulk material, $T_{\mathrm{comp,\,M}} = 280\,\mathrm{K}$ for GdIG [23].

For spin pumping measurements a small ferromagnetic resonance linewidth (low magnetization damping) is desirable. Qualitatively speaking, for a FMR half linewidth larger than 100 mT, measuring a clear signal is challenging. Therefore an important criterion for good samples is a small FMR linewidth. Preliminary FMR experiments were conducted in order to characterize our thin films in terms of FMR linewidth. Since in a compensated garnet the FMR linewidth diverges at the compensation temperature (see Sect. 4.2.2.4 and 4.2.3.4) and T_{comp} varies in different materials, the parameter used for comparison is the linewidth at a temperature far away from the compensation region.

The GdIG/Pt thin film with the best parameters has a linewidth of 15 mT at the cryostat temperature (see Sect. 4.1.4) $T_{\mathrm{cryo}} = 80\,\mathrm{K}$ at a microwave frequency of 9.7 GHz for an in plane magnetic field as shown in Fig. 4.25 and discussed in Sect. 4.2.3.4. This sample was grown using a substrate temperature of 500 °C, an oxygen atmosphere of 1.25×10^{-2} mbar and an energy fluence of the KrF excimer laser of $1.5\,\mathrm{J/cm^2}$ at the target surface. The magnetization compensation temperature is $T_{\mathrm{comp,\,M}} = 279\,\mathrm{K}$, which

is in good agreement with literature [23]. X-ray diffractometry measurements yield a Pt layer thickness of 5.3 nm. The GdIG film thickness could not be determined from XRD measurements, probably due to a large surface roughness of the film. But from the number of laser pulse packets during the PLD process in comparison with other samples, the film thickness is assumed to be about 50 nm. A $2.5 \times 5\,\mathrm{mm}^2$ was cut from the finished bilayer sample for use in our experiments.

2.2 In and Y doped Gadolinium Iron Garnet

The disadvantage of pure GdIG is that $T_{\mathrm{comp,\,M}}$ is of the order of 280 K, close to room temperature [23], and that the temperature range in which the divergence of FMR linewidth and effective g-value take place is quite broad in our samples, about ± 80 K around T_{comp}, as discussed in detail in Sect. 4.2.3.4. Our setup is laid out for measurements between 4 K and 300 K and heating above room temperature is challenging (see Sect. 4.1.3). Therefore a sample with a lower compensation temperature and a narrower divergence region is desirable for our measurements.

For this purpose, the WMI growth team grew a thin film out of In and Y doped GdIG, viz. $(Gd_2Y)(Fe_4In)O_{12}$ (InYGdIG). The paramagnetic Y^{3+} is here substituted for Gd^{3+} with spin 7/2, which reduces the Gd-moment. The In^{3+}, which has no magnetic moment either, substitutes spin 5/2 Fe^{3+} ions on the a lattice [64], i.e. those Fe atoms with the smaller magnetic moment, so that the net Fe-moment is increased. In this system lower temperatures are necessary for the Gd sublattice to compensate the net Fe-moment and therefore the compensation temperature will be lower [65, 66].

It was also shown that the In^{3+} substitution strongly decreases the ferromagnetic resonance linewidth [66]. This can be explained by anisotropy arguments: the magnetocrystalline anisotropy constant K_1 is determined by the amount of Fe^{3+} ions on the a and d sites. Since the a site contributes more to the anisotropy, reducing the a-site moment also reduces the anisotropy. The anisotropic linewidth broadening ΔH_{ani} is proportional to K_1^2/M^3 [67]. The change in K_1 is larger than the change in saturation magnetization, so that the linewidth is decreased in the doped material [66, 68].

The same optimization processes as described in Sect. 2.1 were conducted in this material by Sascha Frölich in the course of his Bachelor's thesis [69]. The sample used for our experiments was grown onto single crystalline [111]-oriented Yttrium Aluminum Garnet using a substrate temperature of 500 °C, an oxygen atmosphere of 2.5×10^{-2} mbar and an energy fluence of the KrF excimer laser of $2\,\mathrm{J/cm}^2$ at the target surface. The InYGdIG layer thickness determined by XRD measurements is 61.5 nm and the Pt layer has a thickness of 3.6 nm. The sample dimensions are $1.9 \times 5\,\mathrm{mm}^2$. The compensation temperature is $T_{\mathrm{comp,\,M}} = 85$ K and the FMR half linewidth is 5 mT at room temperature at a microwave frequency of 9.7 GHz for in plane magnetic field, as discussed in detail in

Sect. 4.2.2. This is one third of the GdIG linewidth determined in Sect. 4.2.3.4. Therefore, most measurements will be conducted in the InYGdIG thin film.

2.3 Yttrium Iron Garnet reference sample

As a reference sample, a well known material, i.e. Yttrium Iron Garnet ($Y_3Fe_5O_{12}$, YIG), is used. The effects relevant for the discussion here, namely FMR, spin pumping [16, 17, 70], spin Seebeck effect [9, 10, 38, 41, 43] and spin Hall magnetoresistance [6–8], have thoroughly been investigated in YIG thin films.

The YIG sample was also grown onto single crystalline [111]-oriented Yttrium Aluminium Garnet, with a substrate temperature of 500 °C, an oxygen atmosphere of 2.5×10^{-2} mbar and an energy fluence of the KrF excimer laser of $2\,\mathrm{J/cm^2}$ at the target surface. The YIG and Pt layers have a thickness of 59.5 nm and 9.7 nm respectively, the sample dimensions are $2.45 \times 5\,\mathrm{mm^2}$. This sample was grown by Stephan Altmannshofer in the course of his Master's thesis [71].

Sample	t_{garnet} (nm)	t_{Pt} (nm)	$T_{\mathrm{comp,\,M}}$(K)
GdIG/Pt	50	5.3	279
InYGdIG/Pt	61.5	3.6	88
YIG/Pt	59.5	9.7	-

Table 2.1: List of the samples examined in this thesis with layer thicknesses from XRD and magnetization temperature $T_{\mathrm{comp,\,M}}$ determined from SQUID magnetometry.

Chapter 3

Simulation of magnetization, effective g value and FMR field in a magnetically compensated material

We will now present a calculation based on the mean field approximation allowing us to determine the temperature dependence of magnetization, effective g value, and ferromagnetic resonance field in magnetically compensated garnets. We will later compare the results to the experimental data analyzed in Chap. 4.

The simulation was mainly developed by J. Lotze in the course of his PhD thesis[1] and this chapter shall give an overview of the approaches and calculations which were used.

3.1 Calculation of the magnetization

We start with the calculation of the sublattice magnetizations based on the work by G. Dionne about molecular field coefficients of Gd^{3+} substituted YIG [72, 73].

In a ferrimagnet the temperature dependence of the magnetization of the different sublattices i can be calculated as

$$M_i(T) = M_i(0)B_{S_i}(x_i) \tag{3.1}$$

with $M_i(0)$ the magnetization at $T = 0$, and $B_{S_i}(x)$ the Brillouin functions for the sublattices i, respectively. We are interested in magnetically compensated Gadolinium Iron Garnet (GdIG) consisting of three sublattices, viz. a tetrahedral Fe sublattice (d), an octahedral Fe sublattice (a) and a dodecahedral Gd sublattice (c), as described in (ref Theory). $M_{d,Fe}$ and $M_{a,Fe}$ are antiferromagnetically coupled, $M_{c,Gd}$ is antiferromagnetically coupled to $M_{d,Fe}$ and ferromagnetically coupled to $M_{a,Fe}$ [23]. This can also be seen in the sign of the exchange energies given in Table 3.2. For weak magnetic fields we can assume that all three sublattices are either parallel or antiparallel to each other over the whole temperature range (see Sect. 1.5). The total magnetization is then given by

[1] PhD thesis in progress.

$$M_{\mathrm{tot}}(T) = M_d(T) - M_a(T) - M_c(T) \tag{3.2}$$

with $M_i > 0$ the absolute values of the sublattice magnetizations.

The Brillouin function for sublattice i is [74]

$$B_{S_i}(x) = \frac{2S_i+1}{2S_i}\coth\left(\frac{2S_i+1}{2S_i}x_i\right) - \frac{1}{2S_i}\coth\left(\frac{1}{2S_i}x_i\right) \tag{3.3}$$

with [72, 73]

$$x_a = \frac{S_a g_a \mu_B}{kT}\left(N_{ad}M_d + N_{aa}M_a + N_{ac}M_c + \mu_0 H_0\right) \tag{3.4}$$

$$x_d = \frac{S_d g_d \mu_B}{kT}\left(N_{dd}M_d + N_{da}M_a + N_{dc}M_c + \mu_0 H_0\right) \tag{3.5}$$

$$x_c = \frac{S_c g_c \mu_B}{kT}\left(N_{cd}M_d + N_{ca}M_a + N_{cc}M_c + \mu_0 H_0\right) \tag{3.6}$$

with N_{ij} the molecular field coefficients and $S_{i,j}$ the spin quantum numbers of the ions for sublattices i,j, μ_B the Bohr magneton, k the Boltzmann constant, g_i the g factor for the ions on sublattice i and $\mu_0 H_0$ the external magnetic field. $N_{ij}M_j$ describes the molecular field generated by sublattice i acting on the magnetization of sublattice j. The original formulas from Ref. [72, 73] do not contain an external magnetic field $\mu_0 H_0$, but this term can be added to the molecular fields in order to describe the behaviour of a magnetic material in an effective magnetic field [55, 74].

We use the following molecular field coefficients N_{ij} from Ref. [73] (in cgs units $\mathrm{mol\,cm^{-3}}$):

N_{dd}	N_{aa}	$N_{ad} = N_{da}$	$N_{dc} = N_{cd}$	$N_{ac} = N_{ca}$	N_{cc}
-30.4	-65.0	97.0	6.0	-3.44	0

Table 3.1: Molecular field coefficients in GdIG

The molecular field coefficients N_{ij} are related to the exchange constants J_{ij} by:

$$N_{ij} = \frac{z_{ij}}{n_j}\frac{2J_{ij}}{g_i g_j \mu_B^2} \tag{3.7}$$

with z_{ij} the number of nearest-neighbour j ions and n_j the number of j ions per mole. The exchange constants J_{ij} in T are then given by:

The molecular fields generated by the magnetic moments are therefore in general much stronger than the external magnetic field, so that in Eq. (3.4) to (3.6), the influence of $\mu_0 H_0$ should be small[2].

[2]This simulation however yields a magnetic field dependence of the magnetization compensation

J_{dd}	J_{aa}	J_{ad}	J_{dc}	J_{ac}	J_{cc}
-25.5	-18.2	54.2	10.1	-1.9	0

Table 3.2: Exchange constants J_{ij} in GdIG in T.

The molecular field constants are dependent on the concentration of magnetic ions in each sublattice, i.e. depend on doping. In [72, 73] the molecular field constants for (Y_z Gd_{3-z}) (In_x Fe_{2-x}) (In_y Fe_{3-y}) O_{12} have been determined to:

$$N_{dd}(k_a) = -30.4(1 - 0.87k_a) \tag{3.8}$$
$$N_{aa}(k_d) = -65(1 - 1.26k_d) \tag{3.9}$$
$$N_{ad}(k_a, k_d) = 97.0(1 - 0.25k_a - 0.38k_d) \tag{3.10}$$

where $k_d = y/3$, $k_a = x/2$ and $k_c = z/3$. To a first approximation, N_{dc}, N_{ac} and N_{cc} are considered to be independent of doping.

Inserting Eq. (3.4) to (3.6) into Eq. (3.1) yields an implicit equation, in which the M_i depend on all three sublattice magnetizations. This set of equations can be solved numerically for the three materials discussed in this thesis, viz. GdIG, YIG and InYGdIG.

In Ref. [72, 73], $g_i = 2$ is used for all sublattices and the calculation yields $T_{\text{comp, M}} = 280\,\text{K}$ for $H_0 = 0$. g_i close to 2 is a good approximation, since the Fe^{3+} and the Gd^{3+} ions carry only spin angular momentum and no orbital angular momentum. However, the g values for Fe^{3+} in YIG on the tetrahedral site d and on the octahedral site a were experimentally determined to be $g_{\text{Fe, d}} = 2.0047$ and $g_{\text{Fe, a}} = 2.003$ [25, 75]. The g value for Gd^{3+} was determined experimentally to be $1.9906 \leq g_{\text{Gd, c}} \leq 1.9925$ in CaF_2 [25, 76]. Rodrigue et al. extracted $g_{\text{Gd, c}} = 1.994 \pm 0.005$ from measurements in GdIG [77]. As discussed in Sect. 1.5, when the g_i are slightly different from each other, the effective gyromagnetic ratio from Eq. (1.27) diverges at $T_{\text{comp, L}}$, which is consistent with experimental results [78, 79].

We therefore use $g_{\text{Fe, d}} = 2.0047$, $g_{\text{Fe, a}} = 2.003$ and $g_{\text{Gd, c}} = 1.994$ in our calculation and apply an external field of $\mu_0 H_0 = 1\,\text{T}$. We obtain the magnitudes of the three sublattice magnetizations in GdIG, $M_{d,Fe}$ in blue, $M_{a,Fe}$ in red and $M_{c,Gd}$ in green, as shown in Fig. 3.1 a). The total magnetization $M_{\text{tot}} = |M_{d,Fe} - M_{a,Fe} - M_{c,Gd}|$ in an external magnetic field $\mu_0 H_0 = 1\,\text{T}$ is shown in Fig. 3.1 b), where the directions of the Gd sublattice and the net Fe sublattice magnetizations $M_{d,Fe} - M_{a,Fe}$ are represented by

temperature, which was not observed experimentally and has to be further investigated.

green and purple arrows respectively.

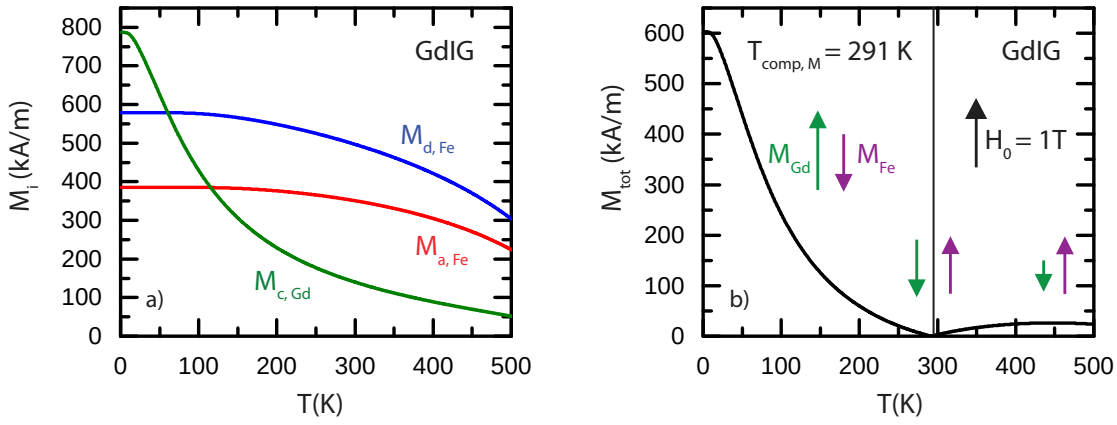

Figure 3.1: a) Magnetization magnitude of the Fe sublattices a (red) and d (blue) as well as the Gd magnetization c (green) in GdIG calculated using a mean field approach. b) Total magnetization $M_{\mathrm{tot}} = |M_{d,Fe} - M_{a,Fe} - M_{c,Gd}|$ in an external magnetic field $\mu_0 H_0$ represented by a black arrow. The magnetization directions of the Gd sublattice and the net Fe sublattice are represented by green and purple arrows respectively. A black line indicates the magnetization compensation temperature at $T_{\mathrm{comp,\,M}} = 291\,\mathrm{K}$.

With $\mu_0 H_0 = 1\,\mathrm{T}$ and the g values given above, the calculation yields a magnetization compensation temperature $T_{\mathrm{comp,\,M}} = 291\,\mathrm{K}$ (black line in Fig. 3.1 b)), which is higher than the value of $T_{\mathrm{comp,\,M}} = 280\,\mathrm{K}$ for $\mu_0 H_0 = 0\,\mathrm{T}$ [72, 73], but still consistent with different experimental values between $T_{\mathrm{comp,\,M}} = 279\,\mathrm{K}$ and $296\,\mathrm{K}$ [23, 77, 79, 80]. This magnetic field dependence of the magnetization compensation temperature was not observed experimentally in SQUID magnetometry measurements in GdIG thin films, and we find $T_{\mathrm{comp,\,M}} = 279\,\mathrm{K}$ in our GdIG film, independent on the external magnetic field. These deviations from the experimental observations might be due to the fact that the simulation is based on the assumption that the sublattice magnetizations are always collinear. As discussed in Sect. 1.5, this assumption is not valid anymore at $T_{\mathrm{comp,\,M}}$ for finite external magnetic fields due to spin canting. Therefore the simulation cannot reproduce the exact behaviour of the magnetization around the magnetization compensation point, but nevertheless gives a good idea of the temperature dependence of the magnetization and yields a magnetization compensation temperature, which lies within the range of experimental values.

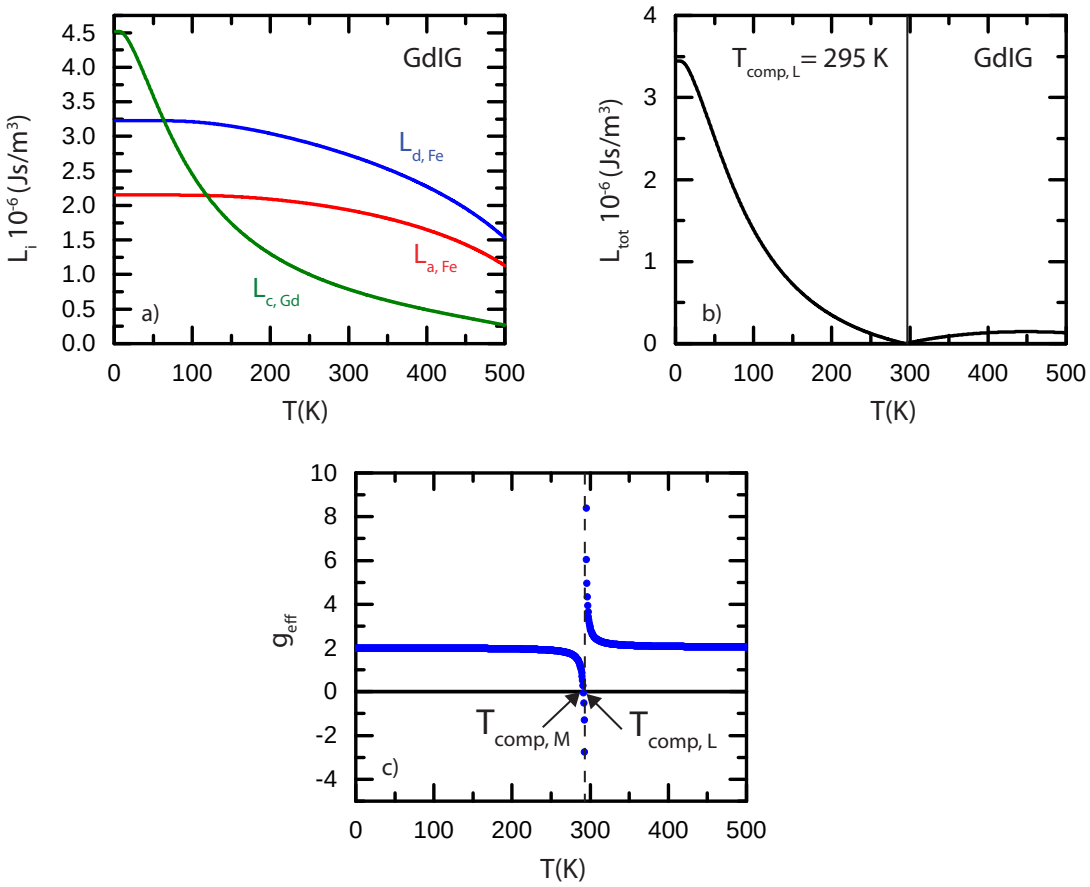

Figure 3.2: a) Angular momentum of the Fe sublattices a (red) and d (blue) as well as the Gd angular momentum c (green) in GdIG calculated obtained from calculation. b) Total angular momentum $L_{\mathrm{tot}} = |L_{d,Fe} - L_{a,Fe} - L_{c,Gd}|$ in an external magnetic field $\mu_0 H_0$. A black line indicates the angular momentum compensation temperature at $T_{\mathrm{comp,\,L}} = 295\,\mathrm{K}$. c) Effective g value in GdIG obtained using the sublattice magnetization calculated in Sect. 3.1. g_{eff} goes to 0 at $T_{\mathrm{comp,\,M}}$ and diverges at $T_{\mathrm{comp,\,L}}$.

3.2 Calculation of the angular momentum L and effective g value

With the sublattice magnetizations calculated as discussed in Sect. 3.1 and the g values ($g_{\mathrm{Fe,\,d}} = 2.0047$, $g_{\mathrm{Fe,\,a}} = 2.003$ and $g_{\mathrm{Gd,\,c}} = 1.994$) given there, we can calculate the angular momentum L_i attributed to each sublattice i using [27]

$$L_i = \frac{M_i}{\gamma_i} \tag{3.11}$$

where $\gamma_i < 0$ is the gyromagnetic ratio of sublattice i obtained as $\gamma = g_i e/2m$ with m and e the electron mass and charge. The resulting L_i as well as the total angular momentum $L_{\mathrm{tot}} = |L_{d,Fe} - L_{a,Fe} - L_{c,Gd}|$ are shown in Fig. 3.2 a) and b). This calculation

yields an angular momentum compensation temperature $T_{\mathrm{comp,\,L}} = 295\,\mathrm{K}$.

Once the magnetization and angular momentum of each sublattice are known, the effective gyromagnetic ratio according to Eq. 1.27 can be calculated, as well as the effective g value $g_{\mathrm{eff}} = 2m\gamma_{\mathrm{eff}}/e$. The resulting g_{eff} is shown in Fig. 3.2 c) as a function of temperature.

We can distinguish the magnetization compensation temperature $T_{\mathrm{comp,\,M}}$ at 291 K, where $g_{\mathrm{eff}} = 0$ and the angular momentum compensation temperature $T_{\mathrm{comp,\,L}}$ at 295 K, where g_{eff} diverges, so that $T_{\mathrm{comp,\,L}}$ and $T_{\mathrm{comp,\,M}}$ are 4 K apart. This temperature difference is small since the difference between the g_i is small as well.

3.3 Ferromagnetic resonance field

As discussed in Sect. 1.1.1 and 1.1.2, the ferromagnetic resonance frequency ω depends on an effective field $\mu_0 H_{\mathrm{eff}}$, which consists of the static external magnetic field, the shape anisotropy and crystalline anisotropy fields. The total free energy of a magnetic sample in an external magnetic field is given by Eq. (1.5). The contributions to the free energy have different angle dependencies [28], leading to hard and easy magnetic axes. Minimizing the magnetic free energy with respect to the magnetization direction yields the equilibrium orientation of the magnetization, which in general will not be along the external field. We therefore have to distinguish the angles Θ and Φ for the magnetization orientation and θ and ϕ for the external magnetic field, as shown in Fig. 3.3.

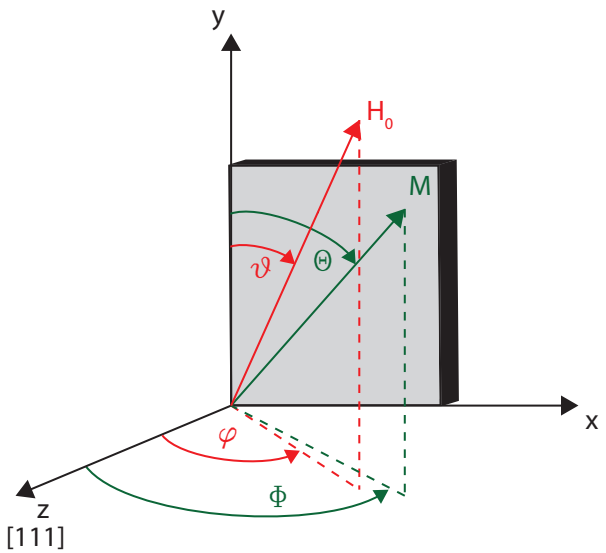

Figure 3.3: Polar coordinate system in a thin film sample: the angles θ and ϕ describe the orientation of the magnetic field $\mathbf{H}_0$, while the angles Θ and Φ describe the magnetization direction. Figure taken from Ref. [28]

For given magnetic field angles θ and ϕ, the energetically favorable magnetization orientation, i.e. Θ_0 and Φ_0, is obtained by minimizing the total free energy in Eq. 1.5.

$$\partial_\Phi F_{\text{tot}}\Big|_{\Phi=\Phi_0} = \partial_\Theta F_{\text{tot}}\Big|_{\Theta=\Theta_0} = 0 \tag{3.12}$$

The resonance condition is given as [27]

$$\left(\frac{\omega}{\gamma}\right)^2 = \frac{1}{M_s^2 \sin^2\Theta}\left(\left(\partial_\Phi^2 F_{\text{tot}}(\Theta_0,\Phi_0)\right)\left(\partial_\Theta^2 F_{\text{tot}}(\Theta_0,\Phi_0)\right) - \left(\partial_\Phi\partial_\Theta F_{\text{tot}}(\Theta_0,\Phi_0)\right)^2\right) \tag{3.13}$$

We use this kind of calculations in two different ways in the course of this thesis: in Sect. 4.2.1.1, we conduct out of plane magnetic field rotations as a function of temperature for the YIG/Pt sample and determine the FMR field as a function of magnetic field orientation. In the case of our thin film samples, the contribution from shape anisotropy and uniaxial crystalline anisotropy both have the same angle dependence and cannot be distinguished in magnetic field orientation dependent FMR experiments. In the simulation we therefore have a uniaxial anisotropy field B_u containing both uniaxial anisotropy terms and a cubic anisotropy field B_c. Since the shape anisotropy dominates in thin films, we can in many samples neglect the crystalline anisotropies B_c. In the simple case of an in plane magnetic field and neglecting B_c the resonance condition can then be written as [28]

$$\left(\frac{\omega}{\gamma}\right)^2 = \left(\mu_0 H_{\text{res,ip}} + B_u\right)\left(\mu_0 H_{\text{res,ip}}\right) \tag{3.14}$$

and for the out of plane configuration we obtain [28]

$$\left(\frac{\omega}{\gamma}\right)^2 = \left(\mu_0 H_{\text{res,oop}} + B_u\right)^2 \tag{3.15}$$

Knowing the resonance frequency and setting the g value to $g = 2$, we then determine the uniaxial anisotropy field B_u necessary to obtain the FMR field observed experimentally in the out of plane magnetic field rotations[3]. B_u can then be compared to the shape anisotropy expected from the magnetization obtained from SQUID magnetometry.

In Sect. 4.2.2 and 4.2.3 however, where the magnetically compensated materials are discussed, we start from the very general formula (3.13): the magnetization is obtained from the mean field calculation described in Sect. 3.1 and for γ we can insert the effective gyromagnetic ratio from Sect. 3.2. Equation (3.13) then allows for the calculation of

[3]This specific part of the simulation for out of plane magnetic field rotations was written by Dr. M. Althammer at WMI.

the resonance frequency ω for given anisotropies, external magnetic field strength and orientation. In our experiments however, a fixed microwave frequency $\omega_c = 2\pi\ 9.7\,\mathrm{GHz}$ is used and we want to calculate the corresponding resonance field. The simulation varies the external magnetic field until $\omega = \omega_c$, and gives out the corresponding value $\mu_0 H_{\mathrm{res}}$. For all calculations we use $\phi = 90°$, so that the magnetic field is always applied in the sample plane and the angle θ then corresponds to the in plane angle. Since in [111] oriented films, the orientation of the 100, 010 and 001 axes is not known, θ is not precisely known from the measurement configuration. The remaining free parameters θ and the anisotropy constants are then chosen in order to best match the experimental data of the FMR field.

Chapter 4

Spin pumping and microwave induced spin Seebeck effect in YIG/Pt, InYGdIG/Pt and GdIG/Pt bilayers

In this chapter, we will discuss the temperature dependence of the spin pumping and spin Seebeck effect in magnetically compensated systems. We will start by describing the measurement setup used for these experiments and then proceed to the analysis of the experimental results. The first sample discussed is a YIG/Pt bilayer, which does not exhibit compensation and is therefore used as a reference sample. We will then give a detailed analysis of the measurements in the InYGdIG/Pt sample and finally of the pure GdIG/Pt sample for comparison.

4.1 Experimental setup

4.1.1 Ferromagnetic resonance

The measurement setup used in this thesis is similar to the one used by Franz Czeschka in his PhD thesis [35] and a sketch of the setup we use is depicted in Fig. 4.1 a). For ferromagnetic resonance (FMR) experiments each sample is mounted on a glass tube (Fig. 4.1 c)), which is non magnetic, and inserted in a Bruker 4118X-MD5 microwave cavity with a resonance frequency of $\omega_C/(2\pi) = 9.7\,\mathrm{GHz}$. The external magnetic field $-0.8\,\mathrm{T} \leq \mu_0 H_0 \leq +0.8\,\mathrm{T}$ is applied in the thin film plane, along the short side of the sample. An Agilent E8257D microwave source is used to generate the microwave radiation. The microwave power is split, so that one part of the beam passes the circulator and reaches the resonator, with a power kept constant at 18 dBm throughout all experiments. The split off signal is used as reference for homodyne detection. The reflected microwave from the sample as well as the reference signal are fed into an IQ mixer (Marki IQ0618LXP) and the I and Q output signals obtained this way are shifted in phase by 90°. The phase between the reference signal and the signal from the cavity can be adjusted using a phase shifter, so that the I output signal is purely absorptive (Lorentzian shaped), and Q is

purely dispersive (Lorentzian derivative), or vice versa.

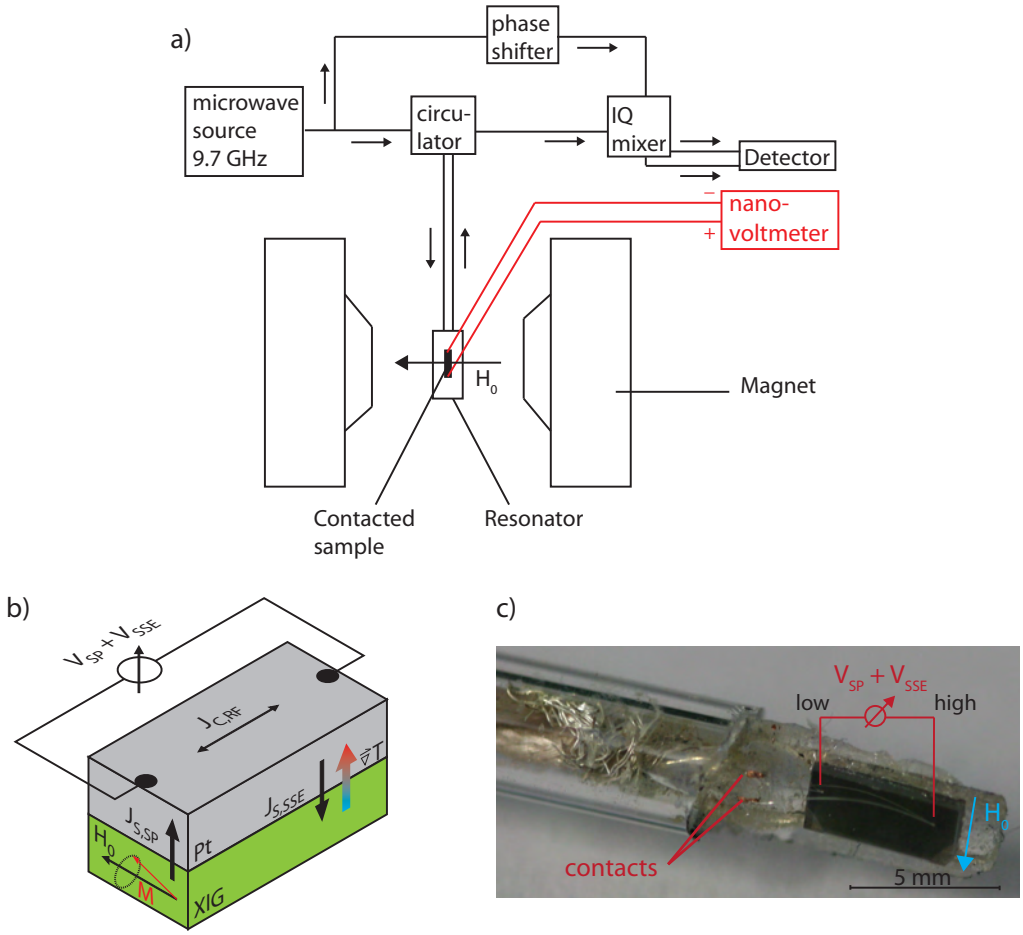

Figure 4.1: a) Sketch of the measurement setup for FMR and dc voltage detection with two magnet coils, microwave source, circulator, cavity with sample inside, IQ mixer and phase shifter for homodyne detection as well as nanovoltmeter to measure the dc voltage. b) Measurement configuration: the external magnetic field H_0 is applied in the thin film plane along the short side of the sample, the dc voltage V_{DC} is measured along the long side so that the maximum spin pumping V_{SP} and spin Seebeck voltage V_{SSE} can be detected. c) Photograph of the InYGdIG/Pt sample mounted on a glass tube and bonded onto the Cu inner conductors of two coaxial cables.

4.1.2 Spin pumping and microwave induced spin Seebeck effect

For the spin pumping and the spin Seebeck effect experiments one and the same setup as described in Sect. 4.1.1 and Fig. 4.1 a) is used, so that FMR by microwave absorption and V_{DC} can be measured simultaneously. As discussed previously in Sect. 1.2.1, the spin currents produced by spin pumping and SSE are converted into a dc charge current via

the inverse spin Hall effect. The sample configuration is shown in Fig. 4.1 b): the voltage is measured along the long side of the sample and the external magnetic field is applied along the short side. In this orientation, the absolute spin pumping and spin Seebeck voltages reach their maximum amplitude (see Sect. 1.2.2 and 1.2.3).

Fig. 4.1 c) shows a photograph of the InYGdIG sample mounted on a glass tube and bonded onto the inner conductors of two coaxial cables. The dc voltage is then measured using a Keithley 2182 nanovoltmeter. The blue arrow in 4.1 c) points in the direction of the external positive magnetic field, i.e. the direction in which a compass needle points (geographic earth north pole) [36]. This corresponds to a magnetic field orientation of $\alpha = 180°$ in Fig. 1.1 and we therefore expect a negative SSE voltage and positive spin pumping amplitude for positive magnetic fields in YIG/Pt (see Sect. 1.2.2 and 1.2.3).

4.1.3 Temperature dependent measurements

For temperature dependent measurements the resonator is inserted into an Oxford CF935 continuous flow cryostat which can be operated with liquid nitrogen or liquid helium. There is no internal reservoir for cryogenics, so cold gas or liquid needs to be supplied by an insulated transfer tube. The cold gas flows into the cryostat past a heater and temperature sensor beneath the sample and through the sample space. The system can be operated using a pump at the cryostat output to create an under-pressure and pull gas through. This pumping can lead to pressure fluctuations that are visible in sensitive measurements. Pressure fluctuations can be avoided by using overpressure at the cryostat entrance to promote gas flow. This method yields a much better signal to noise ratio and is therefore preferentially used.

4.1.4 Temperature measurement and calibration

The relevant temperature in spin pumping and SSE experiments, especially in magnetically compensated materials, is the temperature of the ferrimagnetic film T_{FM}. Additionally in SSE experiments, the amplitude of the effect depends on the difference between the magnon temperature in the ferrimagnetic film and the electron temperature in the Pt film [18] (see Sect. 1.2.2), so that in addition to T_{FM} also the Pt temperature T_{Pt} is important. However, the difference between T_{FM} and T_{Pt} is of the order of 1 K at the most in this kind of bilayers [43] and both are thus in this discussion treated as the same temperature $T_{\mathrm{sample}} = T_{\mathrm{FM}} \approx T_{\mathrm{Pt}}$.

Since the sample is locally heated by an ac current induced by the rf electric field, T_{sample} is not necessarily the same as the temperature T_{cryo} measured at the cryostat temperature sensor, which is located beneath the sample and measures the temperature of the gas flowing into sample space in our setup. There are different methods to experimentally determine a possible temperature difference $\Delta T = T_{\mathrm{cryo}} - T_{\mathrm{sample}}$, and we will discuss two of them in this section.

The microwave heating in the GdIG/Pt sample can be determined by measuring the temperature dependent Pt resistance, while the microwave radiation is switched on, and comparing it to the resistance when the microwave is switched off. The temperature can then be calculated from

$$\rho(T_{\mathrm{Pt}}) = \rho_0 \left(1 + \alpha(T_{\mathrm{Pt}} - T_{0,\,\mathrm{Pt}})\right) \tag{4.1}$$

with $\alpha = 3.92 \times 10^{-3}\mathrm{K}^{-1}$ the temperature coefficient for bulk Pt [81], $T_{0,\,\mathrm{Pt}} = T_{\mathrm{cryo}}$ and ρ_0 the Pt temperature and resistance without microwave heating, and $T_{\mathrm{Pt}} = T_{\mathrm{sample}}$ the temperature obtained with the microwave radiation switched on. Since the coefficient α in thin films can be reduced by up to a factor of 3 as compared to bulk Pt (see Ref. citeSibylle and Sect. 4.2.1.2) the values obtained for $\Delta T = T_{\mathrm{Pt}} - T_{0,\,\mathrm{Pt}}$ with Eq. (4.1) should be understood as lower bounds.

In the GdIG/Pt sample we found $\Delta T = 5\,\mathrm{K}$ for a microwave power of 18 dBm while the cryostat was at room temperature and no gas was flowing through the sample space.

The resistive thermometry did not always lead to reproducible results because two measurements under similar conditions yielded different resistances. This was probably due to slow thermalization processes of the resonator and sample, leading to a temperature drift during the experiments.

As mentioned before in Sect. 2.1, for the GdIG/Pt sample, measurements above room temperature are necessary in order to probe the whole relevant temperature region around T_{comp}. The cryostat is not laid out for temperatures above 300 K, therefore the sample itself must be heated. A heating of the sample further than the heating already attained by microwave radiation can be achieved by applying a dc current of 1 to 10 mA to the Pt layer using a Keithley 2400 sourcemeter, which corresponds to Joule heating of up to 22.8 mW in this sample. Using Eq. (4.1), we determined the sample temperature attained by microwave heating at a power of 18 dBm and dc Joule heating at a power of 22.8 mW to be about 303 K. This is still within the divergence region for GdIG, but using higher currents and heating power increases the risk of damaging the sample, while the increase in temperature is still too small to heat the sample well above T_{comp}. Therefore dc current heating was not pursued, especially since in samples like InYGdIG measurements well below and well above T_{comp} are straightforwardly possible using the standard cryostat temperature range.

In addition to resistive thermometry, we can make use of the fact, that near the compensation point, the compensated material reacts very sensitively to small temperature changes (e.g. divergence of the coercive field at $T_{\mathrm{comp,\,M}}$ as described in Sect. 4.2.2.2). This method is based on properties of the magnetically compensated system and will therefore allow us to determine T_{FM}. We find the additional heating to be about 18 K in the InYGdIG/Pt sample at a cryostat temperature of 77 K and with a microwave power of

18 dBm, so that $T_{\mathrm{FM}} = T_{\mathrm{cryo}} + 18\,\mathrm{K}$. The exact method leading to this result is described in Appendix A.

The microwave heating of $\Delta T = 18\,\mathrm{K}$ in InYGdIG/Pt determined at $T_{\mathrm{cryo}} = 18\,\mathrm{K}$ as detailed in Appendix A is different from the $\Delta T = 5\,\mathrm{K}$ determined at room temperature in the GdIG/Pt film. This is probably due to the fact, that the thermalization efficiency depends sensitively on the environment, viz. cryostat temperature, gas flow, etc. While the InYGdIG/Pt sample was held at a stable temperature of 70 K by a steady Helium gas flow, the resistance measurements in GdIG/Pt were conducted without gas flow, so that the sample temperature in this case might not have been as stable. Furthermore, we have seen that Eq. (4.1) gives only a lower bound of the temperature increase, while the actual heating could be higher. In addition to this, the Pt film quality might also play a role in the amount of heating induced by the rf current in different samples.

This discussion shows the different issues concerning precise temperature calibration in our setup. Since the Joule heating may vary for different samples (film quality) and different cryostat conditions (viz. cryostat temperature, gas flow), a universal correction of the temperature scale by a constant factor might distort the results. A precise calibration would require resistance measurements in each sample over the whole temperature range with and without microwave radiation. Since the extent of the calibration issues became clear only after comparing measurements in different samples, no such calibration was possible within the time frame of this thesis. We will therefore initially always use the temperature T_{cryo} that was actually measured and discuss a temperature correction afterwards if necessary.

4.2 Experimental results

In the following section, the results of temperature dependent ferromagnetic resonance, spin pumping and spin Seebeck effect measurements in our three different samples YIG/Pt, GdIG/Pt and InYGdIG/Pt are presented.

4.2.1 Temperature dependent FMR, spin pumping and spin Seebeck effect measurements in YIG/Pt

We first turn to the analysis of ferromagnetic resonance, spin pumping and spin Seebeck effect measurements as a function of temperature in our YIG/Pt reference sample. In order to analyze the following experiments in compensated garnets, a reference measurement using a well known ferrimagnetic system, e.g. YIG, is useful. This will allow us to distinguish effects inherent to compensated systems from those which can also be seen in materials with a Brillouin like magnetization curve.

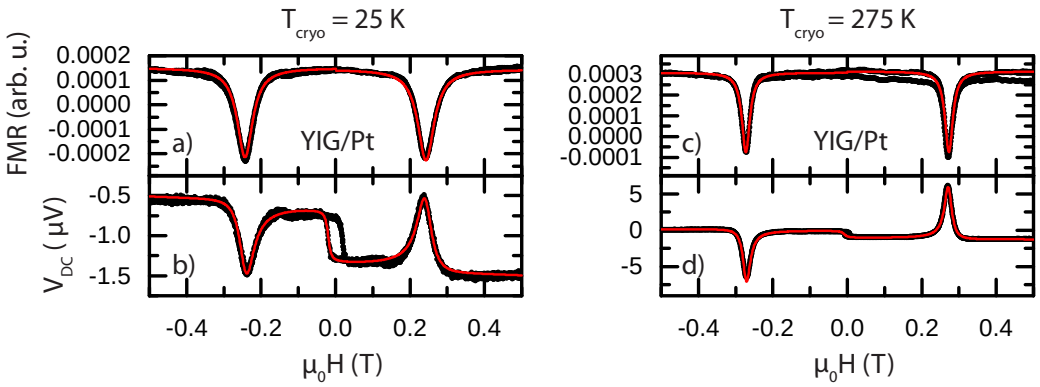

Figure 4.2: Ferromagnetic resonance of the YIG/Pt sample at $T_{\mathrm{cryo}} = 25\,\mathrm{K}$ (a) and $T_{\mathrm{cryo}} = 275\,\mathrm{K}$ (c), dc voltage as a function of external magnetic field at $T_{\mathrm{cryo}} = 25\,\mathrm{K}$ (b) and $T_{\mathrm{cryo}} = 275\,\mathrm{K}$ (d). The voltage signal is a superposition of the SSE hysteresis and the two spin pumping Lorentzian peaks at the FMR resonance position. The black dots represent experimental data, the red line is the fit.

Even though temperature dependent SSE and spin pumping measurements have previously been conducted in YIG thin films [9, 10, 16, 17, 38, 41, 43, 70], and a report of simultaneous measurements of both effects has been put forward recently [82], there are, to our knowledge, no such measurements as a function of temperature.

The ferromagnetic resonance, spin pumping and spin Seebeck effect were measured from $T_{\mathrm{cryo}} = 5\,\mathrm{K}$ - $295\,\mathrm{K}$ in $10\,\mathrm{K}$ steps using liquid He. The external magnetic field was applied in the film plane as described in Fig. 4.1 c) and swept from $0.5\,\mathrm{T}$ down to $-0.5\,\mathrm{T}$ and up again in order to observe the full hysteretic magnetization behaviour of the ferrimagnetic sample.

4.2.1.1 Ferromagnetic resonance

We will start by analyzing the ferromagnetic resonance detected by microwave absorption, which is depicted in Fig. 4.2 a) and c) for $T_{\mathrm{cryo}} = 25\,\mathrm{K}$ and $T_{\mathrm{cryo}} = 275\,\mathrm{K}$ respectively.

The absorption curve (black dots), i.e. the absorption signal coming from the IQ mixer (see Fig. 4.1 a)), has a Lorentzian shape (see Sect. 1.1.1) and the experimental data is fitted using Eq. (1.4) (red line in Fig. 4.2 a) and c)). In both cases the up and down magnetic field sweeps are depicted, but for visibility reasons only the peaks from one sweep direction are fitted. In Fig. 4.2 c) the problem of temperature drifting becomes clear, since up and down sweep do not coincide exactly. This is due to the fact that when the cavity temperature drifts only slightly, its resonance frequency ω_{C} changes as well. In a FMR experiment, we measure the reflected signal from the cavity at a fixed frequency ω. Therefore, if ω_{C} drifts away, $\omega \neq \omega_{\mathrm{C}}$ and the reflected microwave power changes, leading to the kind of drift visible in Fig. 4.2 c). This also leads to small

distortions of the Lorentzian absorption curves of the sample, which are more or less pronounced depending on thermalization efficiency and temperature stability throughout the measurement, especially for broad FMR lines. Additionally, since most of the signal is absorbed in the cavity, the reflected signal is small and more affected by statistical noise. It is therefore difficult to determine the experimental errors in the FMR data, and for this reason no error bars are given.

We will see in Sect. 4.2.1.2, that the absorption line can be analyzed with more precision in the dc voltage, but the FMR measurement still is a good enough method to determine the position and linewidth of the resonance.

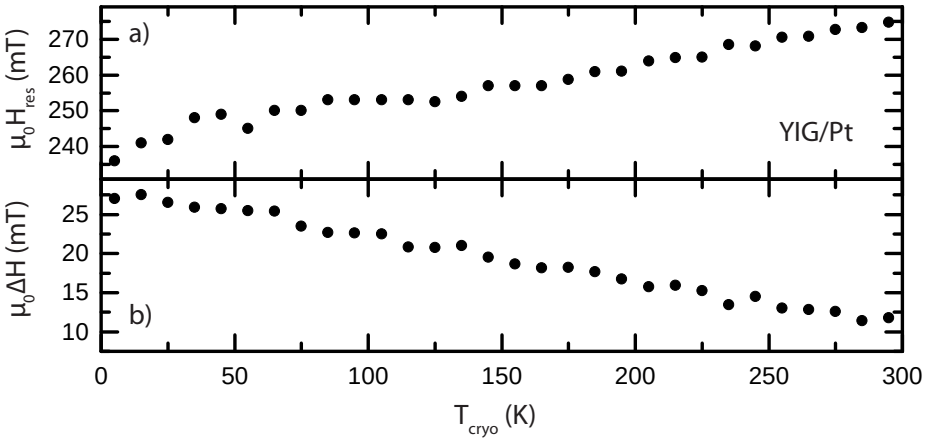

Figure 4.3: a) In plane ferromagnetic resonance field $\mu_0 H_{\mathrm{res}}$ and b) half FMR linewidth in the YIG/Pt sample as a function of the cryostat temperature T_{cryo}.

We will first discuss $\mu_0 H_{\mathrm{res}}$ extracted from in plane FMR measurements for different temperatures, as summarized in Fig. 4.3 a). $\mu_0 H_{\mathrm{res}}$ decreases with temperature from 275 mT at T_{cryo}= 295 K to 235 mT at T_{cryo}= 5 K.

This decrease in resonance field at low temperatures has been observed previously in YIG [61, 71] and in Fe or Co thin films [15, 83, 84]. It is attributed to an increase of the saturation magnetization [61, 85, 86] and/or anisotropy [77, 84] with decreasing temperature.

The influence of different kinds of anisotropy on the resonance field has been discussed in Sect. 1.1.2 and 3.3. Since in thin films the shape anisotropy $\mu_0 M_{\mathrm{sat}}$ is an important contribution to the effective field, we will first determine the temperature dependence of the saturation magnetization separately. A SQUID magnetometry measurement of the YIG/Pt thin film is shown in Fig. 4.4. M_{sat} increases from 99 kA/m at T_{sample}= 295 K to 151 kA/m at T_{sample} = 10 K [1] which is comparable to previous measurements [61, 85, 86].

[1] In the SQUID setup the temperature measured is assumed to be T_{sample} since there is no additional

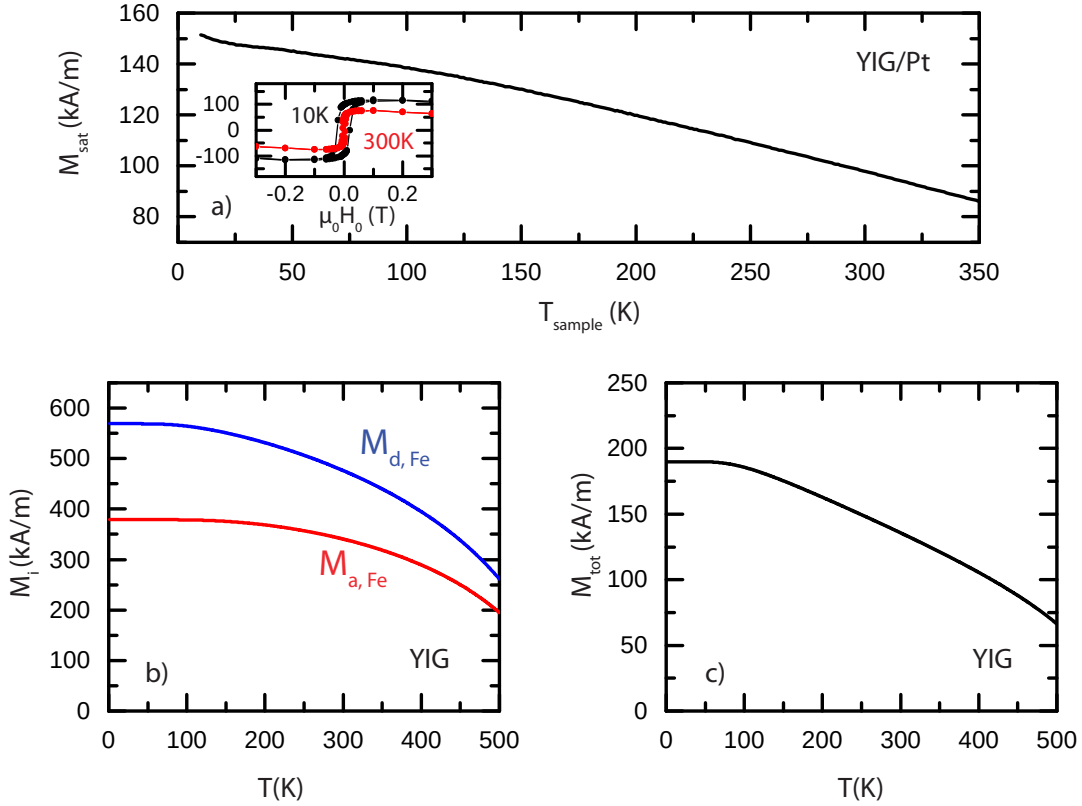

Figure 4.4: Saturation magnetization as a function of sample temperature of the YIG/Pt thin film. The inset shows the saturation magnetization as a function of external field at T_{sample}= 10 K (black) and T_{sample}= 300 K (red).

The sublattice magnetizations as well as the total magnetization can also be calculated as described in Sect. 3.1 and the results are shown in Fig. 4.4 b) and c). The calculation yields qualitatively the same behaviour of the magnetization as the SQUID magnetometry. However, the obtained values are not the same since at $T_{\text{sample}} = 300\,\text{K}$ from the experiment we find $M_{\text{sat}} = 97\,\text{kA m}^{-1}$, while the calculation yields $M_{\text{sat}} = 135\,\text{kA m}^{-1}$. The value from the calculation is consistent with the bulk value in YIG [62], while the experimentally determined magnetization is lower. This difference might be due to an inferior sample quality in our thin film, but also to errors in the experimental determination of the magnetization.

In order to give an estimation of the error arising when determining the saturation magnetization, we will quickly describe how the magnetization is obtained. The SQUID magnetometry measures the magnetic moment of the whole sample. Since the substrate is orders of magnitude thicker ($t_{\text{substrate}} = 500\,\mu\text{m}$) than the magnetic thin film, its diamag-

heating.

netic contribution cannot be neglected and has to be subtracted from the total moment. Then, in order to calculate the sample magnetization $M = m/V$ from the magnetic moment m determined from SQUID magnetometry, the volume V of the ferrimagnetic thin film has to be determined. This is achieved by measuring the sample area and multiplying it with the ferrimagnetic film thickness from XRD measurements. This can give rise to errors if the film is not completely homogeneous. This procedure yields different small sources of errors (ferrimagnet volume, subtraction of diamagnetic moment) which eventually can lead to a deviation from the actual magnetization.

According to Eq. (1.7) the increase of M_{sat} with decreasing T leads to an increase of the shape anisotropy term and therefore to a decrease of the resonance field (see Eq. (3.14)) with temperature, which is consistent with the experimental results for $\mu_0 H_{\mathrm{res}}$.

In addition to shape anisotropy, there might also be other contributions from the crystal. In a more general way, the anisotropy terms can be determined by measuring the evolution of the FMR resonance field as a function of the external magnetic field orientation and analyzing this FMR angle dependence in terms of different magnetic anisotropy contributions [28]. This can be done by using the simulation presented in Sect. 3.3 based on the free energy considerations in Sect. 1.1.2, where the uniaxial (B_u) and the crystalline cubic (B_c) anisotropy fields can be adjusted so that the resulting resonance field matches the experimental results.

We recorded FMR as a function of magnetic field orientation, rotating around the axis along the long side of the sample, so that for 0° orientation the external field is in plane and for 90° it is out of plane. These measurements were performed at five different temperatures in the cryostat and the resonance fields are shown in Fig. 4.5 a). In Fig. 4.5, all data is shown as a function of the sample temperature $T_{\mathrm{sample}} = T_{\mathrm{cryo}} + 18\,\mathrm{K}$ (see Sect. 4.1.4), in order to compare it with the SQUID magnetometry data.

Fig. 4.5 b) shows the comparison of experimental FMR data (green dots) and our simulation (red line) for $T_{\mathrm{sample}} = 168\,\mathrm{K}$. This was done for all five temperatures in order to extract B_u and B_c.

The uniaxial anisotropy term B_u is plotted as a function of temperature in Fig. 4.5 c) (black dots). This term contains the shape anisotropy, corresponding to $\mu_0 M_{\mathrm{sat}}$, and the crystalline uniaxial anisotropy. $\mu_0 M_{\mathrm{sat}}$ derived from SQUID magnetometry as seen in Fig. 4.4 was also plotted as red dots in Fig. 4.5 c) and deviates from the B_u extracted from simulation. This difference could represent the additional crystalline uniaxial anisotropy, but is probably mainly due to errors in the determination of $\mu_0 M_{\mathrm{sat}}$. Therefore a comparison of B_u and $\mu_0 M_{\mathrm{sat}}$ will not allow us to determine the additional crystalline uniaxial anisotropy with certainty. Still, it is clear that the total uniaxial anisotropy increases with decreasing temperature, explaining the behaviour of H_{res} and confirming previous measurements [61].

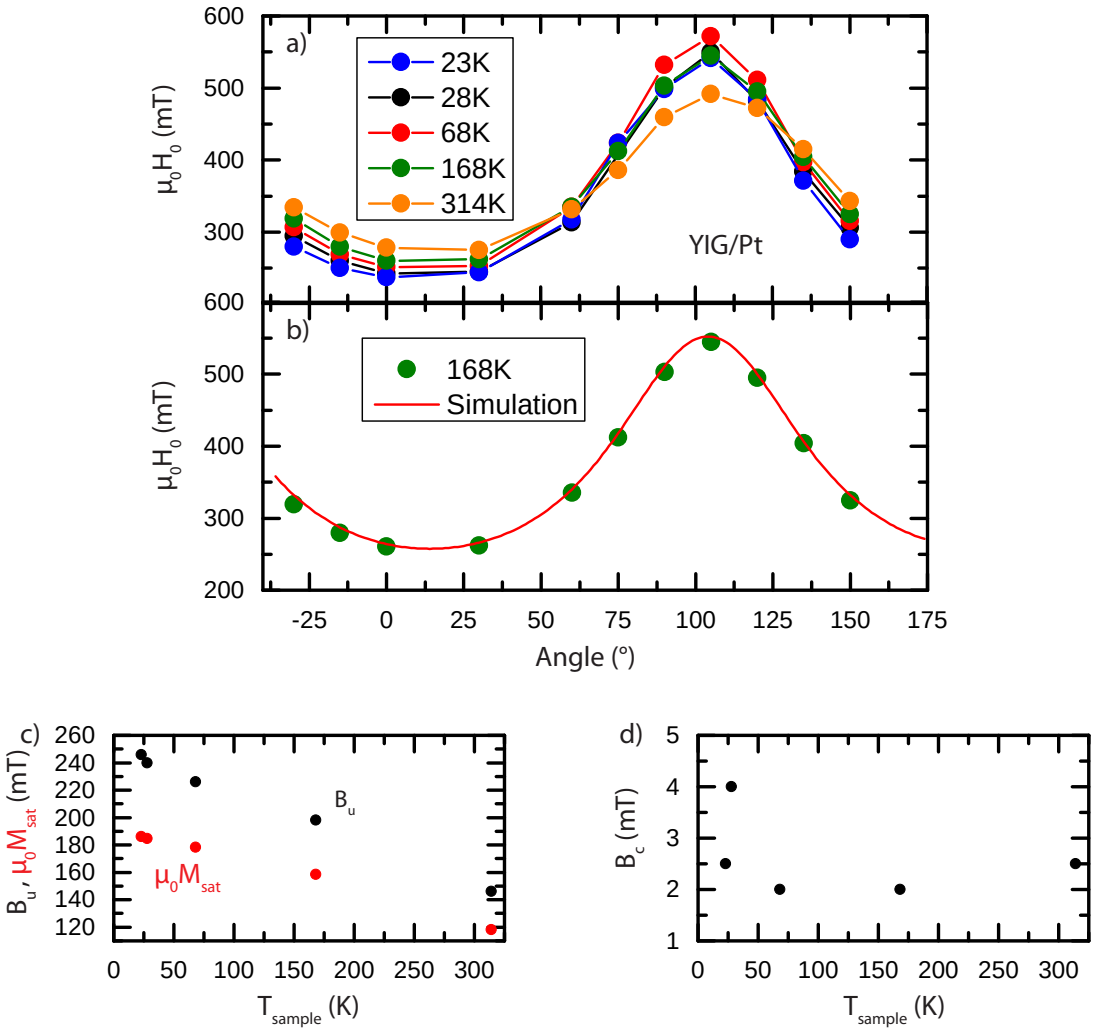

Figure 4.5: a) Magnetic field orientation dependence of the ferromagnetic resonance field in YIG/Pt as a function of T_{sample}. b) Comparison of the experimental FMR resonance field data in YIG/Pt at $T_{\text{sample}} = 168\,\text{K}$ (green dots) with simulation data (red line). c) Uniaxial anisotropy term B_u (black dots) and saturation magnetization (red dots) as a function of T_{sample}, as extracted from simulation parameters. d) Cubic crystalline anisotropy term B_c as a function of T_{sample} extracted from simulation as well.

The cubic anisotropy was also extracted from the FMR simulation (see Fig. 4.5 d)) but is negligible compared to the uniaxial term and does not exhibit a clear temperature dependence.

The temperature dependence of the ferromagnetic resonance field shown in Fig. 4.3 can therefore be explained mainly by an increase of the uniaxial anisotropy, which is dominated by shape anisotropy.

After analyzing the FMR resonance position, we also look at the FMR hlaf linewidth, which was extracted from the fit to the FMR as well and is shown in Fig. 4.3 b): the linewidth increases with decreasing temperature from 10 mT at T_{cryo}= 295 K to 25 mT at T_{cryo}= 5 K. The increase of linewidth at low temperatures has also been observed previously in YIG [61] and in ferromagnetic metals [15]. The monotonous increase of linewidth with decreasing temperature in Fe thin films is attributed to an increase of anisotropy at low temperatures [83]. This is consistent with the angle dependent measurements described above (Fig. 4.5 c)). However, further analysis of the linewidth and damping might be necessary to fully explain the FMR temperature dependence.

4.2.1.2 DC voltage

Simultaneously to the ferromagnetic resonance measurements by microwave absorption, the dc voltage along the sample long side was recorded as a function of temperature. Two such measurements are shown in Fig. 4.2 b) and d) for T_{cryo}= 25 K and T_{cryo}= 275 K, where the experimental data is represented by black dots. The dc voltage can be understood as a superposition of the resonant spin pumping and microwave rectification voltage and the non resonant, microwave heating induced, spin Seebeck voltage. In the configuration shown in Fig. 4.1, at room temperature, the spin pumping voltage is positive and the SSE voltage negative at positive magnetic field. This is consistent with the absolute sign of both effects as determined by Schreier et al. [36] (see Sect. 1.2.2 and 1.2.3) . We use Eq. (1.26) to fit the experimental data, as indicated by the red line in Fig. 4.2 b) and d).

The fit reproduces well the experimental data in terms of spin Seebeck hysteresis and resonant voltage.

The parameters we can extract from fitting Eq. (1.26) to our data are: the peak position, corresponding to the FMR resonance field $\mu_0 H_{\mathrm{res}}$, the half width at half maximum $\mu_0 \Delta H$, the amplitudes of the spin pumping and rectification voltage (L and D respectively), the amplitude $2B$ of the SSE voltage and the coercive field $\mu_0 H_{\mathrm{c}}$ of the ferrimagnetic layer.

4.2.1.3 Spin pumping

We first focus on the analysis of the spin pumping signal. As discussed in Sect. 1.2.3, spin pumping measurements allow the electrical detection of ferromagnetic resonance. Therefore the resonance position of both spin pumping signal and FMR should coincide. This can be seen qualitatively when comparing Fig. 4.2 a) and b) as well as c) and d). It is also clearly visible in Fig. 4.6 a) where $\mu_0 H_{\mathrm{res}}$ extracted from the FMR (using Eq. (1.4)) is represented by black dots and $\mu_0 H_{\mathrm{res}}$ extracted from spin pumping (using Eq. (1.26)) is shown as red dots. The results from FMR and spin pumping are in good agreement, except for small deviations at some temperatures. These deviations are due to the different detection methods: while in spin pumping measurements a large signal is detected with a rather small noise level, the FMR measurements are more affected by noise and especially

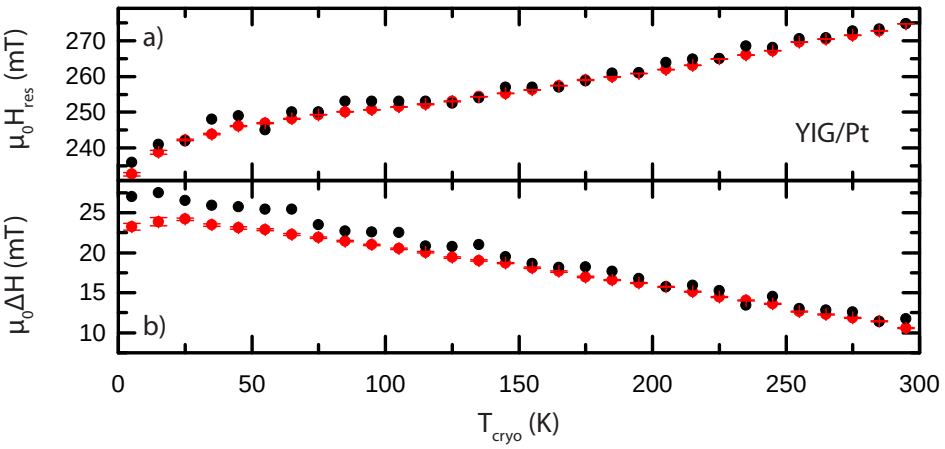

Figure 4.6: Resonance position (a) and half width at half maximum (b) from FMR (black dots) and spin pumping (red dots) in YIG/Pt for an in plane external magnetic field.

by temperature drift of the cavity, as discussed in Sect. 4.2.1.1.

The half width at half maximum was also extracted from the dc voltage using expression (1.26). These values are plotted as red dots in Fig. 4.6 b). The black dots representing the previously measured values from the FMR, match the results from spin pumping well between 150 K and 295 K. Below this, the values deviate which can again be attributed to the temperature drift affecting the FMR measurements and leading to a distortion of the FMR line (see Sect. 4.2.1.1).

Overall, the FMR and spin pumping measurements are consistent, yielding very similar results concerning resonance field and linewidth. Since the data quality of the spin pumping voltage is superior to the FMR data quality, we will from now on concentrate on the dc voltage and use the FMR measurements only for comparison.

After comparing the resonance fields and linewidths extracted by FMR and spin pumping measurements, we will turn to the spin pumping amplitude, i.e. the amplitude L of the symmetric part in Eq. (1.26), which is shown in Fig. 4.7 a). L increases by a factor of about 15 from $T_{\mathrm{cryo}} = 5\,\mathrm{K}$ to room temperature. The amplitude of the antisymmetric part D, attributed to microwave rectification, is also plotted as a function of temperature in Fig. 4.7 b). D increases as well with temperature, by a factor of about 6 over the whole temperature range. L and D have opposite signs, but the symmetric part is an order of magnitude larger than the antisymmetric part and therefore dominates the voltage in resonance.

We now turn to a quantitative analysis of the spin pumping amplitude. As described in

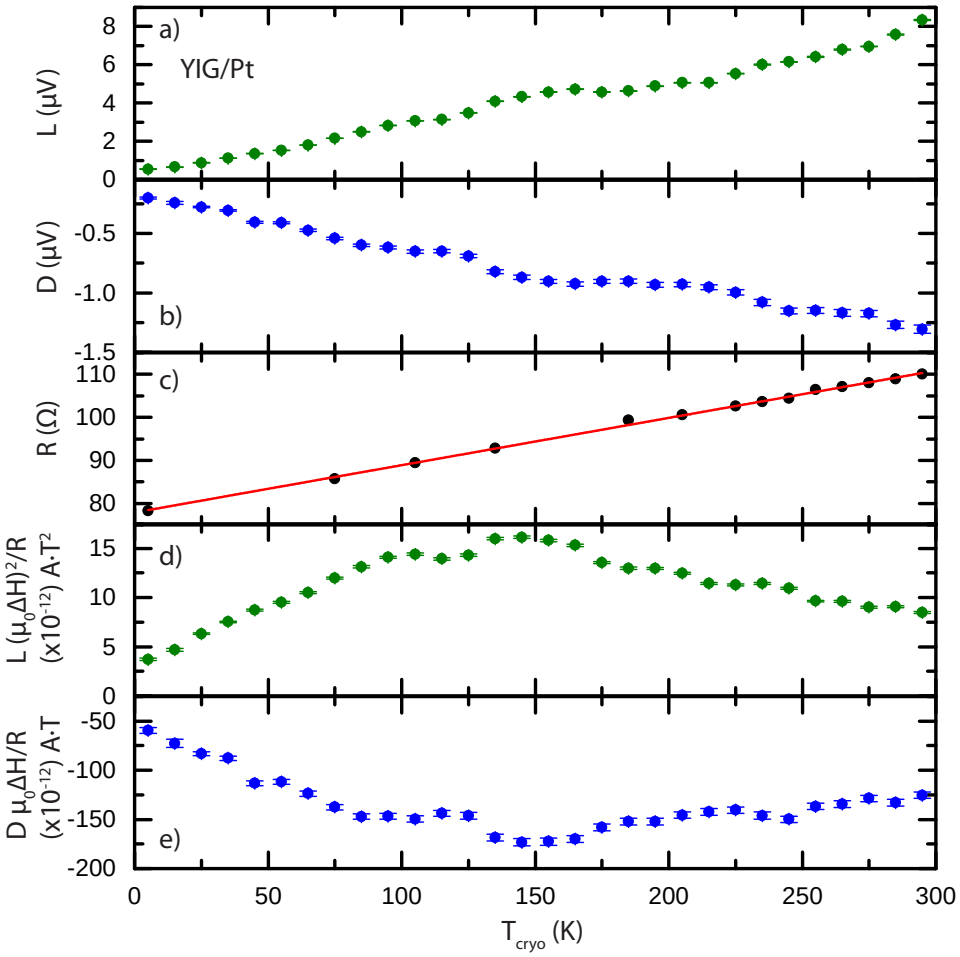

Figure 4.7: a) Spin pumping amplitude L (green dots) and b) microwave rectification amplitude D (blue dots) of the YIG/Pt sample as a function of temperature. L and D have opposite signs but their absolute value increases with temperature. The resonant voltage signal is dominated by spin pumping which is one order of magnitude larger than the rectification amplitude. c) The resistance (black dots) of the YIG/Pt sample also increases with temperature and can be fitted linearly (red line). d) The effective spin pumping signal $L \cdot \Delta H^2/R$ as well as the effective rectification amplitude $D \cdot \Delta H/R$ (e) have a broad maximum around 150 K.

Eq. (1.15) and (1.18), the spin pumping amplitude L is proportional to $\frac{1}{\Delta H^2}$, such that $L \cdot (\mu_0 \Delta H)^2$ represents a spin pumping "efficiency".

Since the spin pumping voltage is also proportional to the sample resistance (see Eq. (1.15)), i.e. the temperature dependent Pt resistance, an IV-curve was recorded for some temperatures. The IV-curve was linear for currents from 1 µA to 1 mA and the resistance was extracted from a linear fit to this data. The results can be seen in Fig. 4.7 c) as black dots. From this data we can determine the temperature dependence of the Pt resistance using again a linear fit (red line). This leads to $R(T_{\mathrm{cryo}}) = (77.9 \pm 0.3)\,\Omega +$

$(0.11 \pm 0.0013) \cdot T_{\mathrm{cryo}}\ \Omega/\mathrm{K}$. Comparing this to Eq. (4.1) we find a temperature coefficient $\alpha = 0.0014\mathrm{K}^{-1}$ which is lower than the value for bulk Pt $\alpha_{\mathrm{bulk}} = 0.00392\mathrm{K}^{-1}$ [87], but similar to YIG/Pt films with comparable Pt thickness, as discussed in [8].

In order to exclude the temperature dependence of the Pt resistance from the spin pumping voltage, the spin pumping current can be calculated $I_{\mathrm{SP}}(T) = L/R$, which is justified since the ISHE induces a charge current in the Pt layer. From this we can again calculate a spin pumping current efficiency $L \cdot (\mu_0 \Delta H)^2/R$ shown in Fig. 4.7 d). Starting from $3.7 \cdot 10^{-12}\,\mathrm{A\,T^2}$ at T_{cryo}= 5 K, the spin pumping current efficiency increases with T until reaching a maximum of $1.6 \cdot 10^{-11}\,\mathrm{A\,T^2}$ at T_{cryo}= 145 K and then decreases again to $8.4 \cdot 10^{-12}\,\mathrm{A\,T^2}$ at room temperature. This corresponds to a change in signal of a factor of 4 between both extrema. Even though the obtained efficiency value is not constant over the whole temperature range, the change in signal over T is much less than in the spin pumping voltage L.

If we take a look at Eq. (1.15) and the parameters contributing to the spin pumping voltage, by calculating the spin pumping current efficiency, as shown in Fig. 4.7 d), we have excluded the temperature dependence of the resistance and the linewidth (damping). The spin diffusion length λ_{SD}, as well as the spin mixing conductance $g_{\uparrow\downarrow}$ were found to be temperature independent in YIG/Pt thin films, while the spin Hall angle α_{SH} decreases slightly with T [8]. Therefore in $L \cdot (\mu_0 \Delta H)^2/R$ only a small temperature dependence is expected, which is consistent with our results.

A similar analysis for the antisymmetric amplitude D, using $D \cdot \mu_0 \Delta H/R$ as discussed in Sect. 1.3 [46], is shown in Fig. 4.7 e). The obtained value normalized to linewidth and resistance has a similar behaviour as the spin pumping current efficiency $L \cdot (\mu_0 \Delta H)^2/R$, also showing a maximum around 150 K. Since this antisymmetric signal is attributed to microwave rectification based on the spin Hall magnetoresistance, the rectification efficiency $D \cdot \mu_0 \Delta H/R$ is expected to have a similar temperature dependence to the SMR effect. The SMR depends on the same parameters cited above for the spin pumping voltage, viz. λ_{SD}, $g_{\uparrow\downarrow}$ and α_{SH} [8], which explains the similarities in the temperature dependence between $L \cdot (\mu_0 \Delta H)^2/R$ and $D \cdot \mu_0 \Delta H/R$ (see Fig. 4.7 d) and e)).

The results obtained from the resonant voltage signal confirm the expectations for the temperature dependence of spin pumping voltage and microwave rectification due to spin Hall magnetoresistance, in particular the different dependencies on the linewidth (see Sect. 1.2.3 and 1.3) predicted by Azevedo et al. [46]. Our results show, that the temperature dependence of the FMR linewidth cannot be neglected in the analysis of the resonant voltage, and that extracting a spin pumping and rectification efficiency allows us to exclude this linewidth temperature dependence.

4.2.1.4 Microwave heating induced spin Seebeck effect

After analyzing the resonantly induced dc voltage, we will now come to the effects arising from non-resonant microwave heating in the Pt layer. Due to the microwave heating induced spin Seebeck effect, the voltage reproduces the magnetic hysteresis, allowing us to deduce not only the SSE amplitude $2B$ but also the coercive field $\mu_0 H_c$ of the ferrimagnetic thin film. Both parameters were plotted as a function of temperature in Fig. 4.8.

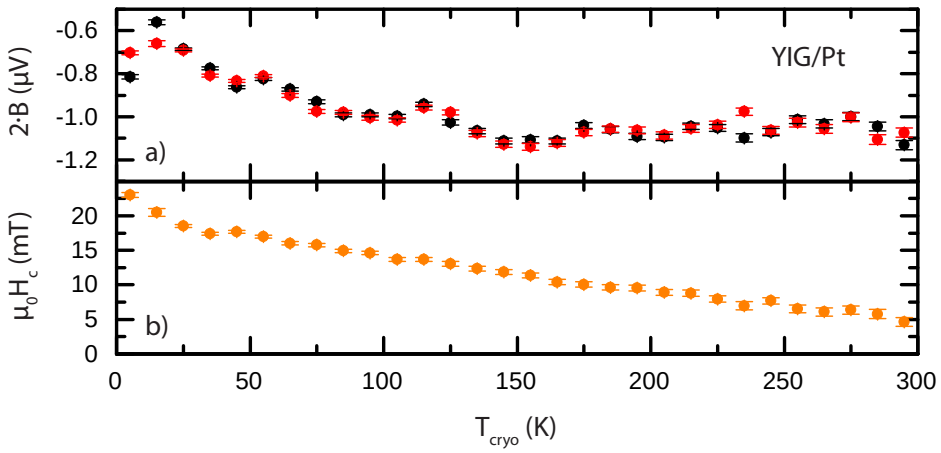

Figure 4.8: a) Temperature dependent spin Seebeck voltage $2B$ in YIG/Pt, extracted using Eq. (1.26). b) Coercive field $\mu_0 H_c$ extracted from spin Seebeck measurements as a function of temperature.

We will begin by analyzing the SSE voltage as shown in Fig. 4.8 a). The SSE voltage is negative, as expected in this configuration [36], and has opposite sign to spin pumping. This is consistent with theory, since in resonance, the magnetization in the ferrimagnetic layer is excited and relaxes by emitting a spin current into the Pt layer (see Fig. 4.1), leading to a positive spin pumping voltage. The spin Seebeck voltage is due to the relaxation of the microwave heated Pt layer into the cooler YIG layer. This yields a spin current in the opposite direction to the spin pumping current, but with same spin polarization, i.e. an ISHE voltage of opposite sign.

We find that the SSE voltage is constant between T_{cryo}= 150 K and room temperature and linearly decreases below 150 K (see Fig. 4.8 a)).

In contrast to spin pumping measurements, the spin Seebeck effect has already been measured as a function of temperature by multiple groups allowing us to compare our results.

Temperature dependent SSE measurements were performed by Uchida et al. [88] in a 1 mm thick YIG sample, covered by 15 nm of Pt, showing a sharp maximum of the SSE voltage signal around 50 K (enhancement by a factor larger than 10 over a temperature range of 70 K) for single crystalline YIG (see black dots in Fig. 4.9 a)). This is attributed

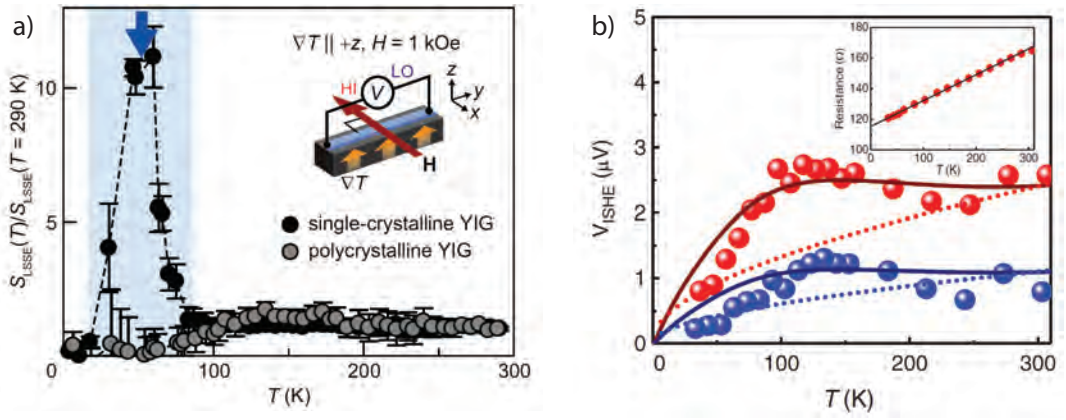

Figure 4.9: a) SSE voltage normalized to the room temperature amplitude measured by Uchida et al. in two YIG(1 mm)/Pt(15 nm) samples as a function of sample temperature. One sample is single-crystalline and shows a large enhancement of the SSE around 50 K while no such increase arises in the polycrystalline YIG/Pt sample [88]. b) Temperature dependent SSE voltage measured by Rezende et al. in a YIG(8 mm)/Pt(6 nm) sample for a temperature difference $\Delta T = T_{\mathrm{Pt}} - T_{\mathrm{YIG}}$ of 3 K (blue dots) and 6 K (red dots) [13]. The solid lines were calculated using the model presented in [13].

to an increased phonon lifetime in single crystalline YIG and so called phonon-drag [89] leading to a strong enhancement of the thermal conductivity. According to Uchida et al., the voltage in polycrystalline YIG/Pt (grey dots in Fig. 4.9 a)) does not show such a strong T dependence.

XRD measurements show that our YIG thin films are single crystalline, but such a sharp maximum as in [88] is not visible in our data.

In contrast, Rezende et al. calculated the temperature dependence of the longitudinal SSE [13] in YIG/Pt bilayers based on magnon population and lifetime. With lowering T, the magnon population decreases whereas the lifetime increases, leading to a competition of both factors and resulting in a broad peak of the SSE voltage at about 120 K. This calculation also yields a vanishing SSE voltage at $T = 0$ due to the vanishing of the thermal magnon population. These authors verified their theoretical predictions by longitudinal SSE measurements in a YIG film with thickness 8 µm covered by 6 nm of Pt. The results are shown in Fig. 4.9 b): the SSE voltage vanishes at $T = 0$ K as expected from calculations, increases until reaching 100 K and above this the signal is constant. This behaviour can be reproduced by calculations (solid lines in Fig. 4.9 b)) based on the presented model. A similar behaviour of the SSE voltage was found experimentally in $NiFe_2O_4$/Pt samples by Meier et al. [11].

Our SSE measurements are qualitatively comparable to the ones by Rezende et al. [13] depicted in Fig. 4.9 and Meier et al. [11]. However, in our sample the SSE voltage does not seem to vanish at very low T_{cryo}. Still, in our setup it is very challenging to determine the

exact microwave heating in the Pt layer and the actual sample temperature. As discussed in Sect. 4.1.4, the temperature scale in Fig. 4.8 was not corrected because the heating power can only be approximated. Therefore our measurements might not be completely reliable at very low temperatures and the low temperature behaviour of our sample can only qualitatively be compared to [13] and [11].

It might also be interesting to compare samples with different YIG and Pt thicknesses, since the measurements by Rezende et al. and Uchida et al. where conducted in samples with a much thicker YIG layer. It was indicated previously by Niklas Roschewski in his Master's thesis, that the temperature dependence of the SSE voltage might also depend on the YIG and Pt layer thickness [42]. However, he examined the current induced SSE voltage [41] in a sample of similar YIG and Pt thicknesses (61 nm and 11 nm respectively) and found a minimum of the voltage at low temperatures. This is not consistent with the results shown in Fig. 4.8 a) and needs to be further investigated.

Even though our results are similar to measurements by Rezende et al., there are still different temperature dependencies observed by other groups [42, 88]. An examination of other YIG/Pt samples and a more precise temperature calibration at low T in our setup would be necessary in order to deduce a clear temperature dependence of the spin Seebeck effect.

Finally, we come to the coercive field which can also be extracted from the dc voltage (see Fig. 4.8 b)). $\mu_0 H_c$ increases from 5 mT at T_{cryo}= 295 K to 23 mT at T_{cryo}= 5 K. This is in agreement with $M(H)$ SQUID measurements performed on the same thin film at different temperatures (see inset Fig. 4.4) and previous measurements in YIG [61, 71]. The coercive field determines the external magnetic field necessary to rotate the sample magnetization by 180° during a field sweep [74]. Therefore $\mu_0 H_c$ depends on the ratio between two energies: the crystalline anisotropy energy, which tends to align the magnetization with an easy magnetic axis and the Zeeman energy $-\mu_0 M H_0$, which tends to align the magnetization with the external field. If the anisotropy energy increases faster with lowering temperatures than the Zeeman energy, which is proportional to M, the coercive field increases.

To summarize this chapter, we have measured the temperature dependence of ferromagnetic resonance position and linewidth in a YIG/Pt bilayer. We have simultaneously examined the dc voltage, which is a superposition of two resonant effects, viz. spin pumping and microwave rectification, and the non resonant SSE induced by microwave heating in the Pt layer, as function of temperature. An increase of the ferromagnetic resonance field, as well as a decrease of the linewidth and the coercive field with increasing temperature were observed, which can be attributed to magnetic anisotropy effects. We also discussed the sign and temperature dependence of the spin pumping and rectification amplitudes,

and found them to be consistent with theoretical expectations. The temperature dependence of the SSE voltage we observed, is in agreement with previous measurements by other groups, but probably needs further examination.

In anticipation of the following measurements in compensated garnets, we want to emphasize here, that (as expected for YIG/Pt) spin pumping and spin Seebeck voltages are of opposite sign in the whole temperature range from T_{cryo}= 5 K to T_{cryo}= 295 K. The signs of both voltages do not change over the temperature range investigated.

4.2.2 Temperature dependent spin pumping and spin Seebeck effect measurements in InYGdIG/Pt

After examining the YIG/Pt reference sample, we will now discuss magnetically compensated materials. This kind of material is interesting since, they allow the separate investigation of magnetization and angular momentum. Furthermore, the different sublattice magnetizations and angular momenta have different temperature dependencies (see Sect. 1.5 and Chap. 3). Examining the spin pumping and SSE as a function of temperature should therefore also yield information about the sublattices involved in those effects.

In the following section, the results of the experiments on the InYGdIG/Pt sample are presented, while results from experiments on GdIG/Pt are presented in Sect. 4.2.3.

4.2.2.1 Magnetization curve of InYGdIG/Pt

Before turning to the examination of the dc voltage, we will start with the temperature dependence of the magnetization M of the InYGdIG/Pt sample. M was obtained by SQUID magnetometry in an external field of 1 T applied along the film plane and is shown in Fig. 4.10 a). The magnetization orientation of the net Fe sublattice and the Gd sublattice are represented by purple and green arrows respectively, and the black arrow indicates the direction of the external field H_0. At $T_{\mathrm{sample}} = 85\,\mathrm{K}$, $M(\mu_0 H_0 = 1\,\mathrm{T})$ reaches a minimum. This is the magnetization compensation point $T_{\mathrm{comp,\,M}}$ marked by a black line in Fig. 4.10 a). $M(\mu_0 H_0 = 1\,\mathrm{T})$ does not reach 0, which might be caused by the fact that all magnetic moments of the Fe and Gd sublattices do not change orientation simultaneously at exactly the same temperature. This behaviour is similar to the domain formation in a ferromagnet, where not all domains switch simultaneously when the magnetic field orientation is inversed, leading to a magnetic hysteresis loop [74]. There is therefore no temperature at which all magnetic moments in the InYGdIG/Pt sample are exactly compensated, so that the magnetization does not completely vanish but goes through a minimum at $T_{\mathrm{comp,\,M}}$. In addition to this, spin canting near $T_{\mathrm{comp,\,M}}$ has to be considered as well, as discussed in Sect. 1.5 [53]: even though in the SQUID measurements an external field of only 1 T is applied, around $T_{\mathrm{comp,\,M}}$ this might be sufficient to enter

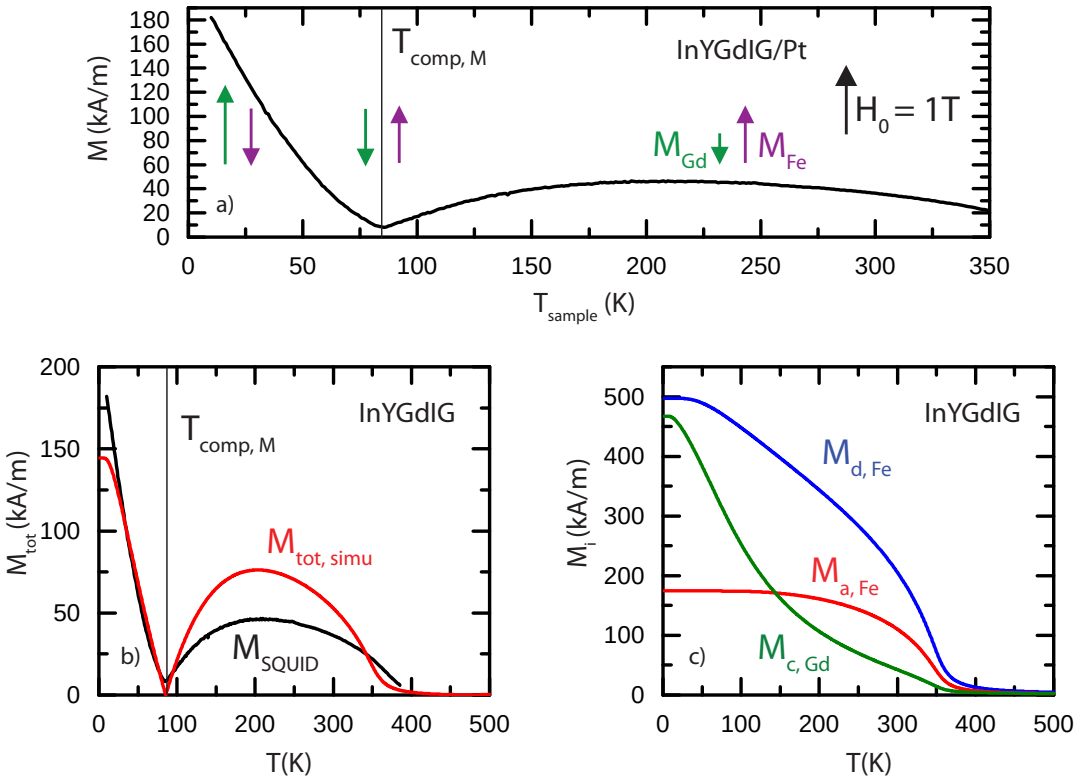

Figure 4.10: a) Magnetization as a function of temperature of the InYGdIG/Pt sample obtained by SQUID magnetometry measurements. The external magnetic field $\mu_0 H_0 = 1\,\mathrm{T}$ applied in the film plane (black) as well as both sublattice magnetizations (purple for the net Fe sublattice and green for Gd) are symbolized by arrows. The compensation of magnetization is indicated by the black line at $T_{\mathrm{sample}} = 85\,\mathrm{K}$. b) The black line represents the experimental SQUID data and the red line is the result of the calculation of the magnetization presented in Sect. 3.1. c) Absolute values of the sublattice magnetizations in InYGdIG obtained by simulation as well.

the spin canting phase, since the critical field decreases in the compensation region (see Fig. 1.7 b)). When the magnetizations are canted, they do not compensate each other, so that there is a finite magnetization left.

In Fig. 4.10 b), the SQUID data is again shown as a black line. The red line is a fit to the experimental data using the simulation for InYGdIG presented in Sect. 3.1. The calculation reproduces the experimental data well with a magnetization compensation temperature $T_{\mathrm{comp,\,M}} = 85\,\mathrm{K}$, for $g_{\mathrm{Fe,\,d}} = 2.0047$, $g_{\mathrm{Fe,\,a}} = 2.003$ and $g_{\mathrm{Gd,\,c}} = 1.994$. These g values were determined from measurements in YIG [75] and GdIG [77] and can also be used in InYGdIG. For the simulation in Fig. 4.10, doping concentrations of 8 % of In^{3+} on the d lattice, 50 % of In^{3+} on the a lattice and 41 % of Y^{3+} on the c lattice were used. These values are consistent with the doping of the target material $(Gd_2Y)(Fe_4In)O_{12}$ used

to grow this sample (see Sect. 2.2). We would have predicted a doping of 33.33 % of Y^{3+} on the *c* lattice and 50 % of In^{3+} on the *a* lattice, since the In^{3+} is expected to substitute mainly on the *a* lattice [64]. The remaining deviations might be due to the fact that the incorporation rates of the dopants into the GdIG crystal during the growth process are different for different ions and depend on the growth parameters. There are other material compositions, for which the simulation also yields a good match to the experimental data, but those are very different from the target composition and we therefore used the doping values given above.

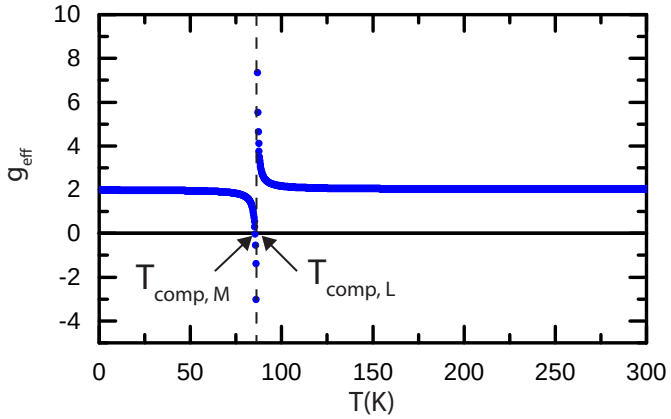

Figure 4.11: Effective g value in InYGdIG/Pt calculated with $g_{\mathrm{Fe,\,d}} = 2.0047$, $g_{\mathrm{Fe,\,a}} = 2.003$ and $g_{\mathrm{Gd,\,c}} = 1.994$ [75, 77]. $T_{\mathrm{comp,\,M}}$ and $T_{\mathrm{comp,\,L}}$ are indicated by black arrows.

With the g values used for the simulation of the magnetization curve, the effective g value as a function of temperature in our InYGdIG/Pt thin film can be calculated using Eq. (1.27), as described in Sect. 3.2. The result is shown in Fig. 4.11: g_{eff} is 0 at $T_{\mathrm{comp,\,M}} = 85\,\mathrm{K}$ and diverges at $T_{\mathrm{comp,\,L}} = 86\,\mathrm{K}$, so that the compensation of angular momentum and magnetization are only 1 K apart. This difference between the two compensation points is even smaller than the 3 K difference found for GdIG (see Sect. 3.2), even though the same g values were used for both materials. This might be caused by the dilution of magnetic moments in InYGdIG which reduces the magnetizations.

We will now proceed to the discussion of FMR, spin pumping and SSE experiments in InYGdIG/Pt, which were conducted simultaneously as a function of magnetic field at various temperatures ranging from $T_{\mathrm{cryo}} = 6\,\mathrm{K}$ to $T_{\mathrm{cryo}} = 295\,\mathrm{K}$.

The measured dc voltage is a superposition of a resonant voltage, consisting of spin pumping and microwave rectification, and the non resonant SSE voltage, so that $V_{\mathrm{DC}} = V_{\mathrm{SSE}} + V_{\mathrm{SP}} + V_{\mathrm{rect}}$ (see Sect. 1.4). The voltages recorded as a function of the external magnetic field applied in the film plane for $T_{\mathrm{cryo}} = 10\,\mathrm{K}$, $T_{\mathrm{cryo}} = 40\,\mathrm{K}$ and $T_{\mathrm{cryo}} = 296\,\mathrm{K}$ are shown in Fig. 4.12 as black lines. The dc voltage has a pronounced temperature

dependence. First of all, the spin pumping amplitude, i.e. the part of the dc voltage that is symmetric around $\mu_0 H_{\mathrm{res}}$ and changes its sign upon magnetic field inversion (see Sect. 1.2.3), is much larger at room temperature than at lower temperatures. At low temperatures, the resonant signal is dominated by an antisymmetric signal attributed to microwave rectification, as discussed in Sect. 1.3. These effects, as well as the temperature dependence of resonance position and linewidth, will be analyzed in detail in the following sections. Furthermore, the SSE voltage yields a characteristic magnetization hysteresis loop with a strongly temperature dependent coercive field. We observe two sign changes in the SSE voltage, since the amplitude $2B$ (see Fig. 4.12) is negative at $T_{\mathrm{cryo}} = 296\,\mathrm{K}$ and $T_{\mathrm{cryo}} = 10\,\mathrm{K}$, and positive at $T_{\mathrm{cryo}} = 40\,\mathrm{K}$. These sign changes are expected since the same behaviour was found in GdIG/Pt [80], but will also be examined in the following discussion in more detail.

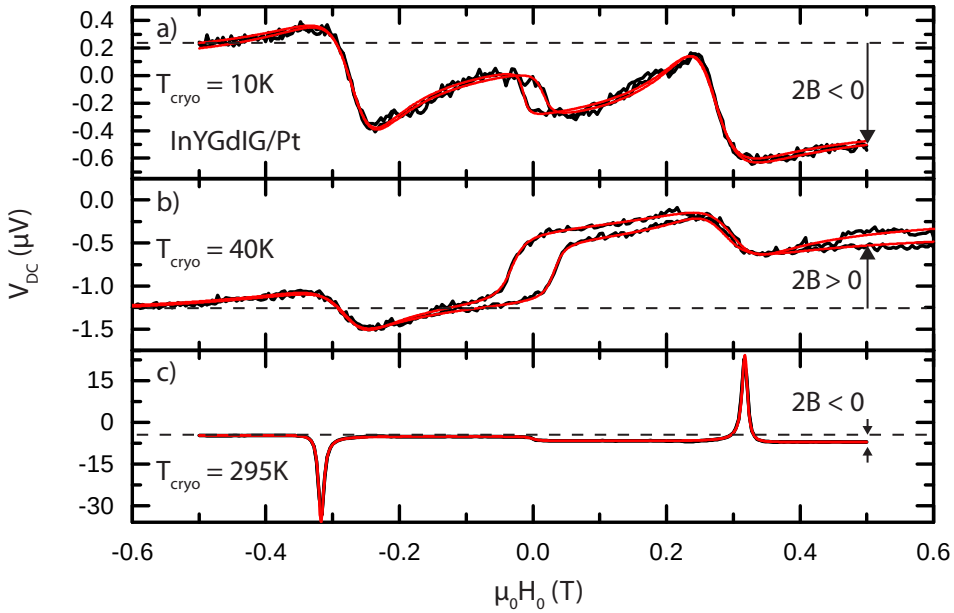

Figure 4.12: DC voltage (black line) in the InYGdIG/Pt sample as a function of the external magnetic field for T_{cryo}= 10 K (a), T_{cryo}= 40 K (b) and T_{cryo}= 295 K (c). The red line represents the fit from Eq. 1.26.

All measurements were fitted using Eq. (1.26) for the dc voltage (red line in Fig. 4.12), in order to extract the same parameters (H_{res}, ΔH, L, D, B) as for the YIG/Pt reference sample.

4.2.2.2 Spin Seebeck effect and coercive field

We will start with the analysis of the spin Seebeck effect and first analyze the SSE voltage amplitude $2B$ extracted using Eq. (1.26). The results are shown in Fig. 4.13 a), where the values extracted from the magnetic field up and down sweep are represented by red

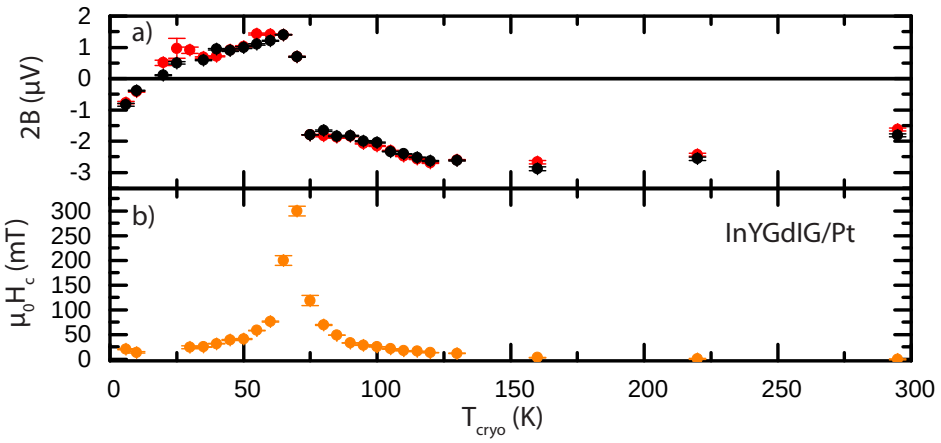

Figure 4.13: a) Spin Seebeck amplitude $2B$ extracted using Eq. (1.26) in the InYGdIG/Pt sample as a function of cryostat temperature, the error bars represent the read out errors. The red and black dots represent the values extracted from magnetic field up and down sweep respectively. b) Coercive field obtained from the fit to the spin Seebeck hysteresis, the errors are the standard deviation from the fit.

and black dots respectively. Between $T_{\mathrm{cryo}} = 75\,\mathrm{K}$ and room temperature the SSE voltage is negative as it was the case for the YIG/Pt reference sample, which was mounted in the same configuration. An absolute maximum of $2.88\,\mu\mathrm{V}$ of the SSE voltage is reached around $T_{\mathrm{cryo}} = 160\,\mathrm{K}$ and below this, the amplitude decreases and goes to 0 at about $72\,\mathrm{K}$ and changes sign. There is a second sign change at approximately $T_{\mathrm{cryo}} = 25\,\mathrm{K}$, where the SSE voltage becomes negative again.

The two sign changes in the SSE seemingly have different natures, since the upper one at $T_{\mathrm{cryo}} = 72\,\mathrm{K}$ is rather abrupt and the lower one at $T_{\mathrm{cryo}} = 25\,\mathrm{K}$ rather smooth. The upper abrupt sign change can be attributed to the magnetization compensation point $T_{\mathrm{comp,\,M}}$, at which all the sublattices switch direction [90]. Due to microwave heating in the Pt layer the sample temperature has to be corrected to $T_{\mathrm{sample}} = T_{\mathrm{cryo}} + 18\,\mathrm{K}$ (see Sect. 4.1.4), so that the upper sign change takes place at $T_{\mathrm{sample}} \approx 90\,\mathrm{K}$. This is higher than $T_{\mathrm{comp,\,M}} = 85\,\mathrm{K}$ from SQUID magnetometry, indicating that a more precise calibration would be necessary, as dicussed in Sect. 4.1.4.

In order to validate the statement that the upper SSE sign change takes place at $T_{\mathrm{comp,\,M}}$, we can additionally analyze the coercive field $\mu_0 H_{\mathrm{c}}$, which was extracted from the SSE voltage as a function of cryostat temperature (see Fig. 4.13 b)). At room temperature $\mu_0 H_{\mathrm{c}}$ is very small at approximately $0.1\,\mathrm{mT}$. With decreasing temperature the coercive field increases strongly and becomes very large around $T_{\mathrm{cryo}} = 72\,\mathrm{K}$, where the upper sign change in the SSE voltage takes place. Below $T_{\mathrm{cryo}} = 60\,\mathrm{K}$, $\mu_0 H_{\mathrm{c}}$ decreases again. Due to the fact that the SSE voltage is very small around the second sign change of the SSE, the coercive field could not be evaluated at temperatures around $30\,\mathrm{K}$.

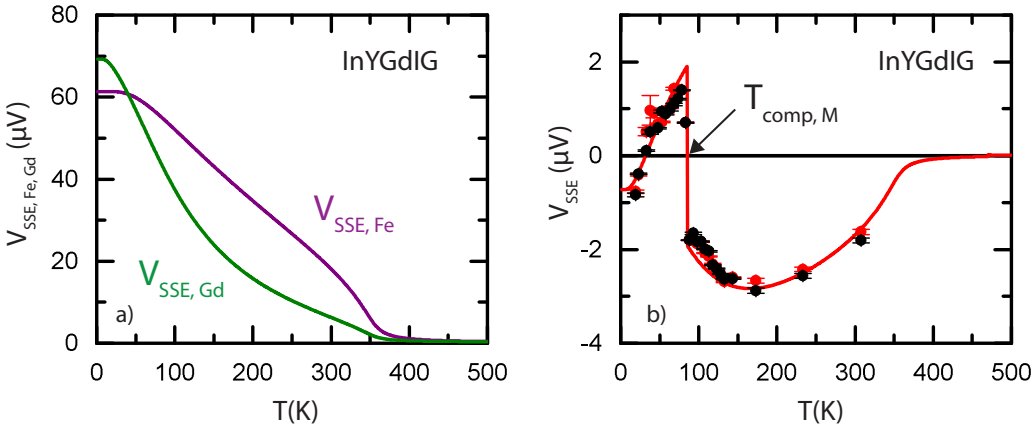

Figure 4.14: a) Simulation of the SSE contributions from the net Fe sublattice (purple) and the Gd sublattice (green) in InYGdIG as a function of temperature. b) The black and red dots represent the SSE voltage extracted from experiments, the red line is the total SSE voltage obtained from the simulation assuming that the Fe and Gd sublattices contribute with different efficiencies to the SSE voltage.

The coercive field defines the external magnetic field that has to be applied to the ferrimagnetic material in order to rotate the total magnetization by 180° [74]. The higher the crystalline anisotropy of the sample, the higher the applied magnetic field has to be in order to switch all magnetic moments. Therefore a large crystalline anisotropy field leads to a large coercive field. The crystalline anisotropy field is proportional to K/M with K the crystalline anisotropy constant and M the saturation magnetization. At $T_{\mathrm{comp,\,M}}$ M goes to 0 and K/M becomes very large, no matter how small K is. Therefore at the magnetization compensation temperature a strong increase of the coercive field is expected [26], which is consistent with the experimental results shown in Fig. 4.13. Since the SSE changes sign at the temperature where $\mu_0 H_{\mathrm{c}}$ diverges, this is an additional evidence of the fact that the SSE really changes sign at $T_{\mathrm{comp,\,M}}$.

The behaviour of the SSE in InYGdIG/Pt is very similar to the one observed by Geprägs et al. [80] in GdIG/Pt thin films. They also found an abrupt sign change at a temperature corresponding to the magnetization compensation point at T_{sample}= 286 K and a second smoother one at T_{sample}= 68 K.

Both sign changes of the SSE in a magnetically compensated material can be explained by a qualitative picture: we assume that the SSE contribution of each sublattice is proportional to its magnetization, that the Fe sublattices contribute equally with a factor 1 and the Gd sublattice with a factor $\eta = 0.75$, such that

$$V_{\mathrm{SSE,\,total}} = \sum_i V_{\mathrm{SSE,\,M}_i} = c \cdot (M_{d,Fe} - M_{a,Fe} - \eta M_{c,Gd}) \tag{4.2}$$

with $V_{\mathrm{SSE,\,M}_{d,Fe}} = cM_{d,Fe}$, $V_{\mathrm{SSE,\,M}_{a,Fe}} = cM_{a,Fe}$ and $V_{\mathrm{SSE,\,M}_{c,Gd}} = c\eta M_{c,Gd}$. The sublattice magnetizations M_i are the same as in Fig. 4.10 obtained from a mean field calculation as described in Sect. 3.1. The scaling factor $c = 1.8 \times 10^{-10}\mathrm{V\,m\,A^{-1}}$ is a phenomenological constant introduced to convert the magnetization into a voltage of the same order of magnitude as the one observed in the experiment. The resulting temperature dependence of the SSE voltage from the net Fe sublattices (purple line) and from Gd (green line) are depicted in Fig. 4.14 a). The two curves cross each other at 40 K, yielding the low temperature zero-crossing observed in the experiment. If we add the right signs of the magnetization for each sublattice contribution, i.e. negative for Fe and positive for Gd at high T, so that opposite magnetizations yields opposite voltages, and switch those signs at the magnetization compensation point, we are able to qualitatively reproduce the experimental data. This is shown in Fig. 4.14 b), where the experimental data is represented by red and black dots (magnetic field up and down sweep) and the result from the simulation by a red line. The temperature of the experimental data was corrected to $T_{\mathrm{sample}} = T_{\mathrm{cryo}} + 13\,\mathrm{K}$ to match the compensation temperature $T_{\mathrm{comp,\,M}} = 85\,\mathrm{K}$ of the calculation. At high T the Fe sublattice dominates the spin Seebeck signal, giving rise to a negative SSE voltage, similar to the YIG/Pt reference sample (see Fig. 4.8). In this temperature range, the Gd sublattice contribution is very small and the sample behaves like YIG/Pt in terms of SSE voltage. The SSE amplitude qualitatively follows the magnetization curve shown in Fig. 4.10 a) and decreases to higher T as we approach the Curie temperature. At the compensation point, the sublattice magnetizations change direction, so that the SSE voltage changes sign with the still dominating Fe contribution and becomes positive. At lower temperatures, the Gd sublattice gains importance. This leads to a slow decrease of the SSE voltage, until the Gd eventually dominates, so that a smooth second sign change takes place at a lower temperature. The constant c and the Gd sublattice efficiency were chosen empirically to match the results from the experiment.

The results in Fig. 4.13 a) therefore suggest that the spin Seebeck effect in InYGdIG/Pt does not depend on the net magnetization, but that Fe and Gd sublattices contribute with different efficiencies to the SSE, leading to two sign changes in the SSE voltage.

4.2.2.3 Resonance field

We will now turn to the resonant voltage (the voltage appearing in FMR) and start by determining the resonance field $\mu_0 H_{\mathrm{res}}$ using Eq. (1.26). The resonance field can also be extracted from FMR measurements, since FMR and spin pumping are expected at the same field (see Sect. 1.2.3), but as discussed for the YIG/Pt sample, the signal to noise ratio in the FMR detection is smaller than in the voltage measurements, leading to larger errors in the determination of the resonance field. We will thus focus on the spin pumping voltage to determine $\mu_0 H_{\mathrm{res}}$.

The resulting resonance field for the in plane configuration (see Fig. 4.1) is shown in

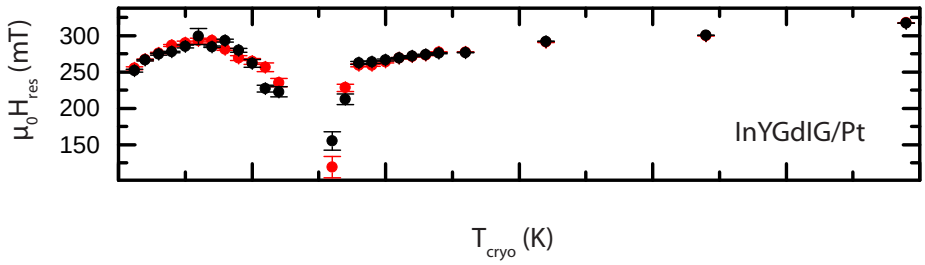

Figure 4.15: Temperature dependence of the resonance field determined from the spin pumping voltage in InYGdIG/Pt, the error bars represent the standard deviation from the fit. The red and black dots represent the values extracted from magnetic field up and down sweep respectively.

Fig. 4.15 as a function of the cryostat temperature, the red and black dots represent the data extracted from magnetic up and down sweep respectively. Starting at 317 mT at room temperature the resonance field decreases slightly, similar to the YIG/Pt sample (see Fig. 4.6). Around $T_{\mathrm{cryo}} = 72\,\mathrm{K}$, $\mu_0 H_{\mathrm{res}}$ decreases strongly and then increases again reaching a local maximum of 293 mT at $T_{\mathrm{cryo}} = 35\,\mathrm{K}$. At very low temperatures, the resonance field again decreases slightly.

When approaching $T_{\mathrm{cryo}} = 72\,\mathrm{K}$ it is increasingly difficult to detect the spin pumping signal and extract $\mu_0 H_{\mathrm{res}}$, so that at some temperatures no data is available. As we will see later, this is due to the fact that in this temperature region the linewidth is very large and the spin pumping amplitude disappears.

We have seen in the discussion of the SSE voltage, that the magnetization compensation temperature in the InYGdIG/Pt sample corresponds to $T_{\mathrm{cryo}} = 72\,\mathrm{K}$. It therefore seems that we observe a drop in the ferromagnetic resonance field at $T_{\mathrm{comp,\,M}}$.

Our results are consistent with the strong decrease of $\mu_0 H_{\mathrm{res}}$, around the compensation point observed by Calhoun et al. [79] and Rodrigue et al. [77] in GdIG.

In order to understand the behaviour of $\mu_0 H_{\mathrm{res}}$, we start with the simplified FMR equation

$$\omega = \gamma_{\mathrm{eff}}\ \mu_0 H_{\mathrm{res}} \tag{4.3}$$

where anisotropy terms are neglected. As discussed in Sect. 1.5, the effective gyromagnetic ratio γ_{eff} given by Eq. (1.27) diverges at the angular momentum compensation point $T_{\mathrm{comp,\,L}}$ and goes to 0 at the magnetization compensation point $T_{\mathrm{comp,\,M}}$ (see Fig. 4.11). Equation 4.3 then yields a drop in $\mu_0 H_{\mathrm{res}}$ when γ_{eff} diverges, so that a strong decrease in $\mu_0 H_{\mathrm{res}}$ around $T_{\mathrm{comp,\,L}}$ is expected.

According to Eq. (4.3), we should also observe an increase in $\mu_0 H_{\mathrm{res}}$ at $T_{\mathrm{comp,\,M}}$, where

γ_{eff} vanishes. Such a behaviour was observed by J. Pauleve in Lithium-Chromium Ferrites [78] and by T. McGuire in Nickel Ferrite Aluminates [91]. However, a pronounced increase in $\mu_0 H_{\text{res}}$ is not visible in our data in Fig. 4.15 and a more thorough analysis of the resonance condition is necessary.

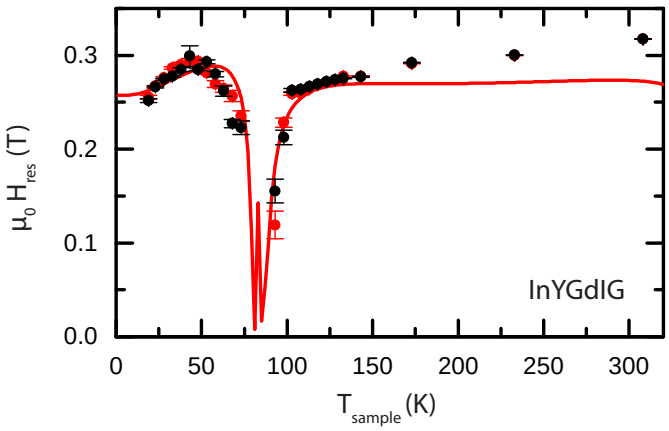

Figure 4.16: The black and red dots represent the in plane FMR resonance field extracted from the spin pumping voltage as a function of sample temperature $T_{\text{sample}} = T_{\text{cryo}} + 13\,\text{K}$. The red line is the result of the simulation presented in Sect. 3. The sharp peak in the compensation region is a numerical artifact due to the fact that the resonance field cannot be negative.

Using Eq. (4.3) is only justified as long as anisotropy fields are small compared to the external field. This is not the case here, since the anisotropy (i.e. shape anisotropy in a thin film and crystalline anisotropy) cannot be neglected [77], and a free energy calculation as described in Sect. 3.3 is necessary to determine the effective magnetic field acting on the magnetization. The crystalline anisotropy field has a contribution proportional to K/M to the effective magnetic field [26, 28] with K the anisotropy constant and M the magnetization. Therefore even for a small K, the anisotropy field diverges at $T_{\text{comp, M}}$, which in a simplified picture, compensates the decrease of γ_{eff}, so that there is no visible increase of FMR simu around $T_{\text{comp, M}}$ [78]. The details of these calculations are not straightforward and we use a simulation based on the free energy ansatz to determine the expected resonance field as a function of temperature in InYGdIG (see Sect. 3.3). The total magnetization determined in Sect. 4.2.2.1 using the mean field approach described in Sect. 3.1 was used. In this simulation, approximations were made, for example that the anisotropy constant K is independent of temperature. Measurements show that this is not the case and that the anisotropy increases upon lowering T [77].

It is however possible to reproduce the behaviour of the experimentally determined resonance field, as shown in Fig. 4.16, where the experimental data is represented by red and black dots as a function of temperature corrected to $T_{\text{sample}} = T_{\text{cryo}} + 13\,\text{K}$ in order to match $T_{\text{comp, M}} = 85\,\text{K}$ from the simulation (see Sect. 4.2.2.1). The red line is the result of

the simulation, which reproduces nicely the strong decrease in resonance field around the compensation temperature. The sharp peak in the compensation region is a numerical artifact caused by the fact that only positive values for the resonance field are given out. The high temperature behaviour of the resonance field is not exactly reproduced by the simulation, but this may be attributed to the fact that a temperature independent anisotropy constant was used.

The drop in resonance field can therefore not simply be attributed to $T_{\mathrm{comp,\,L}}$, as suggested by Eq. (4.3), since the divergence of the anisotropy field near $T_{\mathrm{comp,\,M}}$ also contributes to the behaviour of $\mu_0 H_{\mathrm{res}}$. We have seen that the angular momentum and magnetization compensation temperatures are only a few K apart (see Fig. 4.11) and can therefore not be distinguished in these measurements.

The simulation also reproduces the low T behaviour of $\mu_0 H_{\mathrm{res}}$, i.e. the slight decrease at low temperatures. This effect was observed as well by Calhoun et al. [79] and can be attributed to an increase of the magnetization and/or anisotropy with decreasing temperature [77], similar to the observations made in the YIG/Pt reference sample (see Sect. 4.2.1.1).

4.2.2.4 FMR linewidth

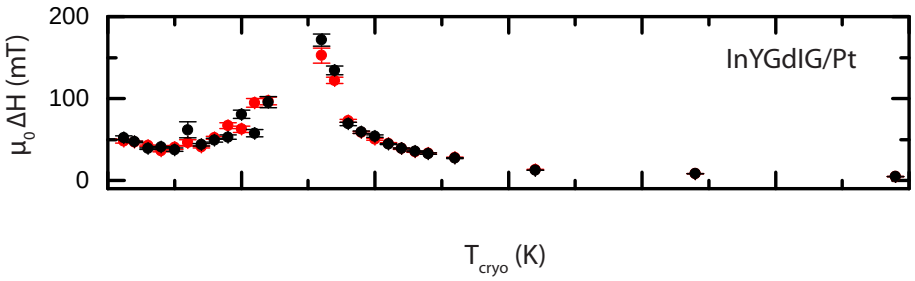

Figure 4.17: Half width at half maximum in InYGdIG/Pt as a function of temperature for an in plane external magnetic field. The red and black dots represent the values extracted from magnetic field up and down sweep respectively. The error bars indicate the standard deviation from the fit.

After analyzing the temperature dependence of the resonance field in the InYGdIG/Pt sample, we will now proceed to the analysis of the resonance linewidth for an in plane magnetic field. It is possible that the FMR line consists of multiple lines, we will however treat it as one line in the following analysis. The half width at half maximum extracted from spin pumping measurements using Eq. (1.26) is shown in Fig. 4.17.

We can see a large increase in linewidth to over 100 mT around $T_{\mathrm{cryo}} = 72\,\mathrm{K}$. Here again, the measurements could not be analyzed close to the compensation region because the

spin pumping linewidth increases to the point that the resonance can no longer be observed.

This divergence effect in linewidth was also observed previously [77, 79] and was attributed to the sharp increase in anisotropy at the magnetization compensation temperature $T_{\mathrm{comp,\,M}}$, similar to the divergence of the coercive field.

Another explanation for the divergence of linewidth is a divergence of the effective damping coefficient α_{eff} at $T_{\mathrm{comp,\,L}}$ as discussed by Giles et al. [58]

$$\alpha_{\mathrm{eff}} = \frac{\frac{\alpha_1 M_1}{\gamma_1} + \frac{\alpha_2 M_2}{\gamma_2}}{\frac{M_1}{\gamma_1} - \frac{M_2}{\gamma_2}} \tag{4.4}$$

where $\alpha_{1,2}$ and $\gamma_{1,2}$ are the damping coefficients and gyromagnetic ratios of two antiferromagnetically coupled sublattices with absolute magnetization values $M_{1,2}$. However, since in InYGdIG/Pt $T_{\mathrm{comp,\,L}}$ and $T_{\mathrm{comp,\,M}}$ are only a few kelvin apart, the divergence of the FMR linewidth cannot be attributed with certainty to one of the two temperatures.

4.2.2.5 Resonant voltage $V_{\mathrm{res}} = V_{\mathrm{SP}} + V_{\mathrm{rect}}$

We will now proceed to the analysis of the resonantly induced voltage amplitude. The resonant voltage consists of a symmetric signal with amplitude L, which changes sign upon magnetic field inversion, attributed to spin pumping and of an antisymmetric signal of amplitude D attributed to microwave rectification. Both amplitudes L and D (spin pumping and rectification respectively) were extracted using Eq. (1.26) as shown in Fig. 4.18 a) as a function of cryostat temperature. The red dots represent the results from the magnetic field upsweep, the black dots the ones from the downsweep and the error bars represent the standard deviation from the fit function. At room temperature, similar to the YIG/Pt sample, the spin pumping amplitude is positive, while the rectification amplitude is negative. Therefore at high temperatures, the InYGdIG/Pt sample yields the same sign for spin pumping and rectification as the YIG/Pt reference sample. This is similar to the observations in the SSE voltage in InYGdIG/Pt (see Fig. 4.13), where the Gd sublattice can be neglected at high T, and mainly the Fe sublattices contribute, so that the InYGdIG/Pt behaves just like YIG/Pt at high T.

At room temperature, the spin pumping voltage L is about an order of magnitude larger than the rectification voltage D, as it is the case in the YIG/Pt sample. When approaching the compensation region both resonant signals decrease, and vanish around $T_{\mathrm{cryo}} = 80\,\mathrm{K}$. Below $T_{\mathrm{cryo}} = 60\,\mathrm{K}$, the resonance reappears and L and D slightly increase to very low temperatures. The inset in Fig. 4.18 a) shows a close up of the spin pumping voltage in the compensation region. The amplitude L does not only vanish but changes sign at $T_{\mathrm{cryo}} = 100\,\mathrm{K}$. Below $T_{\mathrm{cryo}} = 60\,\mathrm{K}$ the signal is positive again, yielding a second sign change around $T_{\mathrm{comp,\,M}}$.

It becomes clear in the field sweeps, that the antisymmetric rectification voltage dom-

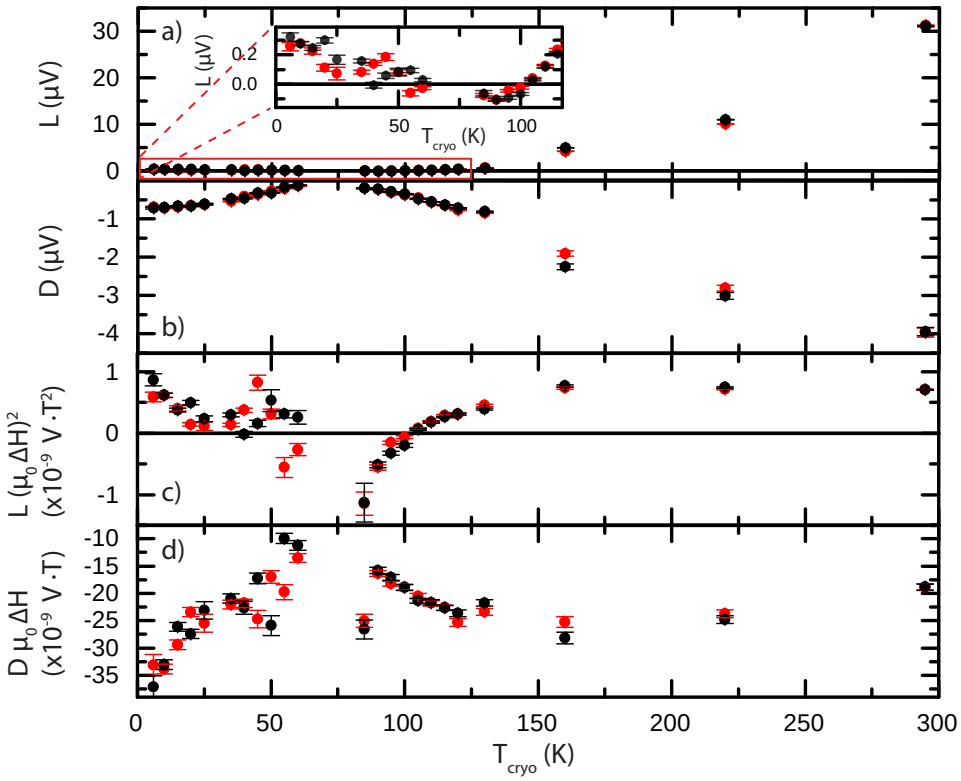

Figure 4.18: a) Spin pumping amplitude L and b) microwave rectification amplitude D, as a function of cryostat temperature in InYGdIG/Pt. The inset in a) shows a close up of the compensation point region for the spin pumping amplitude L. c) "spin pumping efficiency" $L \cdot (\mu_0 \Delta H)^2$ and d) "rectification efficiency" $D \cdot \mu_0 \Delta H$ as a function of cryostat temperature. The red dots represent the data extracted from the magnetic field upsweep and the black dots the results from the downsweep.

inates over the spin pumping voltage at low T (see Fig. 4.12). This is also visible in Fig. 4.18 a) and b) where L is smaller than D between $T_{\mathrm{cryo}} = 0\,\mathrm{K}$ and $125\,\mathrm{K}$. Such a behaviour can be expected, since the spin pumping amplitude is proportional to $\frac{1}{\Delta H^2}$ and the rectification only to $\frac{1}{\Delta H}$ (see Sect. 1.2.3 and 1.3). Therefore when ΔH continuously increases (see Fig. 4.17), the spin pumping is reduced much faster than the rectification voltage.

Due to the fact that both the spin pumping and the rectification amplitude are strongly dependent on FMR linewidth, the relationship between the magnetization in the ferrimagnet and the spin current injected into the Pt is better described by the spin pumping and rectification efficiencies (see Sect. 1.2.3 and 1.3).

The spin pumping amplitude is proportional to $\frac{1}{\Delta H^2}$ (see Eq. 1.16) and we therefore analyze the efficiency $L \cdot (\mu_0 \Delta H)^2$, which is plotted in Fig. 4.18 b). The values extracted from the magnetic field upsweep are represented by red dots, while the ones from the

downsweep are depicted as black dots. In the compensated InYGdIG/Pt sample, looking at the spin pumping efficiency turns out to be even more necessary than in the YIG/Pt reference sample, since the linewidth has a very pronounced temperature dependence, which obviously influences the spin pumping amplitude. Around the compensation region the linewidth diverges and the spin pumping signal goes to 0, whereas at room temperature the linewidth is reduced and L attains a maximum of about 32 µV. Calculating the spin pumping efficiency allows us to exclude the temperature dependence that is due to the linewidth and the spin pumping efficiency then reflects the behaviour of the remaining parameters, viz. resistance, spin mixing conductance, spin Hall angle and spin diffusion length (see Eq. (1.15)). Contrary to YIG/Pt, no resistance measurements in InYGdIG/Pt were conducted in this setup as a function of temperature, but it is known from other experiments (see Sect. 5.1.2) that the Pt resistance increases linearly with temperature and the change is about 200 Ω between 50 K and 300 K. Since the spin pumping voltage depends linearly on the sample resistance R (see Eq. (1.15)), $L \cdot (\mu_0 \Delta H)^2/R$ has the same qualitative behaviour around T_{comp}, as $L \cdot (\mu_0 \Delta H)^2$ and the resistance is not essential to understanding the spin pumping behaviour in InYGdIG/Pt in the compensation region.

The spin pumping efficiency $L \cdot (\mu_0 \Delta H)^2$ remains constant from $T_{\mathrm{cryo}} = 160\,\mathrm{K}$ to $T_{\mathrm{cryo}} = 296\,\mathrm{K}$ and below $T_{\mathrm{cryo}} = 60\,\mathrm{K}$, which is consistent with the fact that the pronounced increase of L at room temperature is due to the decrease of linewidth as shown in Fig. 4.17. The spin pumping efficiency in this temperature region is of the same order of magnitude as $L \cdot (\mu_0 \Delta H)^2$ in YIG/Pt, i.e about 1×10^{-9} A T^2 (see Fig 4.7). At $T_{\mathrm{cryo}} = 100\,\mathrm{K}$ the efficiency changes sign with L, until $T_{\mathrm{cryo}} = 80\,\mathrm{K}$, where the resonant signal is no longer visible. Below $T_{\mathrm{cryo}} = 60\,\mathrm{K}$ the spin pumping voltage is positive and does not change strongly until the lowest measured temperature. We thus find that the change in the spin pumping efficiency is most likely connected to the magnetization compensation in InYGdIG, since as a function of temperature, the efficiency changes strongly only around the compensation temperature.

This kind of sign change of the spin pumping voltage in a magnetically compensated material has never been observed before. The lower sign change is close to the compensation region around $T_{\mathrm{cryo}} = 72\,\mathrm{K}$ and could be attributed to the change of orientation of the sublattice magnetizations or angular momenta at $T_{\mathrm{comp,\,M}}$, similar to the sign change of the spin Seebeck voltage at $T_{\mathrm{comp,\,M}}$ (see Sect. 4.2.2.2). However, contrary to the SSE voltage which yields a second low temperature sign change below $T_{\mathrm{comp,\,M}}$, the second sign change of the spin pumping voltage takes place at a temperature above $T_{\mathrm{comp,\,M}}$. The low temperature sign change of the SSE can be explained by the phenomenological model presented in Sect. 4.2.2.2, based on the assumption that the Gd sublattice contributes with a smaller efficiency to the SSE voltage than the Fe sublattice. This model can only yield a sign change at $T > T_{\mathrm{comp,\,M}}$ as observed in the spin pumping voltage, if the efficiency of the Gd sublattice was larger than the Fe sublattice efficiency. We find that for a Gd spin pumping efficiency 1.2 times larger than the Fe spin pumping efficiency,

the temperature of the upper sign change can be reproduced. This would mean, that spin pumping and spin Seebeck effect depend on different parameters, for example that the SSE is related to the magnetization, while the spin pumping is linked to the angular momentum. These measurements could then yield a method to distinguish magnetic moment and angular momentum. However, there is not enough experimental data to confirm this hypothesis, especially since $T_{\mathrm{comp,\,M}}$ and $T_{\mathrm{comp,\,L}}$ cannot be differentiated in our measurements in InYGdIG/Pt. There is also, until now, no theoretical explanation for the spin pumping behaviour. Therefore further investigations, for example in a material, where $T_{\mathrm{comp,\,M}}$ and $T_{\mathrm{comp,\,L}}$ are further apart will be necessary (see Sect. 6.2).

The last step in our analysis concentrates on the resonant antisymmetric signal attributed to microwave rectification. The rectification efficiency $D \cdot \mu_0 \Delta H$ (see Sect. 1.3), extracted separately for up and down sweep (red and black respectively), is shown as a function of temperature in Fig. 4.18 d). Starting at room temperature the signal is approximately constant at about -20×10^{-9} V T until $T_{\mathrm{cryo}} = 130\,\mathrm{K}$ and then starts to decrease until disappearing between $T_{\mathrm{cryo}} = 80\,\mathrm{K}$ and 60 K similar to the spin pumping signal. Below $T_{\mathrm{cryo}} = 60\,\mathrm{K}$, the up and down sweep values do not match perfectly due to a larger signal to noise ratio, but the signal value increases to very low temperatures.

The high temperature rectification efficiency is approximately the same as the -20×10^{-9} V T found in YIG/Pt (see Sect. 4.2.1.3), which is consistent with the assumption that the InYGdIG/Pt sample behaves like YIG/Pt as long as we are far away from the compensation region. This also justifies the fact that we used $D \cdot \mu_0 \Delta H$ as a rectification efficiency, since the efficiency is the same in both the InYGdIG/Pt and the YIG/Pt sample, even though the actual rectification amplitude D is different.

In contrast to the spin pumping amplitude L, D does not change sign at $T_{\mathrm{cryo}} = 100\,\mathrm{K}$, but seems to go to 0 between $T_{\mathrm{cryo}} = 60\,\mathrm{K}$ and 80 K. This corresponds to the temperature range around $T_{\mathrm{comp,\,M}}$, where the magnetization reaches a minimum. Since the rectification probably originates in the spin Hall magnetoresistance (SMR), further SMR measurements in this sample might help to understand the decrease of the rectification voltage around $T_{\mathrm{comp,\,M}}$. Such experiments will be discussed in Sect. 5.2.2.

In this section we have discussed the measurements of the resonant and non resonant dc voltage in an InYGdIG/Pt bilayer with a magnetization compensation temperature of 85 K. We observe two sign changes in the SSE voltage, one being attributed to the abrupt switching of the sublattice magnetizations at $T_{\mathrm{comp,\,M}}$. The origin of the second sign change at $T < T_{\mathrm{comp,\,M}}$ cannot yet be determined with certainty, but one possible explanation is that the sublattices contribute with different efficiencies to the SSE. In addition to this, we found a strong decrease of the ferromagnetic resonance field around the compensation temperature, originating in the divergence of the effective gyromagnetic ratio at $T_{\mathrm{comp,\,L}}$ and the divergence of the crystalline anisotropy field at $T_{\mathrm{comp,\,M}}$. The

latter also leads to a divergence of the coercive field at $T_{\mathrm{comp,\,M}}$. The divergence of the FMR linewidth can be attributed to the anisotropy effects at $T_{\mathrm{comp,\,M}}$ as well, or to the divergence of the effective damping constant α_{eff}. However, in order to confirm either explanation further investigations will be necessary.

The analysis of the voltage induced by FMR in InYGdIG/Pt yields similar spin pumping and rectification efficiencies for high temperatures, i.e. far away from $T_{\mathrm{comp,\,M}}$, as for YIG/Pt. The InYGdIG/Pt however behaves differently near the compensation region, since we observed two sign changes in the spin pumping voltage, one around $T_{\mathrm{comp,\,M}}$ and the other one at $T > T_{\mathrm{comp,\,M}}$. This kind of sign change in the spin pumping signal in a compensated garnet has never been observed to date and could be attributed to the fact that the Gd sublattice contributes with a higher efficiency to spin pumping than the Fe sublattices. This hypothesis however, has to be confirmed by further measurements and a theoretical model.

4.2.3 Temperature dependent FMR, spin pumping and spin Seebeck effect measurements in GdIG/Pt

We will now turn to the discussion of FMR, spin pumping and spin Seebeck effect measurements in the second magnetically compensated sample, i.e. the pure GdIG/Pt sample, in order to compare it with the results in InYGdIG/Pt.

4.2.3.1 Saturation magnetization of GdIG/Pt

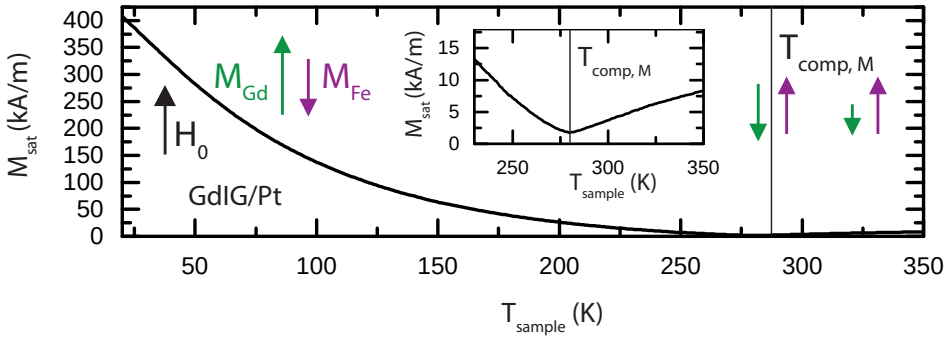

Figure 4.19: Saturation magnetization in GdIG/Pt obtained from SQUID magnetometry as a function of the sample temperature in an external magnetic field of 1 T (black arrow). The black line indicates the magnetization compensation temperature at $T_{\mathrm{sample}} = 279\,\mathrm{K}$. The purple and green arrows show the direction of the magnetization of the net Fe and Gd sublattices respectively. The inset shows a close up around the magnetization compensation temperature $T_{\mathrm{comp,\,M}} = 279\,\mathrm{K}$.

We first look at the saturation magnetization as a function of temperature of the

GdIG/Pt sample, as shown in Fig. 4.19. This curve was obtained by SQUID magnetometry in an external magnetic field of $\mu_0 H_0 = 1\,\mathrm{T}$ applied in the sample plane. The minimum of M_{sat}, i.e. the magnetization compensation temperature, is indicated by a black line at $T_{\mathrm{comp,\,M}} = 279\,\mathrm{K}$, which is consistent with literature values ranging from $T_{\mathrm{comp,\,M}} = 280\,\mathrm{K}$ to $296\,\mathrm{K}$ [23, 77, 79, 80] and in the same region as $T_{\mathrm{comp,\,M}} = 291\,\mathrm{K}$ from the magnetization calculation in GdIG presented in Sect. 3.1. The magnetization directions of the net Fe and Gd sublattices in an external magnetic field are represented by purple and green arrows respectively. The total magnetization of the GdIG/Pt film at low temperatures is larger by about a factor of 2 than in the doped InYGdIG/Pt. This is to be expected since in InYGdIG the Gd is diluted, which reduces the magnetization of the Gd sublattice [23] so that the low temperature increase of M_{sat} is weaker. The inset in Fig. 4.19 is a close up of the region around the magnetization compensation temperature.

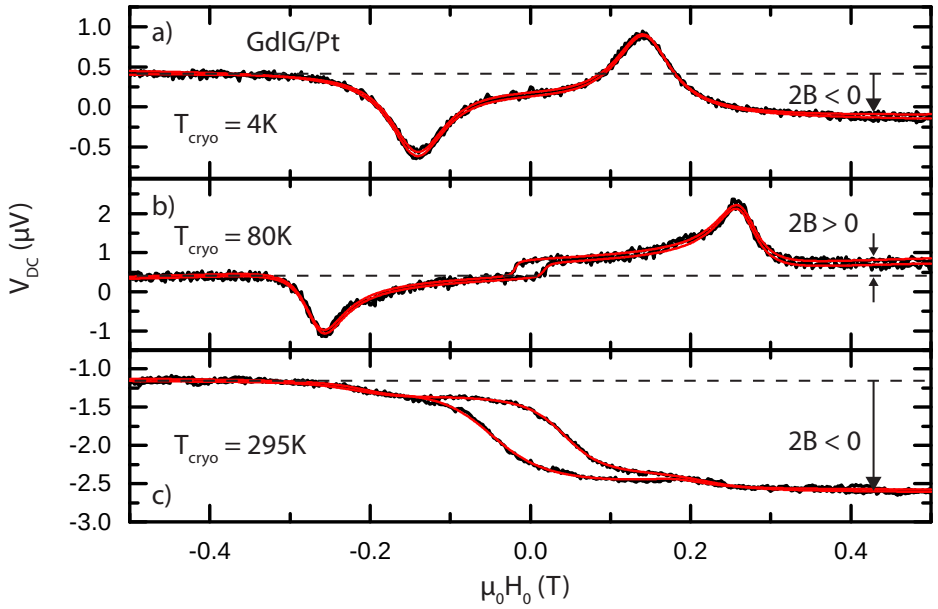

Figure 4.20: DC voltage as a function of the in plane external magnetic field in GdIG/Pt at $T_{\mathrm{cryo}} = 4\,\mathrm{K}$ (a), $T_{\mathrm{cryo}} = 80\,\mathrm{K}$ (b) and $T_{\mathrm{cryo}} = 295\,\mathrm{K}$ (c). The magnetic field upsweep is represented by a red line and the downsweep by a black line. For each temperature, the SSE amplitude $2B$ is indicated by a black arrow.

The same FMR, spin pumping and spin Seebeck measurements as in YIG/Pt and InYGdIG/Pt were conducted in the GdIG/Pt sample as a function of temperature from $T_{\mathrm{cryo}} = 5\,\mathrm{K}$ to $T_{\mathrm{cryo}} = 295\,\mathrm{K}$.

The dc voltage measurements at $T_{\mathrm{cryo}} = 4\,\mathrm{K}$, $T_{\mathrm{cryo}} = 80\,\mathrm{K}$ and $T_{\mathrm{cryo}} = 295\,\mathrm{K}$ are shown in Fig. 4.20 as a black line. The dc voltage is a superposition of different contributions from spin pumping, spin Seebeck effect and microwave rectification $V_{\mathrm{DC}} = V_{\mathrm{SSE}} + V_{\mathrm{SP}} + V_{\mathrm{rect}}$ (see Sect. 1.4) and yields a pronounced temperature dependence. At room temperature for

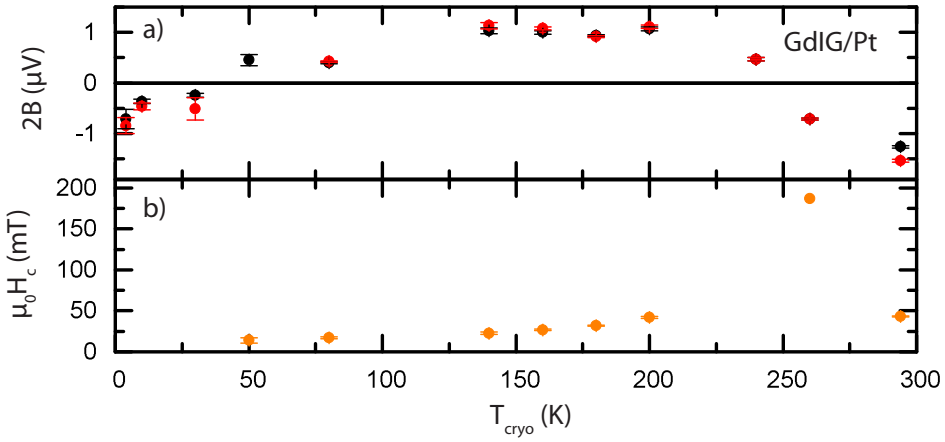

Figure 4.21: SSE amplitude $2B$ (a) and coercive field $\mu_0 H_c$ (b) in GdIG/Pt as a function of the cryostat temperature extracted from the dc voltage. The error bars represent the standard deviations from the fit function (1.26).

example, the resonant voltage nearly vanishes and the coercive field of the SSE hysteresis becomes quite large, while at lower temperatures a resonant voltage is clearly visible and the coercive field is not discernible anymore. Furthermore, there are two sign changes in the spin Seebeck voltage, which is consistent with other measurements in GdIG/Pt thin films [80] and the observations in InYGdIG/Pt described in Sect. 4.2.2.2. We will in the following discuss these effects in more detail as a function of temperature. All voltage measurements were fitted using Eq. (1.26), represented by a red line in Fig. 4.20, in order to extract the same parameters (H_{res}, ΔH, L, D, B) as for the YIG/Pt reference sample in Sect. 4.2.1 and the InYGdIG/Pt sample in Sect. 4.2.2.

4.2.3.2 SSE and coercive field

We again start with the analysis of the spin Seebeck amplitude $2B$ in GdIG/Pt, extracted using Eq. (1.26) as shown in Fig. 4.21 a) as a function of the cryostat temperature. The SSE voltage is negative at high temperatures similar to the YIG/Pt reference sample (see Sect. 4.8) and the InYGdIG/Pt sample (see Fig. 4.13), which were mounted in the same configuration (see Sect. 4.1.2), indicating that GdIG/Pt behaves like YIG/Pt at high temperatures. A first sign change takes place at approximately $T_{\mathrm{cryo}} = 250\,\mathrm{K}$, so that the SSE voltage is positive. At approximately $T_{\mathrm{cryo}} = 75\,\mathrm{K}$ the voltage becomes negative again, yielding a second sign change. This double sign change of the SSE voltage was previously observed in GdIG/Pt by Geprägs et al. [80] and is consistent with the SSE sign changes in InYGdIG/Pt presented in Sect. 4.2.2.2.

We attribute the high temperature sign change to the magnetization compensation point [90] at $T_{\mathrm{sample}} = 279\,\mathrm{K}$ determined from SQUID magnetometry. The sample temperature deviates from the cryostat temperature due to microwave heating and therefore

the scale in Fig. 4.21 needs to be corrected (see Sect. 4.1.4). Using the calibration from the InYGdIG/Pt sample, the upper sign change would take place at $T_{\mathrm{sample}} = T_{\mathrm{cryo}} + 18\,\mathrm{K}$ $= 268\,\mathrm{K}$, which is still lower than $T_{\mathrm{comp,\,M}}$ in GdIG/Pt. This calibration however is based on measurements in InYGdIG/Pt at a different temperature, and a larger temperature deviation in GdIG/Pt possible. We therefore use the correlation between SSE high temperature sign change and magnetization compensation temperature to deduce a deviation of 29 K between T_{sample} and T_{cryo} in the compensation region in this GdIG/Pt sample.

In order to explain the second sign change at $T_{\mathrm{cryo}} = 75\,\mathrm{K}$ we can apply the principle described in Sect. 4.2.2.1 and assume that the three sublattice magnetizations in GdIG contribute with different efficiencies to the SSE voltage. The experimental data can be reproduced when assuming a Gd efficiency $\eta = 0.4$

$$V_{\mathrm{SSE,\,total}} = \sum_i V_{\mathrm{SSE,\,M}_i} = c' \cdot (M_{d,Fe} - M_{a,Fe} - \eta M_{c,Gd}) \tag{4.5}$$

with $V_{\mathrm{SSE,\,M}_{d,Fe}} = c' M_{d,Fe}$, $V_{\mathrm{SSE,\,M}_{a,Fe}} = c' M_{a,Fe}$ and $V_{\mathrm{SSE,\,M}_{c,Gd}} = c'\ \eta M_{c,Gd}$. The sublattice magnetizations M_i are the ones obtained from the mean field calculation presented in Sect. 3.1. The scaling factor $c' = 1 \times 10^{-10}\ \mathrm{V\,m\,A^{-1}}$ was introduced to convert the magnetization into a voltage of the same order of magnitude as the one observed in the experiment. The factor c' found for GdIG/Pt is of the same order of magnitude as $c = 1.8 \times 10^{-10}\mathrm{V\,m\,A^{-1}}$ used for InYGdIG/Pt as discussed in Sect. 4.2.2.2. Figure 4.22 a) shows the SSE voltage contributions from the net Fe sublattice and the Gd sublattice, which cross at a sample temperature of 85 K. The experimentally obtained SSE voltage is depicted as black and red dots in Fig. 4.22 b), with a temperature scale corrected by 41 K (29 K to match the magnetization compensation point from the SQUID data and additionally 12 K to match the simulation as discussed in Sect. 4.2.3.1). The result of the simulation for the efficiencies in Eq. (4.5) (red line) nicely reproduces the experimental data. The $\eta = 0.4$ used here is smaller than the efficiency $\eta = 0.75$ found for the InYGdIG/Pt sample, but still in the same order of magnitude. The different efficiencies could be due to differing sample and/or interface quality. Furthermore, the composition of the samples and g factors are not precisely known, leading to an uncertainty in the simulated sublattice magnetizations. This could also influence the value of η derived from the simulation.

We now proceed to the analysis of the coercive field in GdIG/Pt, as shown in Fig. 4.21 b) as a function of cryostat temperature. The coercive field strongly increases around $T_{\mathrm{cryo}} = 250\,\mathrm{K}$, which corresponds to the magnetization compensation temperature. This is consistent with observations in InYGdIG/Pt, where the increase of the coercive field is attributed to an increase of the anisotropy field proportional to K/M at $T_{\mathrm{comp,\,M}}$ (see Sect. 4.2.2.2).

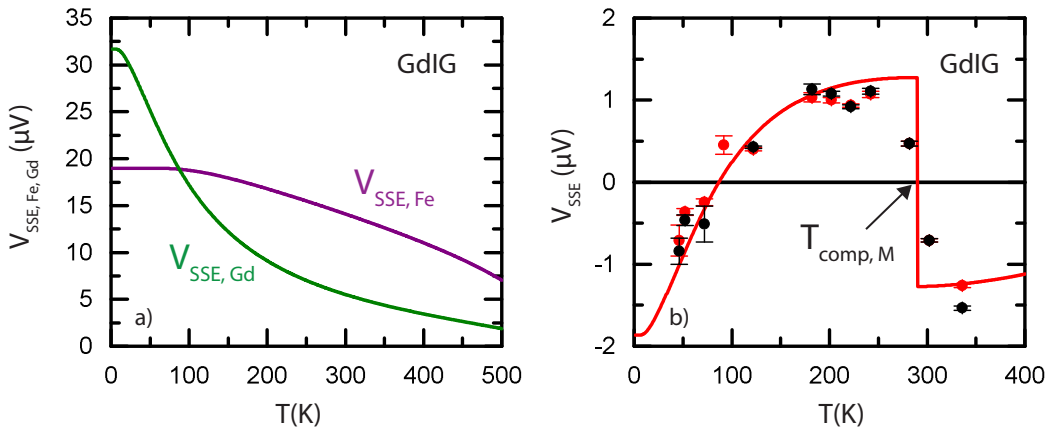

Figure 4.22: a) Simulation of the SSE contributions from the net Fe sublattice (purple) and the Gd sublattice (green) in GdIG as a function of sample temperature. b) The black and red dots represent the SSE voltage extracted from experiments, the red line is the total SSE voltage obtained from the simulation assuming that the sublattices contribute with different efficiencies.

4.2.3.3 Resonance field

We now turn to the ferromagnetic resonance position, which can be deduced from FMR experiments and simultaneously from the spin pumping voltage as a function of cryostat temperature. One supplementary measurement was conducted at a temperature exceeding the cryostat range by applying a dc current to the Pt layer for additional heating. As discussed in Sect. 4.1.4, a precise temperature calibration is very challenging in this case and we estimate the temperature in this measurement to $T_{\mathrm{sample}} \geq 303\,\mathrm{K}$. The goal here was only to heat the sample enough to achieve a temperature well above T_{comp}, and therefore this calibration is sufficient for now.

While heating the sample with a dc current of a few mA, i.e. applying a voltage of a few volts, a dc current of the order of µV is not detectable in this setup, so that there is no spin pumping and spin Seebeck data available above $T_{\mathrm{cryo}} = 295\,\mathrm{K}$. However, FMR measurements through microwave absorption were not affected by the heating current, so that the FMR position and linewidth could still be determined.

We have discussed previously (see Sect. 4.2.1.1 and 4.2.2.3) that the spin pumping voltage is less affected by temperature drift and noise and therefore yields better data quality. However, for high temperatures exceeding the range of the cryostat, only FMR measurements are available and we will therefore show the resonance field obtained from both FMR and spin pumping. The results are shown in Fig. 4.23 as a function of the cryostat temperature: the blue dots represent the data extracted from FMR using Eq. (1.4), while the red and black dots show the resonance field extracted from the spin pumping

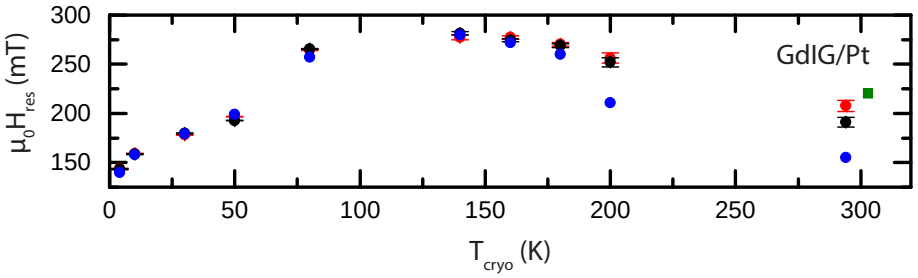

Figure 4.23: Resonance position extracted from FMR measurements (blue dots) and spin pumping voltage (red dots for magnetic field upsweep, black dots for downsweep) as a function of temperature in GdIG/Pt. The green square at 303 K was obtained from an FMR measurement using a dc current to heat the sample.

voltage using Eq. (1.26) from the magnetic field up and downsweep respectively. All three values coincide well over the whole temperature range except for $T_{\mathrm{cryo}} = 200\,\mathrm{K}$ and $T_{\mathrm{cryo}} = 295\,\mathrm{K}$. This deviation might have different origins: as discussed in Sect. 4.2.1 for the YIG/Pt sample, the FMR is more affected by temperature drift, which might distort the resonance, especially for broad lines. We will see that the linewidth in GdIG/Pt is very large around the compensation temperature, so that in this temperature range the determination of the resonance field is less precise and a determination of the experimental errors is challenging. On the other hand, the spin pumping at $T_{\mathrm{cryo}} = 295\,\mathrm{K}$ has practically vanished and the resonance field is very close to the coercive field (see Fig. 4.20 c)), so that the spin pumping overlaps with the slope of the spin Seebeck hysteresis near $\mu_0 H_{\mathrm{c}}$. A fit to this data with Eq. (1.26) might then yield less precise results than for a measurement, where all voltage contributions are clearly discernible.

The green square plotted above 300 K in Fig. 4.23 was extracted from the one FMR measurement, where a dc current was applied to the Pt layer in order to heat the sample above room temperature.

We find a decrease of $\mu_0 H_{\mathrm{res}}$ between $T_{\mathrm{cryo}} = 200\,\mathrm{K}$ and $T_{\mathrm{cryo}} = 303\,\mathrm{K}$ and below $T_{\mathrm{cryo}} = 80\,\mathrm{K}$. The magnetization compensation temperature in GdIG/Pt determined from the SSE voltage is at $T_{\mathrm{cryo}} = 250\,\mathrm{K}$ (see Fig. 4.21). Similar to the InYGdIG/Pt sample, we expect a drop in resonance field around $T_{\mathrm{comp,\,M}}$ and $T_{\mathrm{comp,\,L}}$. From a calculation of γ_{eff} based on the sublattice magnetizations (see Fig. 3.2 c)) we find that $T_{\mathrm{comp,\,M}}$ and $T_{\mathrm{comp,\,L}}$ are 4 K apart, so that the angular momentum compensation temperature is within the region where the FMR and spin pumping signals cannot be analyzed due to the very large linewidth in this temperature region.

The simulation of the resonance field described in Sect. 3.3 and used for InYGdIG/Pt (see Sect. 4.2.2.3) can also be applied to GdIG/Pt. The result is shown in Fig. 4.24 as a red line, as well as the resonance field from the experimental data extracted from spin

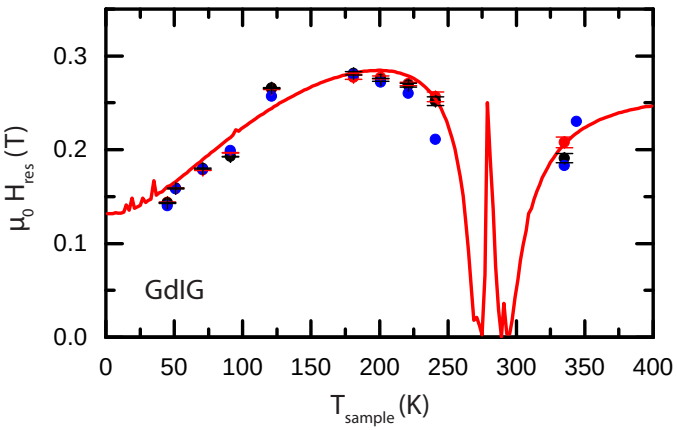

Figure 4.24: The black dots represent the resonance field extracted from the spin pumping voltage and FMR measurements, with a temperature scale corrected to $T_{\text{sample}} = T_{\text{cryo}} + 41\,\text{K}$ in order to match the compensation temperature of the calculation. The red line is the result of the resonance field simulation presented in Sect. 3. The sharp peaks in the compensation region are numerical artifacts due to the fact that the resonance field cannot be negative.

pumping and FMR (black, red and blue dots). The calculation reproduces the drop in resonance field in the compensation region. The sharp peaks around the compensation point are numerical artifacts, since the resonance field cannot become negative.

Our results are also consistent with the drop in resonance field in GdIG in the compensation region as observed in other GdIG samples [78, 79].

In contrast to InYGdIG/Pt, the resonance field at $T \leq 80\,\text{K}$ in GdIG/Pt decreases by a factor of 2, down to 150 mT at 5 K. This behaviour can be attributed to the shape anisotropy, which is proportional to the saturation magnetization (see Sect. 1.1.2 and 4.2.1). M_{sat} is smaller in the InYGdIG/Pt sample, leading to a smaller shape anisotropy and a less pronounced decrease of $\mu_0 H_{\text{res}}$. The strong decrease of $\mu_0 H_{\text{res}}$ to low temperatures is also quantitatively reproduced by the simulation.

4.2.3.4 FMR linewidth

The FMR linewidth was also extracted as a function of temperature as shown in Fig. 4.25, where the linewidth obtained from FMR measurements using Eq. 1.4 is represented by blue dots and the one obtained from the dc voltage using Eq. 1.26 by red and black dots for magnetic up and down sweep, respectively. The FMR linewidth from the measurement conducted with a heating dc current is shown as a green square.

Except for the measurement at room temperature, where the resonance nearly vanishes, the results from both FMR and spin pumping coincide very well. We find that the linewidth increases in the temperature region between $T_{\text{cryo}} = 170\,\text{K}$ and $T_{\text{cryo}} = 303\,\text{K}$, i.e. around the compensation temperature, which is consistent with the divergence of

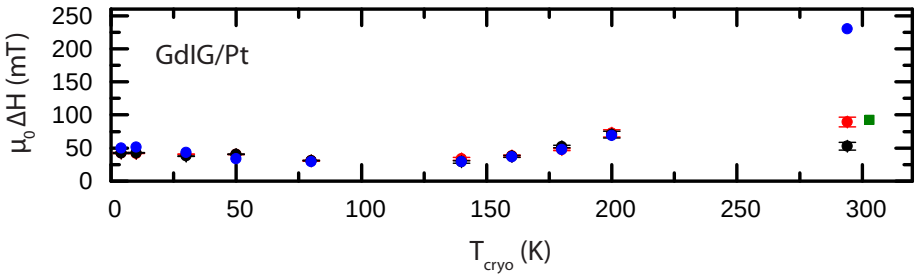

Figure 4.25: Temperature dependence of the linewidth extracted from FMR (blue dots) and spin pumping voltage (red and black dots for magnetic field up and down sweep) in GdIG/Pt. The linewidth extracted from the measurement above 300 K is represented by a green square.

linewidth at T_{comp} observed in other GdIG samples [77, 79] and in InYGdIG/Pt (see Sect. 4.2.2.4).

The results shown in Fig. 4.23 and 4.25 justify our choice to focus on InYGdIG/Pt, since the compensation region in our GdIG/Pt sample stretches over a range of about 100 K, but only over 50 K in InYGdIG/Pt. The expected divergence of linewidth and drop in resonance field are only visible to some extent in GdIG/Pt, while they are very pronounced in InYGdIG/Pt due to the smaller overall FMR linewidth.

4.2.3.5 Resonant voltage $V_{\mathrm{res}} = V_{\mathrm{SP}} + V_{\mathrm{rect}}$

We now turn to the analysis of the voltage in resonance $V_{\mathrm{res}} = V_{\mathrm{SP}} + V_{\mathrm{rect}}$ in GdIG/Pt, i.e. a superposition of a symmetric signal attributed to spin pumping and an antisymmetric signal attributed to microwave rectification. The spin pumping amplitude L was extracted from the dc voltage as a function of the cryostat temperature using Eq. (1.26) as shown in Fig. 4.26 a), where the red dots represent the results from the magnetic field upsweep, the black dots those from the downsweep and the error bars show the standard deviations from the fit. L is positive and therefore has the same sign as in YIG/Pt (see Fig. 4.7) and in InYGdIG/Pt at room temperature (see Fig. 4.18), which is to be expected since all three samples were mounted in the same configuration (see Fig. 4.1). At room temperature, i.e. in the compensation region, L is very small and the resonant voltage vanishes. Below $T_{\mathrm{cryo}} = 200\,\mathrm{K}$, the spin pumping amplitude increases to lower temperatures reaching a maximum of $1.3\,\mu\mathrm{V}$ around $T_{\mathrm{cryo}} = 80\,\mathrm{K}$ and then decreases again slightly. This behaviour is consistent with observations in the InYGdIG/Pt sample, where the spin pumping voltage also decreases when approaching the compensation temperature. However, in the InYGdIG/Pt sample, L changes sign at a temperature 30 K above $T_{\mathrm{comp,\,M}}$, but no such sign change is visible in GdIG/Pt. We have seen that the compensation region in InYGdIG/Pt is narrower and the FMR linewidth smaller than in GdIG/Pt, so that measurements near T_{comp} still yield good results. In the GdIG/Pt sample, we might simply

not be able to see this sign change, because the spin pumping cannot be detected in a narrow enough temperature region around T_{comp}.

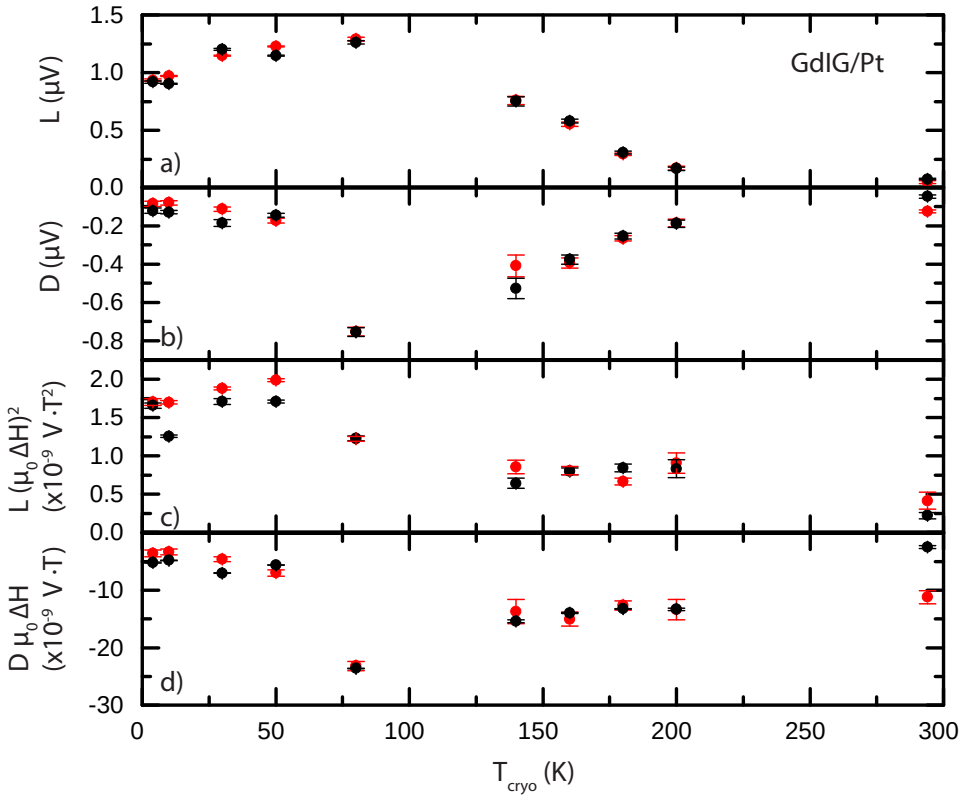

Figure 4.26: a) Amplitude L of the spin pumping voltage and b) amplitude D of the microwave rectification in GdIG/Pt as a function of the cryostat temperature. Panel c) shows the spin pumping efficiency $L(\mu_0\Delta H)^2$ and panel d) the rectification efficiency $D\mu_0\Delta H$ as a function of the cryostat temperature. The red and black dots represent the results obtained from the magnetic field up and down sweep respectively.

The amplitude D of the antisymmetric microwave rectification signal was also extracted from the dc voltage as a function the cryostat temperature using Eq. (1.26), as shown in Fig. 4.26 b), where the results from the magnetic field upsweep are again represented by red dots and those from the downsweep by black dots. The amplitude D is negative over the whole temperature range, so that L and D have opposite sign, similar to the YIG/Pt and InYGdIG/Pt sample. The rectification amplitude is small around the compensation point where the resonant voltage vanishes and increases to lower temperatures until reaching a maximum of 0.75 µV at $T_{\mathrm{cryo}} = 80\,\mathrm{K}$. Below $T_{\mathrm{cryo}} = 50\,\mathrm{K}$, D decreases again below 0.2 µV. The data point at $T_{\mathrm{cryo}} = 80\,\mathrm{K}$ seems to deviate from the data at other temperatures, and further measurements would be necessary to determine whether this point is an outlier due to a slightly different sample orientation or if there actually is a

pronounced maximum in rectification at $T_{\mathrm{cryo}} = 80\,\mathrm{K}$.

We now address the spin pumping efficiency $L(\mu_0\Delta H)^2$ in GdIG/Pt, as discussed in Sect. 1.2.3, in order to exclude the pronounced temperature dependence of the linewidth, as shown in Fig. 4.26 c). In InYGdIG/Pt the spin pumping efficiency is constant over the whole temperature range except for the compensation region. In GdIG/Pt, $L(\mu_0\Delta H)^2$ is constant between $T_{\mathrm{cryo}} = 140\,\mathrm{K}$ and room temperature, but the low temperature behaviour deviates from the expectation since the efficiency increases again. This might be due to the fact that the sample was removed after conducting the measurements between $T_{\mathrm{cryo}} = 80\,\mathrm{K}$ and room temperature and placed back into the resonator for the low temperature experiments. It is therefore possible that the orientation of the sample was slightly changed during this procedure, leading to deviations of the signal amplitude.

However, the spin pumping efficiency is of the order of $1 \times 10^{-9}\ \mathrm{V\,T^2}$, which is the same order of magnitude as in YIG/Pt (see Sect. 4.2.1.3) and InYGdIG/Pt far away from the compensation region (see Sect. 4.2.2.5). As long as only temperatures far away from the compensation temperature are considered, the spin pumping efficiency is therefore quantitatively comparable in all three Iron Garnet samples studied in this thesis. The difference in the spin pumping voltages L is thus mainly due to the FMR linewidth. Remaining deviations between the spin pumping efficiencies in different samples can be attributed to the interface quality.

We finally discuss the microwave rectification efficiency $D\mu_0\Delta H$ shown in Fig. 4.26 d). The efficiency is constant at about $15 \times 10^{-9}\ \mathrm{V\,T}$ for $T \geq 140\,\mathrm{K}$, but there still is an outlier at $T_{\mathrm{cryo}} = 80\,\mathrm{K}$ and at low temperatures the signal decreases. This can again be attributed to a slight change of the sample orientation during the measurement, as discussed for the spin pumping efficiency.

Similar to the spin pumping efficiency, the overall efficiency of the microwave rectification is of the same order of magnitude as the value $15 \times 10^{-9}\ \mathrm{V\,T}$ for YIG/Pt (see Sect. 4.2.1.3) and in InYGdIG/Pt far away from $T_{\mathrm{comp,\,M}}$ (see Sect. 4.2.2.5).

In summary, the measurements in GdIG/Pt yield similar results to the ones in InYGdIG/Pt presented in Sect. 4.2.2. We observe two sign changes in the SSE voltage, the first one at $T_{\mathrm{comp,\,M}}$, where the sublattice magnetizations abruptly switch direction, and the second one at a lower temperature. Similar to the InYGdIG/Pt sample, the low temperature sign change can be explained by assuming different SSE efficiencies of the Fe and Gd sublattices. Even though the compensation region in GdIG/Pt is broader than in InYGdIG/Pt, the same drop in resonance field and the divergence of coercive field and FMR linewidth around the compensation temperature are observed. The efficiencies of spin pumping and microwave rectification are quantitatively comparable in GdIG/P, InYGdIG/Pt and YIG/Pt, at least for temperatures far away the compensation temper-

ature. However, we did not observe a sign change of the spin pumping amplitude near $T_{\mathrm{comp,\,M}}$, as it was the case for InYGdIG/Pt, but we attribute this to the fact that the compensation region is broad, so that measurements near $T_{\mathrm{comp,\,M}}$ could not be conducted.

Chapter 5

Transport measurements in InYGdIG/Pt

In this chapter, we discuss current induced spin Seebeck effect and spin Hall magnetoresistance measurements in InYGdIG/Pt as a function of temperature. We will start with a description of the experimental setup and then proceed to the analysis of the current induced SSE (iSSE) measurements and their comparison with the microwave heating induced SSE (mw-SSE) discussed in Sect. 4.2.2.2. We will then turn to the analysis of the spin Hall magnetoresistance (SMR) measurements and discuss them in comparison to the rectification voltage measured in Sect. 4.2.2.5.

5.1 Experimental setup

5.1.1 Magneto-transport measurements in a Hall bar mesa-geometry

For magneto-transport measurements, the InYGdIG/Pt sample is patterned into a Hall bar mesa-structure with dimensions $600 \times 80\,\mu m^2$, using optical lithography and Argon ion beam milling. Figure 5.1 shows a sketch of the contacted Hall bar structure.

For the SSE measurements, a temperature gradient between the Pt and the InYGdIG is generated by applying a dc current of $I_d = \pm 6\,mA$ along the Hall bar with a Keithley 2400 source meter. The transverse voltage V_t is measured between the blue contacts in Fig. 5.1 using a Keithley 2182 nanovoltmeter. Since the SSE originates in the thermal gradient induced by the dc current, $V_{iSSE} \propto I_d^2$ (see Sect. 1.2.2) and is independent of the current direction. There are however resistive effects, e.g. the spin Hall magnetoresistance [6], which are larger than the SSE voltage and depend on the current direction, Spin Seebeck and resistive effects can be discerned using the following equation [41]

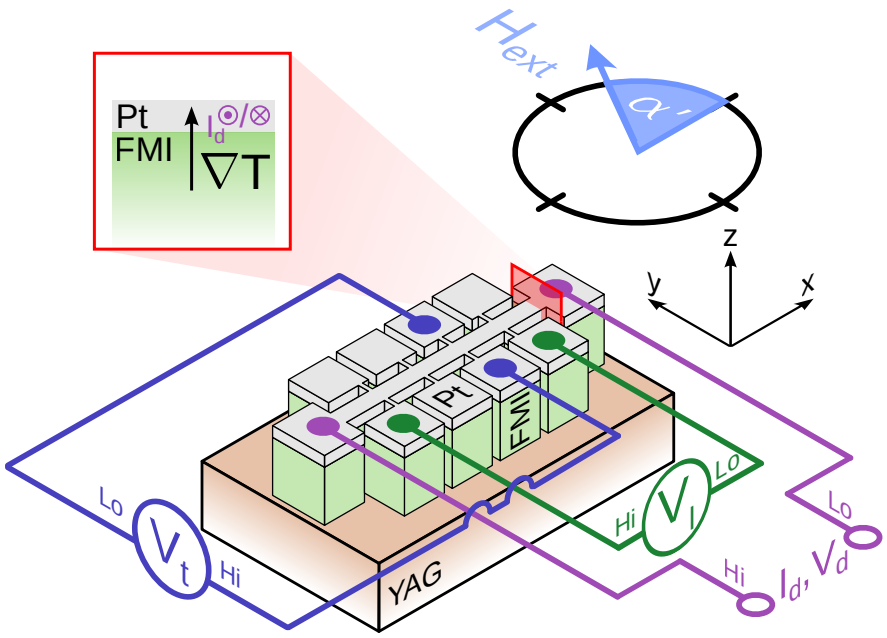

Figure 5.1: Sketch of the Hall bar structure used for the current heating induced SSE experiments: the dc current I_d is applied between the purple contacts, the longitudinal V_l and transverse voltage V_t are measured between the green and blue contacts, respectively. An external magnetic field is applied in plane with an angle α' relative to the short side of the sample. [41] FMI in this case is the InYGdIG layer.

$$\begin{aligned} V_\mathrm{t}(+I_\mathrm{d}) + V_\mathrm{t}(-I_\mathrm{d}) &= V_\mathrm{res}(+I_\mathrm{d}) + V_\mathrm{res}(-I_\mathrm{d}) + V_\mathrm{iSSE}(+I_\mathrm{d}) + V_\mathrm{iSSE}(-I_\mathrm{d}) \\ &= V_\mathrm{res}(+I_\mathrm{d}) - V_\mathrm{res}(+I_\mathrm{d}) + V_\mathrm{iSSE}(+I_\mathrm{d}) + V_\mathrm{iSSE}(+I_\mathrm{d}) \\ &= 2V_\mathrm{iSSE}(+I_\mathrm{d}) \end{aligned} \tag{5.1}$$

with $V_\mathrm{res}(+I_\mathrm{d}) = -V_\mathrm{res}(-I_\mathrm{d})$ the resistive voltage. The iSSE voltage is then obtained as [41]

$$V_\mathrm{iSSE} = \frac{V_t(I_\mathrm{d}) + V_t(-I_\mathrm{d})}{2} \tag{5.2}$$

In the setup depicted in Fig. 5.1, the SMR effect can be observed simultaneously to the iSSE by measuring the longitudinal voltage V_l between the green contacts using a second Keithley 2182 nanovoltmeter. The SMR effect being a resistive effect, it depends on the current direction, so that the longitudinal resistance we are interested in (see Sect. 1.2.4) is given by

$$R_\mathrm{long} = \frac{V_\mathrm{l,\,res}}{I_\mathrm{d}} = \frac{(V_l(I_\mathrm{d}) - V_l(-I_\mathrm{d}))/2}{I_\mathrm{d}} \tag{5.3}$$

Note that the SMR measurements do not require a heating current, and can be conducted using a much small current I_d. Using a dc 'heating' current I_d however allows for the simultaneous observation of SSE and SMR.

In order to conduct temperature dependent SSE and SMR effect measurements, the sample is inserted into a magnet cryostat, in which He exchange gas in a variable temperature insert (VTI) allows us to adjust the sample base temperature from 5 K to 300 K. A magnetic field is applied in the plane of the sample using a superconducting magnet. The magneto-thermo-galvanic voltages are then recorded as a function of the angle α' between the charge current direction and the applied magnetic field, as depicted in Fig. 5.1. In this magnet cryostat, external magnetic fields of up to 7 T are possible.

An in plane orientation for the positive magnetic field of $\alpha' = 180°$ in Fig. 5.1 corresponds to the positive field configuration in the microwave induced SSE experiments (see Sect. 4.1.2), so that at room temperature we expect a negative SSE voltage at $\alpha' = 180°$ [36] (see Sect. 1.2.2).

5.1.2 Temperature calibration

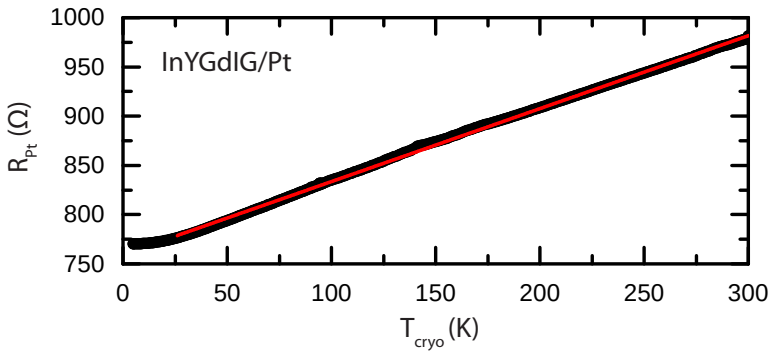

Figure 5.2: Calibration curve of the Pt resistance in InYGdIG/Pt as a function of VTI temperature without dc current heating.

The sample base temperature, corresponding to the VTI temperature T_{cryo} is measured by a Cernox sensor placed just below the sample. For all measurements in this setup, the sample is heated by a dc current of ±6 mA and therefore the sample temperature T_{sample} deviates from the base temperature T_{cryo}, so that a correction of T_{sample} is necessary. We make use of the fact that the Pt resistance has a linear temperature dependence and record a calibration curve, where the Pt resistance is measured as a function of cryostat temperature, as shown in Fig. 5.2 as black dots. For this measurement, a small dc current of 100 µA was applied along the Hall bar (which corresponds to a dissipated heat of the

order of 10 µW and is negligible) and we recorded the voltage between the green contacts in Fig. 5.1. The Pt resistance is linear with T in good approximation between 50 K and 300 K and from the fit (red line) we obtain $R(T_{\mathrm{cryo}}) = (759.5 \pm 0.2)\,\Omega + (0.74 \pm 0.001)\cdot T_{\mathrm{cryo}}\,\Omega/\mathrm{K}$, which corresponds to a temperature coefficient $\alpha = 0.0010\,\mathrm{K}^{-1}$. This is smaller than the value $\alpha_{\mathrm{bulk}} = 0.00392\mathrm{K}^{-1}$ [87] for bulk Pt but close to the value $\alpha = 0.0014\mathrm{K}^{-1}$ obtained for our YIG/Pt thin film (see Sect. 4.2.1.3). Below 50 K the resistance reaches a residual value due to impurities [92].

Since for each measurement conducted with a heating current, the longitudinal resistance is recorded, this value can be compared with the calibration curve shown in Fig. 5.2, in order to determine the actual sample temperature. Since we also observe a magnetoresistive effect, the sample resistance changes in magnetic field dependent measurements. This change however corresponds to a temperature change of the order of 1 K, so that the resistive thermometry method is still justified. The correction was applied to all measurements shown in the following section.

5.2 Experimental results

5.2.1 Current heating induced spin Seebeck effect

In analogy to the microwave heating induced SSE in InYGdIG/Pt as a function of temperature (see Sect. 4.2.2.2), we now analyze the results of the dc current heating induced SSE.

In plane magnetic field rotations in $\Delta\alpha' = 2°$ steps at $\mu_0 H_0 = 7\,\mathrm{T}$ were conducted in the InYGdIG/Pt sample as a function of temperature and the iSSE voltage was determined from V_t using Eq. (5.1). The in plane magnetic field orientation dependent iSSE voltages at $T_{\mathrm{sample}} = 21\,\mathrm{K}$, 59 K and 326 K are shown in Fig. 5.3 in black. According to Sect. 1.2.2, we expect a $\cos(\alpha)$ dependence with α the orientation of the magnetization. At $\mu_0 H_0 = 7\,\mathrm{T}$, in plane anisotropies can be neglected such that $\mathbf{M} \parallel \mathbf{H}_0$ in good approximation, and the SSE voltage indeed has a $\cos(\alpha')$ angle dependence, as shown by the cosine fit represented by a red line. The cosine is offset by a constant voltage, which is particularly pronounced at high temperatures (see Fig. 5.3 c)). This might be due to contributions from the longitudinal voltage caused by a slight misalignment of the transverse Hall bar contacts. These longitudinal voltage contributions increase with temperature as the Pt resistance increases and the offset is therefore more pronounced at high than at low temperatures.

At $T_{\mathrm{sample}} = 326\,\mathrm{K}$, the iSSE voltage at $\alpha' = -180°$ (magnetic field along the Hall bar) is negative, which is consistent with the expectations for this configuration and with the mw-SSE measurements in Sect. 4.2.2.2. There are two sign changes, since $V_{\mathrm{iSSE}}(\alpha' = -180°)$ is negative at $T_{\mathrm{sample}} = 59\,\mathrm{K}$ and positive again at $T_{\mathrm{sample}} = 21\,\mathrm{K}$. This behaviour is also consistent with our previous mw-SSE measurements in InYGdIG/Pt and the observations by Geprägs et al. [80] concerning iSSE in GdIG/Pt thin films as a function of temperature.

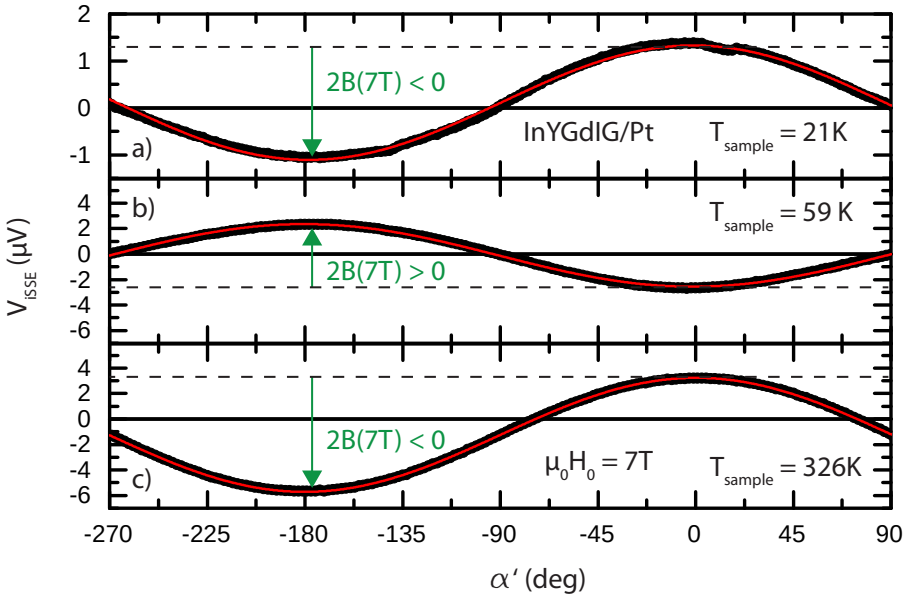

Figure 5.3: V_{iSSE} in InYGdIG/Pt as a function of the in plane magnetic field orientation at 7 T at $T_{\mathrm{sample}} = 21\,\mathrm{K}$, 59 K and 326 K. The experimental data is depicted in black and the red line represents the $\cos(\alpha')$ fit to the data.

The angle dependent measurements were repeated for various temperatures between $T_{\mathrm{sample}} = 21\,\mathrm{K}$ and 326 K and the spin Seebeck amplitude $2B(7\,\mathrm{T})$, corresponding to twice the cosine amplitude[1], was extracted as shown in Fig. 5.4 as black dots. We find a first sign change at $T_{\mathrm{sample}} = 80\,\mathrm{K}$ and the second one at 26 K. The SSE voltage extracted from the microwave heating induced SSE at $\mu_0 H_0 = 1\,\mathrm{T}$ is also shown as red dots as a function of the corrected sample temperature (see Sect. 4.1.4). The temperature dependence of both measurements is very similar, since they both yield two sign changes, the upper one being more abrupt and the lower one smoother. However, the temperatures at which the sign changes take place in the iSSE are about 10 K lower than in the mw-SSE. Since the upper sign change of the spin Seebeck effect is attributed to the magnetization compensation point which was determined by SQUID magnetometry to be at $T_{\mathrm{sample}} = 85\,\mathrm{K}$, both the temperature calibrations from iSSE and mw-SSE measurements deviate from the SQUID temperature scale. The deviation of the iSSE temperature scale can be explained by the fact that the calibration curve in Fig. 5.2 was recorded once at the beginning of the measurement series and used for all following measurements. Even though the heating current was held constant throughout all experiments, it seems that the heating power decreased over time, which might be due to a change of the Pt resistance, i.e. a

[1] $2B(7\,\mathrm{T}) = V_{\mathrm{SSE}}(7\,\mathrm{T}) - V_{\mathrm{SSE}}(-7\,\mathrm{T})$ similar to the SSE amplitude extracted in Sect. 4.2.2.2 using Eq. (1.26)

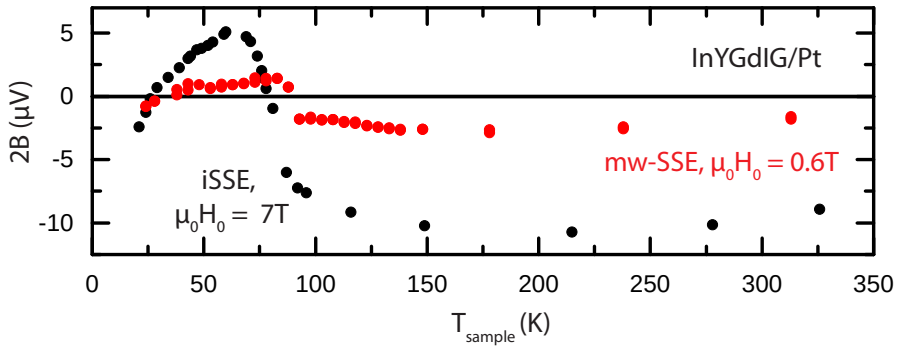

Figure 5.4: Amplitude $2B(7\,\mathrm{T})$ of the current heating induced SSE in InYGdIG/Pt extracted from magnetic field orientation dependent measurements as a function of the sample temperature (black dots). The red dots show the amplitude extracted from the microwave heating induced SSE at 1 T from Sect. 4.2.2.

deterioration of the Pt layer after numerous measurements using dc current heating [2].

It is also possible that the temperature of the SSE sign change depends on the external field, however such a behaviour of the magnetization compensation temperature was not observed in SQUID measurements in our thin films. Therefore further investigations, i.e. measurements at different magnetic field strengths in the same setup, as well as a more precise temperature calibration will be necessary in order to precisely compare the temperatures obtained in different setups.

Nevertheless, we have seen that two different SSE measurement methods (current heating and microwave heating) yield the same kind of temperature dependence of the SSE voltage, i.e. one sign change at $T_{\mathrm{comp,\,M}}$ and a second one at a lower temperature, which, as proposed in Sect. 4.2.2.2, can be attributed to different SSE efficiencies of the sublattices in InYGdIG/Pt.

Even though the temperature dependence resulting from both methods is similar, the absolute amplitude of the iSSE is about a factor 5 larger than the amplitude of the mw-SSE. According to Eq. (1.13), the SSE amplitude is proportional to the temperature difference between electrons in the Pt and magnons in the ferrimagnetic layer [18], i.e to the heating power [41]. Therefore in order to compare the SSE amplitudes obtained from different experimental methods, a comparison of the heating power is necessary. The heating power for the iSSE is known, since it corresponds to the Joule heating power of the dc current in the Pt layer. However, in the case of microwave heating the determination of the heating is challenging, since the exact electric field distribution at the sample position is not known.

[2] A similar deviation of the sign change from the SQUID $T_{\mathrm{comp,\,M}}$ was also observed in other samples measured in this setup.

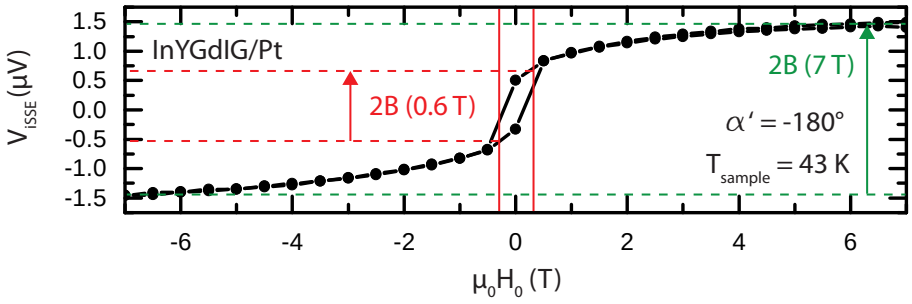

Figure 5.5: The black dots represent the iSSE voltage as a function of the external magnetic field $-7\,\mathrm{T} \leq \mu_0 H_0 \leq 7\,\mathrm{T}$ for $\alpha' = -180°$ at $T_{\mathrm{sample}} = 43\,\mathrm{K}$. The iSSE amplitude $2B(7\,\mathrm{T})$ is marked by a green arrow while the amplitude at zero magnetic field is marked in red.

Furthermore, we have to take into account that the mw-SSE measurements were conducted in a non patterned $1.9 \times 5\,\mathrm{mm}^2$ sample, while the iSSE experiments were conducted in a $600 \times 80\,\mu\mathrm{m}^2$ Hall bar geometry, so that the resistance and also the measured voltage in both cases are different.

In addition to the different heating powers and Pt resistances in both measurements, the SSE amplitude in InYGdIG/Pt strongly depends on the external magnetic field. This effect is illustrated by the magnetic field dependent iSSE measurement for $-7\,\mathrm{T} \leq \mu_0 H_0 \leq 7\,\mathrm{T}$ at $T_{\mathrm{sample}} = 43\,\mathrm{K}$ at $\alpha' = -180°$ shown in Fig. 5.5 as black dots, where the SSE amplitude increases to higher magnetic fields. The amplitude $2B(7\,\mathrm{T}) = V_{\mathrm{iSSE}}(7\,\mathrm{T}, \alpha' = -180°) - V_{\mathrm{iSSE}}(-7\,\mathrm{T}, \alpha' = -180°) = 2.93\,\mu\mathrm{V}$ marked by a green arrow in Fig. 5.5 is consistent with the amplitude $2B(7\,\mathrm{T}) = V_{\mathrm{iSSE}}(7\,\mathrm{T}, \alpha' = -180°) - V_{\mathrm{iSSE}}(7\,\mathrm{T}, \alpha' = 0°) = 2.96\,\mu\mathrm{V}$ in Fig. 5.4, which is expected since a magnetic field rotation by 180° is equivalent to a magnetic field inversion. The amplitude $2B(0.6\,\mathrm{T}) = 0.82\,\mu\mathrm{V}$ marked in red (0.6 T being the maximum external field applied in the mw-SSE experiments) is much smaller than the high field value. Therefore, the different amplitudes obtained from different experimental methods in Fig. 5.4 can also be partly explained by the strong field dependence of the SSE voltage.

The apparent increase of the SSE amplitude with magnetic field amplitude shown in Fig. 5.5 is linear only in a first approximation and cannot simply be described by the additional slope C as defined in Fig. 1.2. The origin of this strong magnetic field dependence is not known yet, but it seems that a very large magnetic field is necessary to saturate the InYGdIG. This might be caused by the paramagnetic behaviour of the Gd moments, but futher investigations will be necessary in the future in order to understand this behaviour.

5.2.2 Spin Hall magnetoresistance

We now proceed to the analysis of the longitudinal voltage in order to determine the temperature dependence of the spin Hall magnetoresistance in InYGdIG/Pt. The longitudinal resistance R_{long} as a function of the in plane magnetic field orientation α' obtained from V_l using Eq. 5.3 at $T_{\text{sample}} = 21\,\text{K}$, 81 K and 326 K in an external field of 7 T is shown in Fig. 5.6 (black).

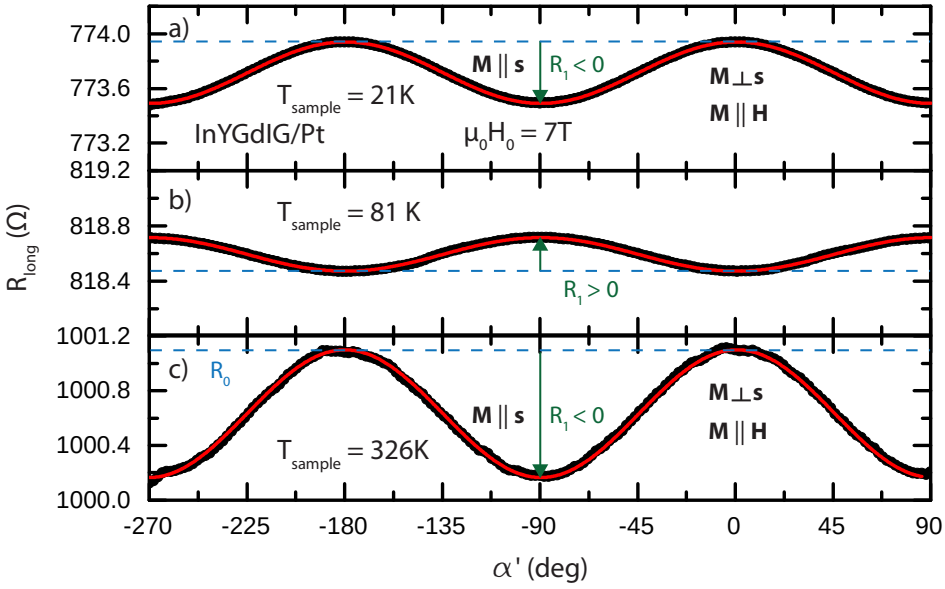

Figure 5.6: The longitudinal resistance R_{long} as a function of the in plane magnetic field orientation α' in InYGdIG/Pt for $\mu_0 H_0 = 7\,\text{T}$ at $T_{\text{sample}} = 21\,\text{K}$ (a), 81 K (b) and 326 K (c) is shown in black. The red line represents a $\cos^2(\alpha')$ fit to the experimental data. The blue dashed line represents the sample resistance R_0 at $\alpha' = 0°$ and the green arrow represents $R_1 = R_{\text{long}}(\alpha' = 90°) - R_{\text{long}}(\alpha' = 0°)$ as defined in Sect. 1.2.4.

We start with the analysis of the measurement at $T_{\text{sample}} = 326\,\text{K}$ shown in Fig. 5.6 c). The longitudinal resistance has a $\cos^2(\alpha')$ dependence on the in plane magnetic field orientation α' (fit function represented by the red line). From Eq. (1.20) we expect a $\cos^2(\alpha)$ dependence of R_{long} on the magnetization orientation α. We assume the individual sublattice magnetizations M_i to be collinear at this temperature far away from $T_{\text{comp, M}}$, where there is no spin canting at 7 T [53], so that $\mathbf{M}_i \parallel \mathbf{M}$ with $\mathbf{M}$ the net magnetization of the sample. The external magnetic field of 7 T applied in the sample plane is sufficient to overcome in plane magnetic anisotropies and align the net magnetization along the external magnetic field. Therefore $\mathbf{M} \parallel \mathbf{H}_0$ and $\alpha = \alpha'$ and our results are consistent with the expectations from the theoretical model in Sect. 1.2.4. At $\alpha' = 0°$ the magnetic field is oriented along the Hall bar, i.e. parallel to the current direction $\mathbf{j}$, so that $\mathbf{M} \perp \mathbf{s}$. The spin current can transfer angular momentum to the magnetization and the resistance reaches its maximum R_0 (dashed blue line in Fig. 5.6). For $\alpha' = 90°$, the magnetic field

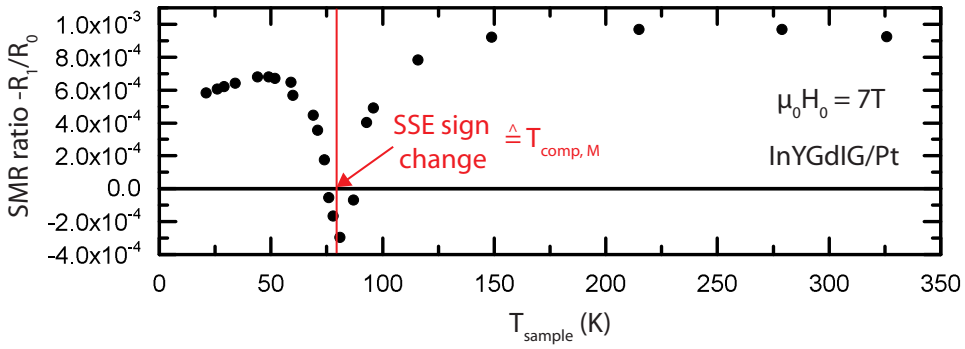

Figure 5.7: SMR ratio $-R_1/R_0$ [6] in InYGdIG/Pt at 7 T as a function of the sample temperature. The red line represents the upper sign change of the SSE attributed to the magnetization compensation temperature $T_{\mathrm{comp,\,M}}$.

is oriented across the Hall bar (see Fig. 5.1), i.e. perpendicular to the current direction $\mathbf{j}$, so that $\mathbf{M} \parallel \mathbf{s}$, with $\mathbf{s}$ the spin current polarization. In this configuration no angular momentum can be transferred to the magnetization and the resistance is at its minimum $R_0 + R_1$, with $R_1 = R_{\mathrm{long}}(\alpha' = 90°) - R_{\mathrm{long}}(\alpha' = 0°) < 0$, as illustrated by the green arrow in Fig. 5.6 c). This definition of R_1 [6] yields a negative magnetoresistance at $T_{\mathrm{sample}} = 326\,\mathrm{K}$. The SMR ratio is then given as $-R_1/R_0$ (see Eq. (1.22)), so that we obtain $-R_1/R_0(326\,\mathrm{K}) = 9.23 \times 10^{-4}$, which is consistent with SMR values obtained in YIG/Pt of comparable Pt thickness at room temperature [6, 8]. In terms of SMR, the InYGdIG/Pt therefore behaves like YIG/Pt at high temperatures.

For $T_{\mathrm{sample}} = 21\,\mathrm{K}$ (see Fig. 5.6 a)), the exact same angle dependence as for 326 K is observed, only the absolute resistance values are different, due to the temperature dependence of the Pt resistance. We obtain $-R_1/R_0(21\,\mathrm{K}) = 5.8 \times 10^{-4}$, which is also comparable to the value obtained in YIG/Pt of comparable Pt thickness at similar temperatures [8].

At $T_{\mathrm{sample}} = 81\,\mathrm{K}$, as shown in Fig. 5.6 b), however, the $\cos^2(\alpha')$ is shifted by 90°, so that the resistance minimum is at $\alpha' = 0°$ and the maximum at $\alpha' = 90°$. Extracting $R_1 = R_{\mathrm{long}}(\alpha' = 90°) - R_{\mathrm{long}}(\alpha' = 0°)$ then yields a positive sign for R_1 and we obtain $-R_1/R_0(81\,\mathrm{K}) = -2.96 \times 10^{-4}$. This sign change of the SMR ratio is due to the definition of R_1 and in fact only reflects the interchange of minimum and maximum resistance configuration, with respect to the external magnetic field orientation α', in comparison to measurements at $T_{\mathrm{sample}} = 326\,\mathrm{K}$ and $T_{\mathrm{sample}} = 21\,\mathrm{K}$. This indicates that for $T_{\mathrm{sample}} = 81\,\mathrm{K}$, at $\alpha' = 0°$, no (or less) angular momentum can be transferred, since the resistance reaches a minimum, even though the magnetic field is perpendicular to $\mathbf{s}$. Therefore it seems that the assumption $\mathbf{M}_i \parallel \mathbf{M} \parallel \mathbf{H}_0$ is no longer valid in this situation. This effect will be discussed in more detail in the following analysis.

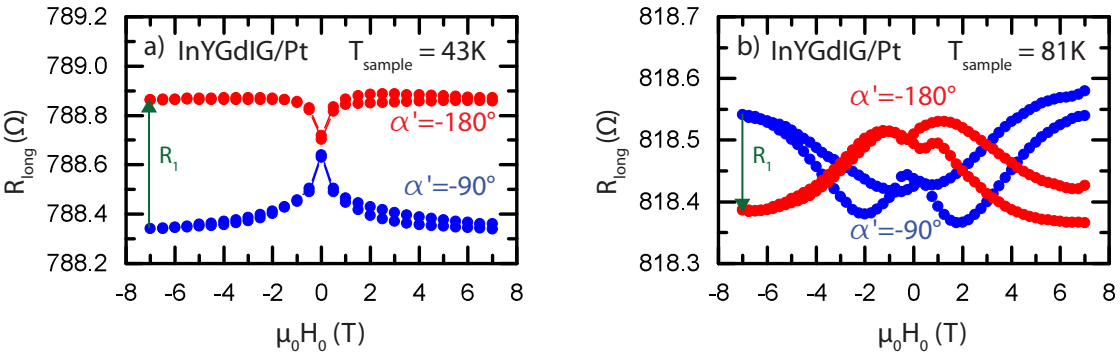

Figure 5.8: R_{long} as a function of magnetic field at 43 K (a) and 81 K (b) with the data for $\alpha = -180°$ represented in red and data for $\alpha = -90°$ in blue. The green arrow indicates the amplitude and sign of R_1.

The in plane angle dependent measurements were conducted at various temperatures between $T_{\text{sample}} = 21\,\text{K}$ and 326 K and the SMR amplitude extracted as described above from Eq. (1.22) is shown as black dots in Fig. 5.7. Starting at high temperatures, the SMR amplitude is approximately constant until $T_{\text{sample}} = 150\,\text{K}$ and then decreases strongly. The amplitude is negative between $T_{\text{sample}} = 75\,\text{K}$ and 87 K, increases again reaching a local maximum of 5.8×10^{-4} at 50 K and slightly decreases to low temperatures. The temperature region in which $-R_1/R_0$ is negative stretches from $T_{\text{sample}} = 76\,\text{K}$ to 87 K, i.e. around the temperature $T_{\text{sample}} = 81\,\text{K}$ where the upper sign change in the SSE voltage takes place (see Sect. 5.2.1). This SSE sign change is attributed to the magnetization compensation temperature $T_{\text{comp, M}}$ and is marked by a red line in Fig. 5.7.

Except for the pronounced drop of the SMR amplitude around $T_{\text{comp, M}}$, the overall behaviour, i.e. slight decrease to lower temperatures, is consistent with previous observations in YIG/Pt [8].

In order to better understand the decrease and "sign change" of the SMR amplitude around the magnetization compensation temperature, additional measurements as a function of magnetic field strength $\mu_0 H_0$ at two constant field orientations $\alpha' = -180°$ and $\alpha' = -90°$ were conducted at $T_{\text{sample}} = 81\,\text{K}$ and $T_{\text{sample}} = 43\,\text{K}$, i.e. at $T_{\text{comp, M}}$ and well below $T_{\text{comp, M}}$. The data is shown in Fig. 5.8 a) and b). In both panels the red dots represent R_{long} as a function of $\mu_0 H_0$ at $\alpha' = -180°$ and the blue ones the sweep at $\alpha' = -90°$.

We will first analyze the field sweeps at $T_{\text{sample}} = 43\,\text{K}$, i.e. far away from the compensation region. At $\mu_0 H_0 = \pm 7\,\text{T}$, $R_{\text{long}}(\alpha' = -180°) \geq R_{\text{long}}(\alpha' = -90°)$ which is consistent with the angle dependent measurements in Fig. 5.6. An illustration of the Fe (purple) and Gd (green) sublattice magnetization orientations in a magnetic field sweep from 7 T

to $-7\,\mathrm{T}$ with an in plane magnetic field orientation $\alpha' = -180°$ is shown in Fig. 5.9. We assume that both magnetizations are rigidly coupled and that the angle between them is always 180°, i.e. $\mathbf{M}_i \parallel \mathbf{M}$ with $\mathbf{M}$ the net magnetization. At $T < T_{\mathrm{comp,\,M}}$, the Gd sublattice magnetization dominates and is parallel to $\mu_0\mathbf{H}_0 = 7\,\mathrm{T}$. In this configuration $\mathbf{M} \perp \mathbf{s}$ and the longitudinal resistance is at its maximum R_{max} (see Fig. 5.9 a)). Upon a field sweep from positive to negative fields, the magnetization direction is not immediately changed by 180° but rather rotates in the sample plane (see Fig. 5.9 b)) (we here assume single domain/macrospin type behaviour, i.e, no magnetic domain formation but coherent rotation), so that the angle between $\mathbf{M}$ and spin polarization $\mathbf{s}$ is less than 90° and $R_{\mathrm{long}} < R_{\mathrm{max}}$ as expected from Fig. 5.6. With increasing negative field, all magnetic moments are again aligned with the external field and the resistance reaches the maximum value for $\alpha' = \alpha = -180°$ (Fig. 5.9 c)).

The illustration in Fig. 5.9 can also be applied for the sweep direction from negative to positive field. The drop in resistance takes place around the coercive field of the magnetic film, leading to a hysteretic behaviour in an up and down field sweep [6]. This hysteretic behaviour is however not visible in the 43 K measurement since the coercive field in InYGdIG/Pt at this temperature is of the order of $\mu_0 H_c = 30\,\mathrm{mT}$ (see Sect. 4.2.2.2), which is much smaller than the resolution of 500 mT of the field sweep in Fig. 5.8. Thus, only the dip from the magnetization orientation change owing to coherent rotation prevails.

The exact same considerations as in Fig. 5.9 can be applied to a magnetic field orientation of $\alpha' = -90°$ in order to reproduce the blue dots in Fig. 5.8 a). At high fields, the magnetization is again aligned with $\mu_0 H_0$, so that in this configuration $\mathbf{M} \parallel \mathbf{s}$ and the longitudinal resistance is at its minimum. During the magnetic field sweep from positive to negative field, the magnetization again does not change direction instantaneously but rotates, so that $\mathbf{M}$ is not parallel to the spin current polarization $\mathbf{s}$ anymore and angular momentum can be transferred, leading to an increase of R_{long}, as observed in Fig. 5.8 a).

We now turn to the magnetic field strength dependent measurement at $T_{\mathrm{sample}} = 81\,\mathrm{K}$, i.e. at the magnetization compensation point, shown in Fig. 5.8 b). At this temperature the field dependence of R_{long} is very different from the one observed in Fig. 5.8 a). At $\mu_0 H_0 = 7\,\mathrm{T}$, $R_{\mathrm{long}}(\alpha' = -180°) < R_{\mathrm{long}}(\alpha' = -90°)$ which is consistent with the angle dependent measurements in Fig. 5.6 b). For $-4\,\mathrm{T} \leq \mu_0 H_0 \leq 4\,\mathrm{T}$ however, $R_{\mathrm{long}}(\alpha' = -180°) > R_{\mathrm{long}}(\alpha' = -90°)$, as it was the case at $T_{\mathrm{sample}} = 43\,\mathrm{K}$, and we observe the expected hysteretic magnetoresistive behaviour. At this temperature the coercive field increases strongly (see Sect. 4.2.2.2) and a hysteretic behaviour is visible with the 250 mT magnetic field resolution. However, for both magnetic field orientations the magnetic field up and down sweep do not match, which might be caused by a slight temperature drift leading to different resistance values.

The strong dependence of R_{long} on the magnetic field strength at $T_{\mathrm{comp,\,M}}$ can be explained by the illustration in Fig. 5.10 for $\alpha' = -180°$. At $T_{\mathrm{comp,\,M}}$, the magnetizations

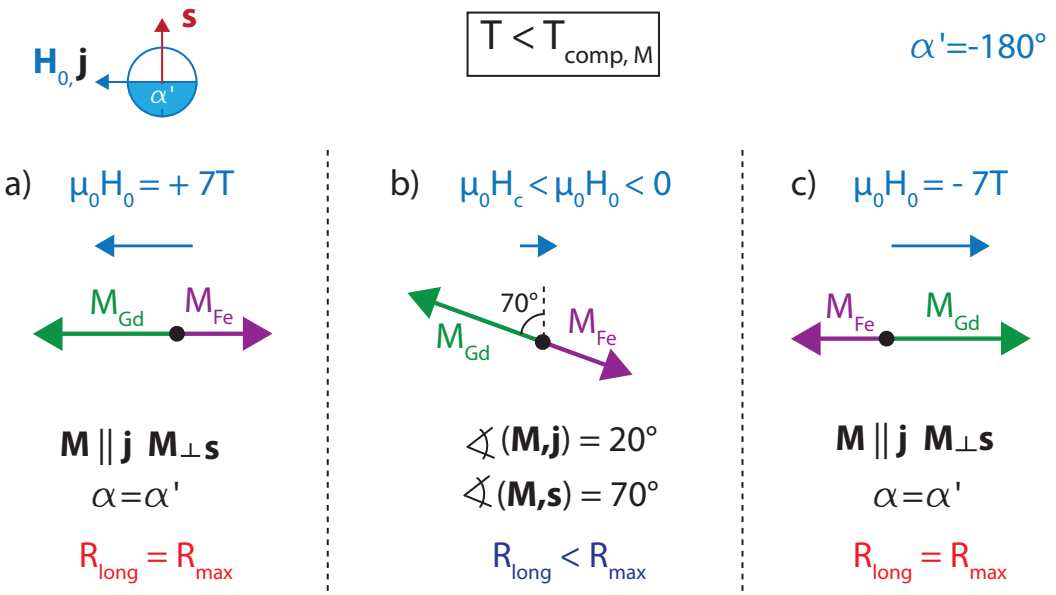

Figure 5.9: Illustration of the magnetization behaviour in InYGdIG/Pt in a magnetic field sweep at $T < T_{\mathrm{comp,\,M}}$. The net Fe and Gd sublattices are represented by purple and green arrows respectively. The dc current $\mathbf{j}$ and the magnetic field $\mu_0\mathbf{H}_0$ are applied along the Hall bar ($\alpha' = -180°$). a) A magnetic field of 7 T is applied, so that $\mathbf{M} \parallel \mathbf{H}_0 \parallel \mathbf{j}$ and $\mathbf{M}\perp\mathbf{s}$ and the R_{long} reaches its maximum. b) The magnetic field is negative but smaller than the coercive field, and not strong enough to completely reorient the magnetization. The angle between $\mathbf{M}$ and $\mathbf{s}$ is smaller than 90° and $R_{\mathrm{long}} < R_{\mathrm{max}}$. c) The strong −7 T magnetic field reorients the magnetization so that again $\mathbf{M} \parallel \mathbf{H}_0 \parallel \mathbf{j}$ and $\mathbf{M}\perp\mathbf{s}$ and $R_{\mathrm{long}} = R_{\mathrm{max}}$

of the net Fe and the Gd sublattices represented by purple and green arrows of the same length compensate each other. As discussed in Sect. 1.5, at $T_{\mathrm{comp,\,M}}$ the sublattice magnetizations $\mathbf{M}_i$ are all aligned with the external magnetic field as long as $\mu_0 H_0$ is weak [53]. This situation is represented in Fig. 5.10 b), where $\mathbf{M}_i \parallel \mathbf{M} \parallel \mathbf{H}_0 \parallel \mathbf{j}$ and $\mathbf{M}\perp\mathbf{s}$, so that the longitudinal resistance is at its maximum R_{max}. For a sufficiently high magnetic field, spin canting occurs [53, 54], where the sublattice magnetizations turn to a position perpendicular to the external magnetic field and are slightly tilted in the direction of $\mathbf{H}_0$ (see Fig. 5.10 a) and c)). For this configuration, the sublattices $\mathbf{M}_i$ are nearly perpendicular to the current direction $\mathbf{j}$ and nearly parallel to the spin current polarization $\mathbf{s}$, so that R_{long} approaches its minimum. This explains the decrease of R_{long} for $|\mu_0 H_0| > 2\,\mathrm{T}$, as shown in Fig. 5.8 b).

In this configuration, even though the small net magnetization is collinear to $\mathbf{H}_0$, the individual sublattice magnetizations are not. If we now rotate the magnetic field by 90°, the $\mathbf{M}_i$ are again perpendicular to the spin polarization $\mathbf{s}$ and R_{long} increases as shown in Fig. 5.6, even though the net magnetization $\mathbf{M}$ is aligned with $\mathbf{s}$.

The same considerations can again be applied to the configuration where $\alpha' = -90°$ in order to obtain the blue dots in Fig. 5.8.

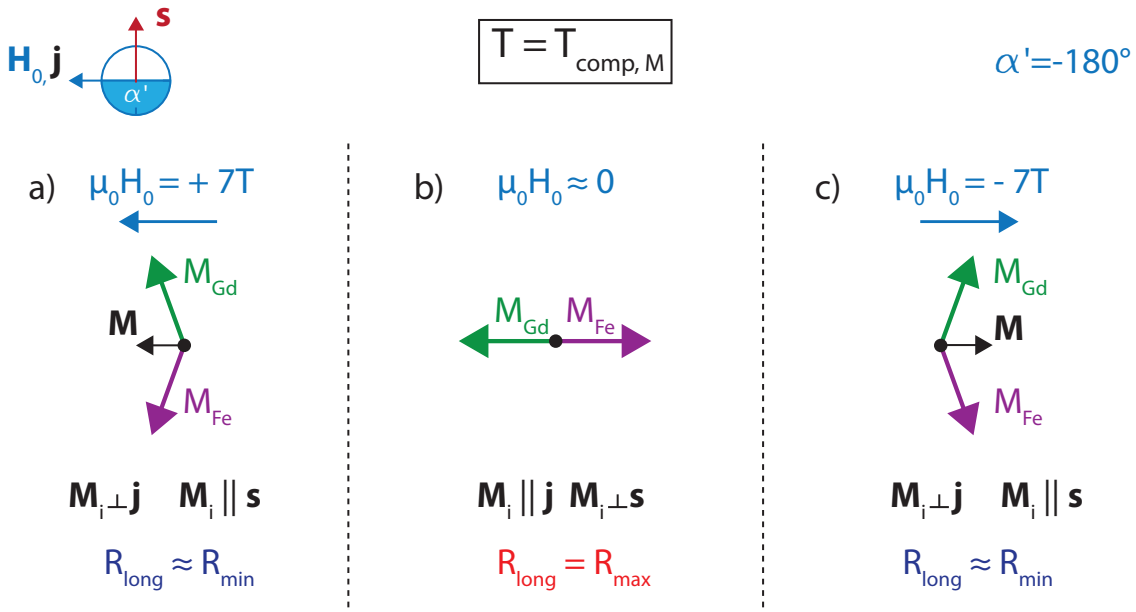

Figure 5.10: Illustration of the magnetization behaviour in InYGdIG/Pt in a magnetic field sweep at $T = T_{\mathrm{comp,\,M}}$, where the net Fe magnetization (purple arrow) and the Gd magnetization (green arrow) compensate each other. The dc current $\mathbf{j}$ and the magnetic field $\mu_0\mathbf{H}_0$ are applied along $\alpha' = -180°$. a) At $\mu_0 H_0 = 7\,\mathrm{T}$ a spin canting [53] occurs and the sublattice magnetizations are reoriented perpendicular to the external magnetic field, so that $\mathbf{M}_i \perp \mathbf{j}$ and $\mathbf{M}_i \parallel \mathbf{s}$. R_{long} reaches a minimum in this configuration. b) At zero magnetic field both magnetizations are aligned with $\mathbf{H}_0$, so that $\mathbf{M}_i \perp \mathbf{s}$ and $R_{\mathrm{long}} = R_{\mathrm{max}}$. c) At $\mu_0 H_0 = -7\,\mathrm{T}$, the situation is the same as in (a) and the longitudinal resistance is small again.

Our interpretation of the measurements conducted in the spin canting phase around the compensation temperature indicate that the SMR effect does not depend on the orientation of the net magnetization $\mathbf{M}$, but on the orientation of the sublattice magnetizations $\mathbf{M}_i$. To our knowledge, this is the first time such an observation was made.

We can also compare these results to the microwave rectification in InYGdIG/Pt attributed to the SMR effect and discussed in Sect. 4.2.2.5. The rectification efficiency was found to decrease when approaching the compensation region, which is consistent with the very pronounced decrease of the SMR amplitude in Fig. 5.7. However, no rectification voltage could be detected close to the compensation temperature because the FMR linewidth was too large to observe a resonant voltage.

In conclusion, we were able to observe the SMR effect in InYGdIG/Pt, and found a slight decrease of the SMR ratio with decreasing temperature, similar to the measurements in YIG/Pt [8]. Around the magnetization compensation temperature, the SMR ratio decreases strongly, which is consistent with the rectification efficiency discussed in

Sect. 4.2.2.5, and changes sign. This sign change of the SMR amplitude R_1 is due to the interchanging of the minimum and maximum resistance configuration, which corresponds to a shift by 90° of the $\cos^2(\alpha')$ dependence of the longitudinal resistance on the magnetic field orientation. The shift can be explained by the fact that for a sufficiently high magnetic field, the sublattice magnetizations enter the spin canting phase, so that the individual magnetizations are rotated by approximately 90°. Since the SMR effect does not disappear in this configuration even though the net magnetization goes to zero, we conclude that the SMR effect does not depend on the orientation of the net magnetization of the sample, but on the individual sublattice magnetizations, leading to the 90° shift of the angle dependence in the spin canting phase at $T_{\mathrm{comp,\,M}}$. In order to confirm this statement, further investigations will be necessary, i.e. the magnetic field dependence of the R_1 sign changes in SMR measurements in the compensation region. Additionally, a more direct observation of the spin canting phase and its magnetic field and temperature dependence will allow for a magnetic field vs temperature phase diagram, which we can then compare to the SMR data.

Chapter 6

Summary and Outlook

In this thesis, spin current flow in magnetic insulator/Pt heterostructures was investigated. The key idea hereby was to use particular magnetic insulators, which exhibit a magnetic compensation point, or possibly even an angular momentum compensation point. In these so-called magnetically compensated ferrimagnetic insulators, e.g., GdIG, InYGdIG, etc., close to the compensation points, magnetic moment and angular momentum (spin) must no longer be strictly antiparallel. Simply speaking, the goal behind the thesis thus was to try to experimentally measure whether a spin current is a current of angular momentum, or should rather be thought of as a current of magnetic moment. More specifically, we studied GdIG/Pt and InYGdIG/Pt heterostructures using spin Seebeck, spin pumping effect and spin Hall magnetoresistance measurements as a function of temperature and magnetic field magnitude and orientation. In this Chapter, we give a summary of the experimental results we obtained and possible models for their explanation. We also propose future experiments for further investigation of the observed effects.

6.1 Summary

In this thesis, we performed temperature dependent spin current experiments in magnetic insulator/Pt heterostructures. The magnetic insulator mainly used was the compensated ferrimagnetic system, Gadolinium Iron Garnet (GdIG). This system features three magnetic sublattices, one of Gd^{3+} and two of Fe^{3+}. The Gd^{3+} sublattice is coupled ferromagnetically to one Fe^{3+} sublattice and antiferromagnetically to the other. The Fe^{3+} sublattices are coupled antiferromagnetically to each other.

To get a quantitative notion of the magnetic properties, SQUID magnetometry was performed on the GdIG films as a function of temperature. We found a strongly temperature dependent magnetization with a characteristic minimum at the GdIG magnetization compensation temperature $T_{\mathrm{comp,\,M}} = 279\,\mathrm{K}$. This behaviour can be described by a simulation based on the mean field model, assuming that each magnetic moment feels, in addition to the external magnetic field, an average molecular field from the other magnetic moments. The model shows that at low temperatures, the Gd^{3+} sublattice dominates the magnetization. With increasing temperature, the magnetization of the Gd^{3+} sublattice

decreases and the Fe^{3+} moment dominates at temperatures higher than $T_{\mathrm{comp,\,M}}$. The simulation also allows for the calculation of the angular momentum of the sublattices. The angular momentum compensation temperature $T_{\mathrm{comp,\,L}}$ is not the same as $T_{\mathrm{comp,\,M}}$, but in GdIG $T_{\mathrm{comp,\,M}}$ and $T_{\mathrm{comp,\,L}}$ are no more than 4 K apart, making an experimental distinction rather difficult. The proportionality constant between the total magnetization and the total angular momentum, i.e. the effective gyromagnetic ratio, nevertheless is highly temperature dependent around the compensation temperature.

Furthermore, it was found that doping GdIG with non magnetic ions Y^{3+} and In^{3+} [65, 66] lowers the magnetization compensation temperature. In InYGdIG, we experimentally obtained $T_{\mathrm{comp,\,M}} = 85\,\mathrm{K}$, which could also be reproduced quantitatively by our simulation. The calculations then yielded $T_{\mathrm{comp,\,L}} = 86\,\mathrm{K}$. Even though in InYGdIG, $T_{\mathrm{comp,\,M}}$ and $T_{\mathrm{comp,\,L}}$ are even closer together than in GdIG, we mainly focused on this InYGdIG/Pt sample, because the doping also lead to a smaller FMR linewidth, which is advantageous for spin pumping experiments.

In Chapter 4, we described the simultaneous measurement of spin pumping voltage and spin Seebeck (SSE) voltage in the InYGdIG/Pt bilayer. These measurements were performed in a microwave cavity: the microwave radiation was used to excite the ferromagnetic resonance needed for spin pumping. It furthermore heated the Pt via eddy currents, and thus allowed to induce a temperature gradient for the SSE. The SSE voltage shows two sign changes as a function of temperature: the sign change around the higher temperature $T = 85\,\mathrm{K}$ is at the magnetization compensation temperature and can be understood in terms of the inversion of all sublattices in an external magnetic field at this temperature. The second sign change, at a lower temperature $T = 40\,\mathrm{K}$ can be explained by assuming that the contribution from one sublattice to the SSE voltage is proportional to its magnetization and that the proportionality constants are different for the Gd^{3+} and Fe^{3+} sublattices. A simulation based on this model, together with the sublattice magnetizations extracted from SQUID magnetometry, allows to quantitatively reproduce the experimental data, if one assumes that the Gd^{3+} sublattice contributes to the SSE effect 0.75 times as efficiently as the Fe^{3+} sublattices.

In the spin pumping voltage there are, as a function of temperature, also two sign changes: one sign change takes place again at the compensation temperature. However, the second sign change in spin pumping is at a temperature above T_{comp}. The model we proposed for the interpretation of the SSE voltage reproduces the experimental data assuming that the Gd^{3+} sublattice contributes to spin pumping 1.2 times more efficiently than the Fe^{3+} sublattices. This indicates that the SSE and spin pumping voltage depend on different parameters, and a possible explanation would be that the SSE depends on the magnetization, while the spin pumping is connected to the angular momentum. This hypothesis however has yet to be confirmed theoretically and experimentally.

In summary, our measurements unambiguously show, that the spin current genera-

tion via spin pumping and SSE in the magnetically compensated bilayer (InY)GdIG/Pt does not depend on the total magnetization. Rather, the magnetizations (or angular momenta) of the individual sublattices contribute independently. This is a new key insight.

In addition to the voltage amplitude we also analyzed the temperature dependence of FMR field and linewidth in InYGdIG: we found a strong decrease of the resonance field in the compensation region, which was reproduced by our simulation. We attributed this behaviour to a combination of the divergence of the effective gyromagnetic ratio at $T_{\mathrm{comp,\,L}}$ and the divergence of the magnetic anisotropy field at $T_{\mathrm{comp,\,M}}$. Furthermore, we observed the divergence of the FMR linewidth at the compensation temperature, which we attributed to a strong increase of the effective damping coefficient at $T_{\mathrm{comp,\,L}}$. The analysis of FMR linewidth and resonance position as a function of temperature yields information about the properties of both compensation points and provides an important consistency check for our multi-lattice model.

As described in the subsequent Chapter 5, we also conducted current heating-induced SSE measurements (iSSE) as well as SMR measurements simultaneously in InYGdIG/Pt as a function of temperature. As one might naively expect, the iSSE measurements confirmed the two sign changes observed in the microwave heating induced SSE. As also expected, when measuring the resistance of a Hall bar patterned into the InYGdIG/Pt bilayer as a function of magnetization orientation in the InYGdIG, we found a resistance modulation consistent with spin Hall magnetoresistance (SMR). As a function of temperature, this SMR amplitude is nearly constant – except for a temperature range of 10 K around $T_{\mathrm{comp,\,M}}$. In this narrow temperature window, the SMR amplitude decreases strongly and changes sign. Such a SMR sign change has never been reported to date in samples made from magnetic insulators without magnetic compensation. In other words, the SMR sign change must be connected to the compensation region. We proposed a model which explains the experimental observations. In this model, the sign change is attributed to the incidence of a spin canting phase near $T_{\mathrm{comp,\,M}}$, where the individual sublattice magnetizations are not collinear anymore to the external magnetic field. This explanation implies the fact that the SMR, like spin pumping and SSE, does not depend on the orientation of the total (net) magnetization, but is governed by the orientations of the sublattice magnetizations and/or angular momenta.

Our experimental findings thus suggest that spin current transport across a FMI/Pt interface is much more subtle than thought to date. The magnetic (angular) sublattices must be considered separately, instead of only the net magnetization.

6.2 Outlook

The temperature dependent measurements of the spin Seebeck, spin pumping and SMR effect in the compensated magnetic insulators GdIG and InYGdIG presented in this thesis thus request a series of experiments to test the "each sublattice contributes in its own right" hypothesis, which could provide a deeper understanding of spin current transport and spin current generation.

6.2.1 Separation of magnetization and angular momentum compensation temperature

We have performed measurements in GdIG-based magnetic insulators, in which the compensation temperature of magnetization and angular momentum are so close together, that they could not be discerned in our experiments. In order to unambiguously attribute specific processes, such as spin current generation, to either the magnetization or to the angular momentum, it is mandatory to use a material, in which $T_{\mathrm{comp,\,M}}$ and $T_{\mathrm{comp,\,L}}$ can be distinguished more clearly.

We have seen that the difference between $T_{\mathrm{comp,\,M}}$ and $T_{\mathrm{comp,\,L}}$ is caused by differing sublattice g values (see Sect. 1.5). Since in GdIG all magnetic ions carry only spin angular momentum, their g values are close to 2 [25]. Replacing the Gd^{3+} by Dy^{3+}, which has an additional orbital angular momentum and $g \neq 2$, should then yield a larger temperature difference between $T_{\mathrm{comp,\,L}}$ and $T_{\mathrm{comp,\,M}}$. DyIG/Pt thin film samples were already grown in the WMI by F. Della Coletta [63] in order to investigate the SSE and SMR effect[1]. Using the exchange coefficients from DyIG and $g_{\mathrm{Dy}} = 1.54$ provided by Ref. [23] in our simulation (see Chapter 3), we obtain $T_{\mathrm{comp,\,M}} = 238\,\mathrm{K}$ and $T_{\mathrm{comp,\,L}} = 330\,\mathrm{K}$, as shown in Fig. 6.1 a). We would therefore not be able to experimentally probe the temperature region around $T_{\mathrm{comp,\,L}}$ in our experimental setups, which are limited to room temperature. However, we have seen that both compensation temperatures of rare earth iron garnets can be lowered by doping the material with non magnetic Y^{3+} and In^{3+} [65, 66]. For a doping of 50% of In^{3+} on the octahedrally ordered Fe^{3+} sublattice and 33% of Y^{3+} on the Dy^{3+} sublattice, our calculations yield $T_{\mathrm{comp,\,M}} = 88\,\mathrm{K}$ and $T_{\mathrm{comp,\,L}} = 135\,\mathrm{K}$, as shown in Fig. 6.1 b). An InYDyIG/Pt bilayer is therefore a promising candidate for further SSE, spin pumping and SMR measurements, since it should allow for the separate study of magnetization and angular momentum compensation and their impact on spin current transport.

[1] Master thesis in progress

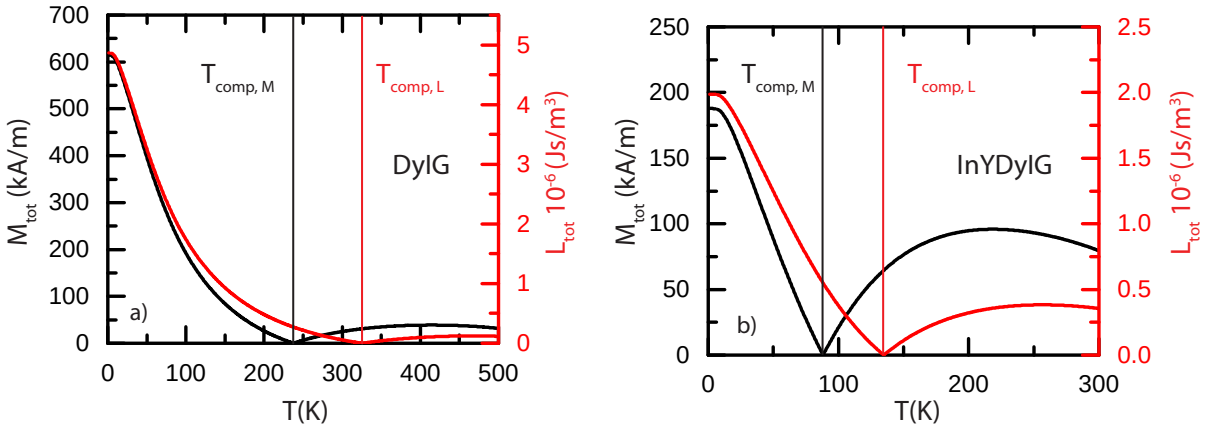

Figure 6.1: a) Simulation of the total magnetization (black) and angular momentum (red) in DyIG, with $T_{\mathrm{comp,\,M}} = 238\,\mathrm{K}$ and $T_{\mathrm{comp,\,L}} = 330\,\mathrm{K}$. b) Total magnetization (black) and angular momentum (red) in InYDyIG, with $T_{\mathrm{comp,\,M}} = 88\,\mathrm{K}$ and $T_{\mathrm{comp,\,L}} = 135\,\mathrm{K}$.

6.2.2 Investigation of the spin canting phase

The SMR measurements in this thesis yielded a sign change of the SMR ratio in GdIG/Pt in the compensation region, and we attributed this to the spin canting phase. In order to confirm this model and obtain a deeper understanding of the mechanisms involved in the SMR effect, further investigations will be necessary. The width of the temperature region, in which the spin canting takes place, increases with the external magnetic field strength [53]. Therefore, SMR experiments in GdIG/Pt as a function of external magnetic field should enable us to extract a magnetic field vs temperature phase diagram similar to the one shown in Fig. 1.7 [53] and delimit the spin canting phase.

Furthermore, we expect that at $T_{\mathrm{comp,\,M}}$, the critical field above which spin canting occurs, does not vanish, but is finite due to the magnetic anisotropy of the sample. The calculations in Ref. [53] neglect such anisotropies, but our simulation can be extended to include magnetic anisotropies in order to reproduce our experimental results. This should then also allow for a better understanding of the behaviour of the magnetic anisotropy near $T_{\mathrm{comp,\,M}}$ and/or $T_{\mathrm{comp,\,L}}$.

Assuming we can observe the spin canting phase in SMR measurements, they are still an indirect observation of the sublattice magnetization orientation. A complementary experiment allowing for a more direct measurement of the spin canting phase will therefore be of great interest. To the best of our knowledge, no spin current transport experiments have been performed using magnetic insulators in the spin canted phase yet (except for those presented in this thesis). Clearly, the interplay between spin current and spin canting phenomena would be an interesting topic for further research.

Bernasconi et al. [53] successfully conducted Faraday rotation experiments in GdIG

films of 0.49 mm thickness: since the Faraday rotation is related to the orientation of the individual sublattice magnetizations [93], when the magnetizations enter the spin canting phase, a change of the rotation angle is observed.

The Faraday rotation, based on light transmission, is proportional to the sample thickness (as long as light transmission is still possible) and is therefore difficult to detect in our thin films. One instead could use the magneto-optical Kerr effect, which stems from the same phenomena as the Faraday effect [94], but is based on reflection and can thus be detected in thin films. Such measurements were already conducted at the WMI in ferromagnetic materials [95].

This thesis gave a first glimpse at the interesting and complex properties of spin current transport in magnetically compensated materials, and provided first models to explain the observed effects. Our results however also gave rise to new questions, and we proposed future experiments as continuation of this work, which will hopefully yield answers and a deeper understanding of spin current physics in FMI/Pt bilayers.

Appendix A

Temperature calibration: Determination of microwave heating in the Pt layer

In a magnetically compensated material we can make use of the characteristic temperature dependence of the coercive field around the compensation temperature to calibrate the heating induced in the Pt layer by the microwave radiation.

The microwave electric field is proportional to the square root of the microwave power

$$E \propto \sqrt{P_{\mathrm{mw}}} \tag{A.1}$$

and therefore induces a current $I_{\mathrm{mw}} \propto 1/R \cdot E \propto 1/R\sqrt{P_{\mathrm{mw}}}$. The Joule heating is then given as

$$P_{\mathrm{Joule}} = I_{\mathrm{mw}}^2 \cdot R \propto P_{\mathrm{mw}} \cdot 1/R \tag{A.2}$$

with R the resistance of the Pt layer. This Pt resistance is also temperature dependent, so that with increasing heating power, the resistance changes. Nevertheless, this change in the InYGdIG/Pt sample is of the order of $1\,\Omega\,\mathrm{K}^{-1}$ (determined from the temperature calibration in another setup, see Fig. 5.2) and can be neglected.

We therefore expect that the temperature increase of the sample is directly proportional to the microwave power. Comparing measurements at different cryostat temperatures but constant microwave power, with measurements at constant cryostat temperature but varying microwave power, will thus allow us to determine the microwave induced heating.

The results of the dc voltage measurements in InYGdIG/Pt at a constant microwave power of 18 dBm = 63 mW as a function of the cryostat temperature are discussed in Sect. 4.2.2 and the extracted coercive field is shown as orange dots in Fig. A.1 a). A linear approximation can be used to interpolate the experimental data (orange line). We repeated these voltage measurements for different microwave powers at a constant cryostat temperature of $T_{\mathrm{cryo}} = 70\,\mathrm{K}$ and again extracted the coercive field. The results can be

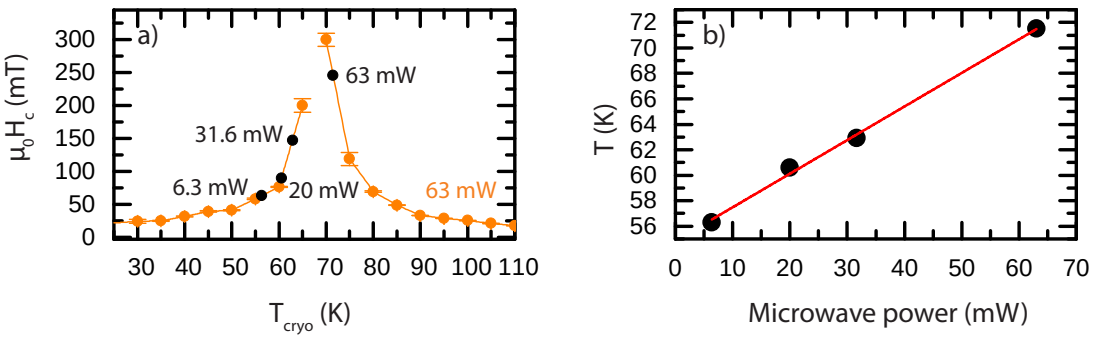

Figure A.1: a) The coercive field as a function of T_{cryo} at a constant microwave power of 18 dBm is represented by orange dots, the orange line is a linear interpolation of the experimental data. The black dots represent the coercive field at $T_{\mathrm{cryo}} = 70\,\mathrm{K}$ at different microwave powers. b) A new temperature is attributed to each microwave power (black dots), the red line represents a linear fit to the data.

compared to the coercive field obtained from the previous measurements and are plotted as black dots in Fig. A.1 a) with their corresponding microwave power.

We can now attribute a temperature to each microwave power as shown in Fig. A.1 b) and indeed find a linear temperature dependence of the additional heating. Using a linear fit (red line in Fig. A.1 b)), the temperature at zero microwave power can be extrapolated to about 55 K. We find a temperature difference of 18 K between on and off switching of the microwave heating, so that $T_{\mathrm{sample}} = T_{\mathrm{cryo}} + 18\,\mathrm{K}$.

This calibration is valid in the temperature range around the compensation temperature, but the measurements described here do not give us any information whether the correction is the same over the whole temperature range. In general, thermalization effects have to be taken into account, since the thermal coupling of the sample to the environment depends on the gas flow and temperature difference between sample and gas.

Due to this issue the temperature scale was not corrected in the measurement data, but the power dependent measurements shall at least give an idea of the temperature deviation between sample and cryostat sensor.

Bibliography

[1] E. Saitoh, M. Ueda, H. Miyajima, and G. Tatara, "Conversion of spin current into charge current at room temperature: Inverse spin-Hall effect", Applied Physics Letters **88**, 182509 (2006).

[2] K. Uchida, S. Takahashi, K. Harii, J. Ieda, W. Koshibae, K. Ando, S. Maekawa, and E. Saitoh, "Observation of the spin Seebeck effect", Nature **455**, 778 (2008).

[3] K. Uchida, J. Xiao, H. Adachi, J. Ohe, S. Takahashi, J. Ieda, T. Ota, Y. Kajiwara, H. Umezawa, H. Kawai, G. E. W. Bauer, S. Maekawa, and E. Saitoh, "Spin Seebeck insulator", Nature Materials **9**, 894 (2010).

[4] Y. Tserkovnyak, A. Brataas, and G. E. W. Bauer, "Spin pumping and magnetization dynamics in metallic multilayers", Physical Review B **66**, 224403 (2002).

[5] Y. Tserkovnyak, A. Brataas, and G. E. W. Bauer, "Enhanced Gilbert Damping in Thin Ferromagnetic Films", Physical Review Letters **88**, 117601 (2002).

[6] M. Althammer, S. Meyer, H. Nakayama, M. Schreier, S. Altmannshofer, M. Weiler, H. Huebl, S. Geprägs, M. Opel, R. Gross, D. Meier, C. Klewe, T. Kuschel, J.-M. Schmalhorst, G. Reiss, L. Shen, A. Gupta, Y.-T. Chen, G. E. W. Bauer, E. Saitoh, and S. T. B. Goennenwein, "Quantitative study of the spin Hall magnetoresistance in ferromagnetic insulator/normal metal hybrids", Physical Review B **87**, 224401 (2013).

[7] H. Nakayama, M. Althammer, Y.-T. Chen, K. Uchida, Y. Kajiwara, D. Kikuchi, T. Ohtani, S. Geprägs, M. Opel, S. Takahashi, R. Gross, G. E. W. Bauer, S. T. B. Goennenwein, and E. Saitoh, "Spin Hall Magnetoresistance Induced by a Nonequilibrium Proximity Effect", Physical Review Letters **110**, 206601 (2013).

[8] S. Meyer, M. Althammer, S. Geprägs, M. Opel, R. Gross, and S. T. B. Goennenwein, "Temperature dependent spin transport properties of platinum inferred from spin Hall magnetoresistance measurements", Applied Physics Letters **104**, 242411 (2014).

[9] M. Weiler, M. Althammer, F. D. Czeschka, H. Huebl, M. S. Wagner, M. Opel, I.-M. Imort, G. Reiss, A. Thomas, R. Gross, and S. T. B. Goennenwein, "Local Charge and Spin Currents in Magnetothermal Landscapes", Physical Review Letters **108**, 106602 (2012).

[10] M. Weiler, M. Althammer, M. Schreier, J. Lotze, M. Pernpeintner, S. Meyer, H. Huebl, R. Gross, A. Kamra, J. Xiao, Y.-T. Chen, H. Jiao, G. E. W. Bauer, and S. T. B. Goennenwein, "Experimental Test of the Spin Mixing Interface Conductivity Concept", Physical Review Letters **111**, 176601 (2013).

[11] D. Meier, T. Kuschel, L. Shen, A. Gupta, T. Kikkawa, K. Uchida, E. Saitoh, J.-M. Schmalhorst, and G. Reiss, "Thermally driven spin and charge currents in thin $NiFe_2O_4$/Pt films", Physical Review B **87**, 054421 (2013).

[12] D. Qu, S. Y. Huang, J. Hu, R. Wu, and C. L. Chien, "Intrinsic Spin Seebeck Effect in Au/YIG", Physical Review Letters **110**, 067206 (2013).

[13] S. M. Rezende, R. L. Rodríguez-Suárez, R. O. Cunha, A. R. Rodrigues, F. L. A. Machado, G. A. Fonseca Guerra, J. C. Lopez Ortiz, and A. Azevedo, "Magnon spin-current theory for the longitudinal spin-Seebeck effect", Physical Review B **89**, 014416 (2014).

[14] O. Mosendz, V. Vlaminck, J. E. Pearson, F. Y. Fradin, G. E. W. Bauer, S. D. Bader, and A. Hoffmann, "Detection and quantification of inverse spin Hall effect from spin pumping in permalloy/normal metal bilayers", Physical Review B **82**, 214403 (2010).

[15] F. D. Czeschka, L. Dreher, M. S. Brandt, M. Weiler, M. Althammer, I.-M. Imort, G. Reiss, A. Thomas, W. Schoch, W. Limmer, H. Huebl, R. Gross, and S. T. B. Goennenwein, "Scaling Behavior of the Spin Pumping Effect in Ferromagnet-Platinum Bilayers", Physical Review Letters **107**, 046601 (2011).

[16] C. H. Du, H. L. Wang, Y. Pu, T. L. Meyer, P. M. Woodward, F. Y. Yang, and P. C. Hammel, "Probing the Spin Pumping Mechanism: Exchange Coupling with Exponential Decay in $\mathbf{Y}_3\mathrm{Fe}_5\mathbf{O}_{12}$/Barrier/Pt Heterostructures", Physical Review Letters **111**, 247202 (2013).

[17] C. Hahn, G. de Loubens, M. Viret, O. Klein, V. V. Naletov, and J. Ben Youssef, "Detection of Microwave Spin Pumping Using the Inverse Spin Hall Effect", Physical Review Letters **111**, 217204 (2013).

[18] J. Xiao, G. E. W. Bauer, K.-c. Uchida, E. Saitoh, and S. Maekawa, "Theory of magnon-driven spin Seebeck effect", Physical Review B **81**, 214418 (2010).

[19] N. Roschewsky, M. Schreier, A. Kamra, F. Schade, K. Ganzhorn, S. Meyer, H. Huebl, S. Geprägs, R. Gross, and S. T. B. Goennenwein, "Time resolved spin Seebeck effect experiments", Applied Physics Letters **104**, 202410 (2014).

[20] Y.-T. Chen, S. Takahashi, H. Nakayama, M. Althammer, S. T. B. Goennenwein, E. Saitoh, and G. E. W. Bauer, "Theory of spin Hall magnetoresistance", Physical Review B **87**, 144411 (2013).

[21] E. Landau, L. Lifschitz, "On the theory of the dispersion of magnetic permeability in ferromagnetic bodies", Zeitschrift der Sowjetunion **8**, 153 (1935).

[22] T. Gilbert, "A phenomenological theory of damping in ferromagnetic materials", Magnetics, IEEE Transactions on **40**, 3443 (2004).

[23] G. F. Dionne, *Magnetic Oxides* (Springer, 2009).

[24] R. K. Wangsness, "Ferrimagnetic Resonance and Some Related Effects", American Journal of Physics **24**, 60 (1956).

[25] A. Abragam and B. Bleaney, *Electron Paramagnetic Resonance of Transition Ions* (Oxford University Press, 1970).

[26] R. C. LeCraw, J. P. Remeika, and H. Matthews, "Angular Momentum Compensation in Narrow Linewidth Ferrimagnets", Journal of Applied Physics **36**, 901 (1965).

[27] S. V. Vonsovskii, *Ferromagnetic Resonance* (1964).

[28] A. Brandlmaier, "Magnetische Anisotropie in dünnen Schichten aus Magnetit", Master's thesis, Technische Universität München (2006).

[29] M. Dyakonov and V. Perel, "Possibility of Orienting Electron Spin with Current", Journal of Experimental and Theoretical Physics **13**, 467 (1971).

[30] J. E. Hirsch, "Spin Hall Effect", Physical Review Letters **83**, 1834 (1999).

[31] Y. K. Kato, R. C. Myers, A. C. Gossard, and D. D. Awschalom, "Observation of the Spin Hall Effect in Semiconductors", Science **306**, 1910 (2004).

[32] N. F. Mott, "The Scattering of Fast Electrons by Atomic Nuclei", Proceedings of the Royal Society of London A **124**, 425 (1929).

[33] L. Berger, "Side-Jump Mechanism for the Hall Effect of Ferromagnets", Physical Review B **2**, 4559 (1970).

[34] J. Sinova, D. Culcer, Q. Niu, N. A. Sinitsyn, T. Jungwirth, and A. H. MacDonald, "Universal Intrinsic Spin Hall Effect", Physical Review Letters **92**, 126603 (2004).

[35] F. D. Czeschka, "Spin Currents in Metallic Nanostructures", Ph.D. thesis, Technische Universität München (2011).

[36] M. Schreier, G. E. W. Bauer, V. Vasyuchka, J. Flipse, K.-I. Uchida, J. Lotze, V. Lauer, A. Chumak, A. Serga, S. Daimon, T. Kikkawa, E. Saitoh, B. J. van Wees, B. Hillebrands, R. Gross, and S. T. B. Goennenwein, "Sign of inverse spin Hall voltages generated by ferromagnetic resonance and temperature gradients in yttrium iron garnet|platinum bilayers", ArXiv e-prints:1404.3490 (2014).

[37] D. Jiles, J. Thoelke, and M. Devine, "Numerical determination of hysteresis parameters for the modeling of magnetic properties using the theory of ferromagnetic hysteresis", Magnetics, IEEE Transactions on **28**, 27 (1992).

[38] K.-i. Uchida, H. Adachi, T. Ota, H. Nakayama, S. Maekawa, and E. Saitoh, "Observation of longitudinal spin-Seebeck effect in magnetic insulators", Applied Physics Letters **97**, 172505 (2010).

[39] M. Weiler, "Magnon-Phonon Interactions in Ferromagnetic thin Films", Ph.D. thesis, Technische Universität München (2012).

[40] M. Schreier, "Spatially resolved Spin Seebeck Experiments", Master's thesis, Technische Universität München (2012).

[41] M. Schreier, N. Roschewsky, E. Dobler, S. Meyer, H. Huebl, R. Gross, and S. T. B. Goennenwein, "Current heating induced spin Seebeck effect", Applied Physics Letters **103**, 242404 (2013).

[42] N. Roschewsky, "Spin Seebeck Effect Measurements", Master's thesis, Technische Universität München (2014).

[43] M. Schreier, A. Kamra, M. Weiler, J. Xiao, G. E. W. Bauer, R. Gross, and S. T. B. Goennenwein, "Magnon, phonon, and electron temperature profiles and the spin Seebeck effect in magnetic insulator/normal metal hybrid structures", Physical Review B **88**, 094410 (2013).

[44] O. Mosendz, J. E. Pearson, F. Y. Fradin, G. E. W. Bauer, S. D. Bader, and A. Hoffmann, "Quantifying Spin Hall Angles from Spin Pumping: Experiments and Theory", Physical Review Letters **104**, 046601 (2010).

[45] K. Ando, T. Yoshino, and E. Saitoh, "Optimum condition for spin-current generation from magnetization precession in thin film systems", Applied Physics Letters **94**, 152509 (2009).

[46] A. Azevedo, L. H. Vilela-Leão, R. L. Rodríguez-Suárez, A. F. Lacerda Santos, and S. M. Rezende, "Spin pumping and anisotropic magnetoresistance voltages in magnetic bilayers: Theory and experiment", Physical Review B **83**, 144402 (2011).

[47] N. Vlietstra, J. Shan, V. Castel, B. J. van Wees, and J. Ben Youssef, "Spin-Hall magnetoresistance in platinum on yttrium iron garnet: Dependence on platinum thickness and in-plane/out-of-plane magnetization", Physical Review B **87**, 184421 (2013).

[48] C. Hahn, G. de Loubens, O. Klein, M. Viret, V. V. Naletov, and J. Ben Youssef, "Comparative measurements of inverse spin Hall effects and magnetoresistance in YIG/Pt and YIG/Ta", Physical Review B **87**, 174417 (2013).

[49] L. H. Bai, Y. S. Gui, A. Wirthmann, E. Recksiedler, N. Mecking, C.-M. Hu, Z. H. Chen, and S. C. Shen, "The rf magnetic-field vector detector based on the spin rectification effect", Applied Physics Letters **92**, 032504 (2008).

[50] L. Bai, Z. Feng, P. Hyde, H. F. Ding, and C.-M. Hu, "Distinguishing spin pumping from spin rectification in a Pt/Py bilayer through angle dependent line shape analysis", Applied Physics Letters **102**, 242402 (2013).

[51] R. Iguchi, K. Sato, D. Hirobe, S. Daimon, and E. Saitoh, "Effect of spin Hall magnetoresistance on spin pumping measurements in insulating magnet/metal systems", Applied Physics Express **7**, 013003 (2014).

[52] C. P. J. Poole, *Electron Spin Resonance* (Dover Publications, 1983).

[53] J. Bernasconi and D. Kuse, "Canted Spin Phase in Gadolinium Iron Garnet", Physical Review B **3**, 811 (1971).

[54] A. E. Clark and E. Callen, "Neel Ferrimagnets in Large Magnetic Fields", Journal of Applied Physics **39**, 5972 (1968).

[55] N. Miura, I. Oguro, and S. Chikazumi, "Computer simulation of temperature and field dependences of sublattice mmagnetization and spin-flip transition in Gallium-substituted Yttrium Iron Garnet", Journal of the Physical Society of Japan **45**, 1534 (1978).

[56] C. Kittel, "Theory of Ferromagnetic Resonance in Rare Earth Garnets. I. g Values", Physical Review **115**, 1587 (1959).

[57] S. Geschwind and L. R. Walker, "Exchange Resonances in Gadolinium Iron Garnet near the Magnetic Compensation Temperature", Journal of Applied Physics **30**, S163 (1959).

[58] M. Giles, R. Mansuripur, "Dynamic of the magnetization reversal in amorphous films of rare earth-transition metal alloys", Journal of the Magnetics Society Japan **15**, 299 (1991).

[59] F. Keffer and C. Kittel, "Theory of Antiferromagnetic Resonance", Physical Review **85**, 329 (1952).

[60] B. Lax and K. Button, *Microwave Ferrites and Ferrimagnetics* (Literary Licensing, 2012).

[61] M. Althammer, "Spin-transport phenomena in metals, semiconductors, and insulators", Ph.D. thesis, Technische Universität München (2012).

[62] M. S. Wagner, "Epitaktisches Wachstum dünner, ferromagnetischer Schichten aus $\mathbf{Y}_3\mathrm{Fe}_5\mathbf{O}_{12}$ mittels gepulster Laserdeposition", Master's thesis, Technische Universität München (2011).

[63] F. Della Coletta, "Work in progress", Master's thesis, Technische Universität München (2014).

[64] S. Geller, "Magnetic Interactions and Distribution of Ions in the Garnets", Journal of Applied Physics **31**, S30 (1960).

[65] E. A. Maguire and J. J. Green, "Magnetic properties of Gadolinium-Yttrium-Iron-Indium-Garnets", Journal of the American Ceramic Society **48**, 7 (1965).

[66] T. Shinohara, S. Takeda, Y. Matsumoto, and Y. Noro, "Magnetic properties of polycrystalline gadolinium calcium vanadium and indium substituted YIG", Magnetics, IEEE Transactions on **11**, 1676 (1975).

[67] E. Schlömann, "Spin-wave analysis of ferromagnetic resonance in polycrystalline ferrites", Journal of Physics and Chemistry of Solids **6**, 242 (1958).

[68] H. J. Van Hook, J. J. Green, F. Euler, and E. R. Czerlinsky, "Linewidth Reduction through Indium Substitution in Calcium-Vanadium Garnets", Journal of Applied Physics **39**, 730 (1968).

[69] S. Frölich, "Thin Film Fabrication for Spin Current and Spin Caloric Experiments", (2014).

[70] Y. Kajiwara, K. Harii, S. Takahashi, J. Ohe, K. Uchida, M. Mizuguchi, H. Umezawa, H. Kawai, K. Ando, K. Takanashi, S. Maekawa, and E. Saitoh, "Transmission of electrical signals by spin-wave interconversion in a magnetic insulator", Nature **464**, 262 (2010).

[71] S. Altmannshofer, "Epitaxie und Charakterisierung von dünnen Schichten des ferromagnetischen Isolators $\mathbf{Y}_3\mathrm{Fe}_5\mathbf{O}_{12}$", Master's thesis, Technische Universität München (2012).

[72] G. F. Dionne, "Molecular Field Coefficients of Substituted Yttrium Iron Garnets", Journal of Applied Physics **41**, 4874 (1970).

[73] G. F. Dionne, "Molecular Field and Exchange Constants of Gd3+Substituted Ferrimagnetic Garnets", Journal of Applied Physics **42**, 2142 (1971).

[74] S. Blundell, *Magnetism in Condensed Matter* (Oxford University Press, 2001).

[75] S. Geschwind, "Sign of the Ground-State Cubic Crystal Field Splitting Parameter in Fe^{3+}", Physical Review Letters **3**, 207 (1959).

[76] W. Low, "Paramagnetic Resonance Spectrum of Trivalent Gadolinium in the Cubic Field of Calcium Fluoride", Physical Review **109**, 265 (1958).

[77] G. P. Rodrigue, H. Meyer, and R. V. Jones, "Resonance Measurements in Magnetic Garnets", Journal of Applied Physics **31**, S376 (1960).

[78] J. Pauleve, "Magnetic Resonance of Ferrites with a Compensation Temperature", Journal of Applied Physics **29**, 259 (1958).

[79] B. A. Calhoun, J. Overmeyer, and W. V. Smith, "Ferrimagnetic Resonance in Gadolinium Iron Garnet", Physical Review **107**, 993 (1957).

[80] S. Geprägs, A. Kehlberger, T. Schulz, C. Mix, F. Della Coletta, S. Meyer, A. Kamra, M. Althammer, G. Jakob, H. Huebl, R. Gross, S. T. B. Goennenwein, and M. Kläui, "Origin of the spin Seebeck effect probed by temperature dependent measurements in $\mathbf{Y}_3\mathrm{Fe}_5\mathbf{O}_{12}$/Barrier/Pt", ArXiv e-prints:1405.4971 (2014).

[81] R. J. Corruccini, "Interpolation of Platinum Resistance Thermometers, 20K to 273.15K", Review of Scientific Instruments **31**, 637 (1960).

[82] M. Agrawal, A. A. Serga, V. Lauer, E. T. Papaioannou, B. Hillebrands, and V. I. Vasyuchka, "Microwave-induced spin currents in ferromagnetic-insulator|normal-metal bilayer system", ArXiv e-prints:1407.4957 (2014).

[83] B. Kuanr, V. Veerakumar, A. Kuanr, R. Camley, and Z. Celinski, "Effect of Temperature on the Ferromagnetic-Resonance Field and Line Width of Epitaxial Fe Thin Films", Magnetics, IEEE Transactions on **45**, 4015 (2009).

[84] R. Meckenstock, K. Harms, O. von Geisau, and J. Pelzl, "Temperature-dependent FMR investigations on epitaxial Fe (001) films with different thicknesses", Journal of Magnetism and Magnetic Materials **148**, 139 (1995).

[85] Y. Krockenberger, H. Matsui, T. Hasegawa, M. Kawasaki, and Y. Tokura, "Solid phase epitaxy of ferrimagnetic Y3Fe5O12 garnet thin films", Applied Physics Letters **93**, 092505 (2008).

[86] Y. Krockenberger, K.-S. Yun, T. Hatano, S. Arisawa, M. Kawasaki, and Y. Tokura, "Layer-by-layer growth and magnetic properties of Y3Fe5O12 thin films on Gd3Ga5O12", Journal of Applied Physics **106**, 123911 (2009).

[87] F. Bernhard, *Technische Temperaturmessung* (Springer, 2004), ISBN 9783540626725.

[88] K. Uchida, T. Ota, H. Adachi, J. Xiao, T. Nonaka, Y. Kajiwara, G. E. W. Bauer, S. Maekawa, and E. Saitoh, "Thermal spin pumping and magnon-phonon-mediated spin-Seebeck effect", Journal of Applied Physics **111**, 103903 (2012).

[89] H. Adachi, K.-i. Uchida, E. Saitoh, J.-i. Ohe, S. Takahashi, and S. Maekawa, "Gigantic enhancement of spin Seebeck effect by phonon drag", Applied Physics Letters **97**, 252506 (2010).

[90] Y. Ohnuma, H. Adachi, E. Saitoh, and S. Maekawa, "Spin Seebeck effect in antiferromagnets and compensated ferrimagnets", Physical Review B **87**, 014423 (2013).

[91] T. R. McGuire, "Microwave Resonance Absorption in Nickel Ferrite-Aluminate", Physical Review **93**, 682 (1954).

[92] A. Gross, R. Marx, *Festkörperphysik* (Oldenbourg, 2012).

[93] W. A. Crossley, R. W. Cooper, J. L. Page, and R. P. van Stapele, "Faraday Rotation in Rare-Earth Iron Garnets", Physical Review **181**, 896 (1969).

[94] C. C. Robinson, "Longitudinal Kerr Magneto-Optic Effect in Thin Films of Iron, Nickel, and Permalloy", Journal of the Optical Society of America **53**, 681 (1963).

[95] M. Pelkner, "Aufbau und Charakterisierung eines Spektrometers für Magnetooptischen Kerr-Effekt", Master's thesis, Technische Universität München (2008).

Acknowledgments

This thesis would not have been possible without the help and support of many people. I would like to thank:

- Prof. Dr. Rudolf Gross for giving me the opportunity to write my Master's thesis at the Walther-Meissner-Institut.
- PD Dr. Sebastian T. B. Gönnenwein for welcoming me into the Magnetiker group a few years ago, for his fascination for physics, for sharing his numerous ideas for new projects and experiments and many helpful discussions about my measurements.
- Johannes Lotze for supervising my work, introducing me to the FMR and spin pumping setup, for giving helpful answers to almost every question I had and for many long discussions, not only about my measurements, but about more mundane topics as well. I particularly thank him for his simulation of my experimental results, which I used to compare my data to.
- Dr. Stephan Geprägs for his ideas concerning new samples and new materials, for numerous discussions about my results and for always smiling when I came into his room.
- Francesco Della Coletta for growing all of the GdIG/Pt samples I used and conducting complementary measurements to my thesis.
- Sascha Frölich for growing InYGdIG/Pt samples and conducting some of the FMR measurements on those samples.
- Hannes Maier-Flaig for almost becoming my supervisor, for many discussions about physics and life.
- Dr. Hans Hübl, Michael Schreier, Sibylle Meier, Dr. Matthias Althammer and Dr. Matthias Opel for their collaboration and help.
- All the other members of the Magnetiker group, as well as my former roommates Edwar Xie and Dr. Edwin Menzel for the friendly atmosphere.
- All the strong, young men at WMI, who helped me carry around Helium dewars. My measurements would not have been possible without you!

- Rene and his staff at the ”Crazy Bean” for the great coffee and desserts and for spreading their good mood.
- The friends I made during the last five years in Munich, in particular my best friend Tanja, for making it through many of the physics lectures with me and being such an amazing friend.
- Kai for being a wonderful person, for supporting me and simply being there whenever needed.
- Last but not least, I want to thank my family, in particular my parents for their financial and especially their moral support, for making me the person I am today and enabling me to pursue my own path in life.